1-1-2009

Multiscale Friction Using A Nested Internal State Variable Model For Particulate Materials

Tonya Williams Stone

MULTISCALE FRICTION USING A NESTED INTERNAL STATE VARIABLE MODEL FOR PARTICULATE MATERIALS

By

Tonya Williams Stone

A Dissertation
Submitted to the Faculty of
Mississippi State University
in Partial Fulfillment of the Requirements
for the Degree of Doctor of Philosophy
in Mechanical Engineering
in the Department of Mechanical Engineering

Mississippi State, Mississippi

May 2009

MULTISCALE FRICTION USING A NESTED INTERNAL STATE VARIABLE

MODEL FOR PARTICULATE MATERIALS

By

Tonya Williams Stone

Approved:

Mark F. Horstemeyer Chair Professor of Mechanical Engineering (Director of Dissertation)	Douglas J. Bammann Professor of Mechanical Engineering (Committee Member)
Philip M. Gullett Assistant Professor of Civil Engineering (Committee Member)	Steven R. Daniewicz Professor of Mechanical Engineering (Graduate Coordinator)
D. Keith Walters Assistant Professor of Mechanical Engineering (Committee Member)	Youssef Hammi Assistant Research Professor of Mechanical Engineering (Committee Member)
Sarah A. Rajala Dean of the Bagley College of Engineering	

Name: Tonya Williams Stone

Date of Degree: May 2, 2009

Institution: Mississippi State University

Major Field: Mechanical Engineering

Major Professor: Dr. Mark F. Horstemeyer

Title of Study: MULTISCALE FRICTION USING A NESTED INTERNAL STATE VARIABLE MODEL FOR PARTICULATE MATERIALS

Pages in Study: 124

Candidate for Degree of Doctor of Philosophy

In the current study we use a multiscale computational methodology to develop an internal state variable model that captures frictional effects during the compaction of particulate materials. Molecular dynamics simulations using EAM potentials were performed to model the contact behavior of spherical nickel nanoparticles. Simulation results for models consisting of various particle sizes and contact angles were compared to quantify the length scale effects of friction. The influence of friction on the microstructure was shown from the nucleation of dislocations near the interface region during sliding. By using an internal state variable theory to couple the microstructural changes due to friction observed at the nanoscale to a macroscopic rate-independent plasticity model, a multiscale friction model that captures the deformation behavior due to dislocations and interparticle friction was developed. The internal state variable friction equation is a function of the volume-per-surface-area parameter and can adequately represent all length scales of importance from the nanoscale to the microscale.

The kinematics was modified by including a frictional component in the multiplicative decomposition of the deformation gradient in order to account for the frictional surface effects due to sliding, as well as frictional hardening/softening within the particles. The friction formulation was extended to the macroscale continuum model by determining the rate of change of the friction angle of the powder aggregate based on the evolution of the friction internal state variable. The constitutive model was coupled with the Bammann-Chiesa-Johnson (BCJ) rate-dependent plasticity model to capture the deformation behavior of the particles.

Key words: multiscale modeling, molecular dynamics, friction, granular materials, particle deformation

DEDICATION

I would like to dedicate this research to my parents, Ozzie H. Williams and the late Harold E. Williams; my husband, Dwayne; my children Joshua, Jordan, and Jasmine; and my last, but certainly not least, my sister, Tracey.

ACKNOWLEDGEMENTS

I would like to take this opportunity to express my appreciation and gratitude to the people who have helped and encouraged me in completing this dissertation. First, I would like to sincerely thank my advisor Dr. Mark F. Horstemeyer for his invaluable guidance and support and insistence on excellence throughout this process. His insight and guidance was invaluable in my accomplishing this work. I would also like to express my appreciation to my committee members Dr. Philip M. Gullett, Dr. Youssef Hammi, Dr. Doug Bammann, and Dr. Keith Walters for their patience in reading this dissertation and for their valuable comments and feedback.

Of my peers, I would particularly like to thank Bohumir Jelinek for his help and many useful suggestions in using the Molecular Dynamics code WARP.

Also I would like to express my sincere appreciation and thanks to my husband, Dwayne, for continually encouraging me during this process. I especially want to thank my children, Jasmine, Jordan, and Joshua, for being as understandable as possible about my being at work many late nights and weekends. Finally, I would like to thank my mother, Ozzie, my sister, Tracey, and all my friends and extended family for their support and love. Pursuing a doctorate degree in mechanical engineering was much more difficult that I had anticipated, and it was only my family's unwavering support and continuous encouragement that helped me through the difficult times.

I would also like to acknowledge the financial support for this research provided by the National Science Foundation Graduate Research Assistantship. I also express my gratitude to the James Worth Bagley College of Engineering at Mississippi State University and the Center for Advanced Vehicular Systems for supporting this research, as well as funding provided by U.S. Automotive Materials Partnership (AMD410) contract no. FC-26-02OR22910.

Most importantly I would like to thank God for giving me wisdom and strength when I needed it most but especially for giving me hope and the perseverance to continue on when I felt like giving up.

TABLE OF CONTENTS

LIST OF TABLES

LIST OF FIGURES

LIST OF SYMBOLS, ABBREVIATIONS, AND SPECIAL NOMENCLATURE

Abbreviations

MD	Molecular Dynamics
CNA	Common Neighbor Analysis
EAM	Embedded Atom Method
BCJ	Bammann-Chiesa-Johnson
PM	Powder Metal

Nomenclature

Molecular Dynamics

E	total atomic energy
F	local electron density of atoms
R	separation distance between atoms
ρ	electron density
β	atomic stress tensor
f	force vector between atoms
r	position vector between atoms
Ω	atomic volume
N^*	number of nearest neighbor atoms
σ	continuum-like atomic stress tensor
γ	interparticle contact angle

ISV Friction Model

φ	interparticle friction angle
ε_f	internal frictional strain
ε_{ss}	strains due to statistically stored dislocations
ϕ	damage
V	volume
υ	velocity
μ	coefficient of friction
f	fractional density
κ	isotropic hardening parameter
α	kinematic hardening parameter
τ	interface traction
τ_f	friction stress
τ_t	tangential traction

τ_n	normal traction
τ_Y	shear yield strength
F_n	normal load
F_t	tangential load
u_t	displacement at the interface
F	Deformation gradient
D	Rate of deformation
K	Bulk modulus
G	Shear modulus
b	Burger's vector
u	Internal energy per unit mass
ψ	Helmholz free energy
ρ	Density
θ	Temperature
q	Heat flux vector
s	specific entropy
r	internal heat supply
A_r	real contact area
A_a	apparent contact area
h	normal indentation
a	contact radius

CHAPTER I

INTRODUCTION

1.1 Motivation

Multiscale modeling has become a new wave of research that has allowed simulation-based design to have greater impact as higher fidelity physics is implemented. By including information from the lower length scales on the mechanical response of materials, more accurate predictions of material behavior can be achieved. Over the past ten years a great deal of effort has been directed toward accurately modeling the powder metallurgy (PM) compaction process. During compaction, powder is added to a die and compacted at high pressures to form a solid or green part. A schematic of closed die compaction, which is utilized in the current research and consists of a fixed die wall with loading applied through upper and lower punches, is provided in Figure 1.1. Due to the particulate nature of powders, densification of the compacted powder proceeds through plastic deformation at the particle contact and by the rearrangement of particles. Interparticle friction, combined with the friction between powder particles and the tooling surfaces, hinders the uniform consolidation of the metal powder leading to density variations in the compacted part. Additionally, high interparticle friction requires the use of higher compaction pressures to achieve a dense part. While powder lubricant is typically added to reduce interparticle friction, understanding dry friction effects on

powder deformation is an important step prior to expanding modeling capabilities to accurately predict the behavior of lubricated metal powders.

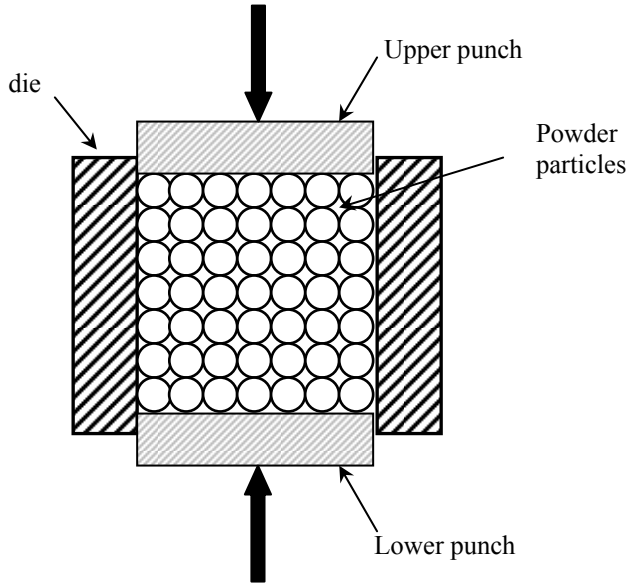

Figure 1.1 Schematic of powder particle compaction.

While several researchers have worked on modeling die compaction, most of the models are phenomenological material models based on density dependent variables [Coube and Riedel, 2000]. Attempts at developing micromechanical models in which the particle behavior is derived from lower length scale particle interactions have been made by a few researchers [Fleck et. al, 1992; Riedel et al., 1993/1994; Fleck, 1995; Storakers et al., 1999; Gu et al, 2001]. As shown in Figure 1.2, micromechanical models provide useful information regarding contact deformation; however, these models are limited to only a few hundred particles. Multiscale modeling for friction, particularly for powder metal materials, has been limited. Most previous work on developing continuum models that include evolution equations for friction have been done for geoscience materials such

as soils and sand [Anand and Gu, 2000; Hattamleh et al, 2007]. Using an internal state variable theory we can replace the particle behavior with a macroscale continuum model that captures the microstructural changes during compaction of the powder particles.

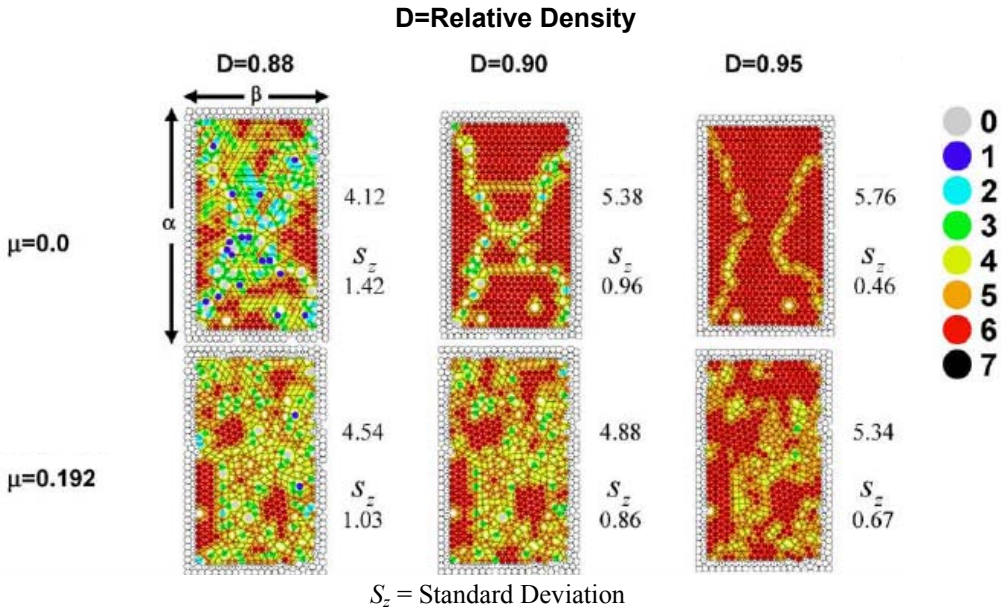

Figure 1.2 Multiparticle finite element model results of the effect of the coefficient of friction μ on the density distribution of hydrostatically compacted particles. [Reprinted from Procopio and Zavaliangos, 2005]

1.2 Friction and the Mechanisms of Friction

In general, friction refers to the resistance of two loaded contacting surfaces to slide. The frictional force F_f is the tangential force resisting the relative motion of two surfaces, which are pressed against each other with a normal force F_n. The constant of proportionality between F_f and F_n is referred to as the coefficient of friction μ, written as

$$F_f = \mu F_n \tag{1.1}$$

and is dependent on the material and on whether the bodies are at rest (in a state of sticking) μ_s or in motion (state of sliding) μ_k. The first published studies on friction were

by Amontons [1699] and Coulomb [1781], who are credited with the development of the classical friction law given in Eq. (1.1).

In order to successfully model interparticle frictional effects it is necessary to understand the mechanisms of friction. Although there are many theories concerning the mechanisms of friction [Anand, 1993; Suh and Sin, 1981], as shown in the block diagram in Figure 1.3, the major contributing factors to the friction force are the combined effects of adhesion, elastic-plastic asperity deformation, and plowing by wear particles. Asperities are the sharp or rugged points on a macroscopically flat surface and are the origins of surface friction and wear. The relative contribution of these various mechanisms show in Figure 1.3 depends on the condition of the sliding interface. From experiments, Suh and Sin [1981] observed that the coefficient of friction is a function of the sliding distance between contacting surfaces and could be divided into six primary stages of frictional phenomena. As shown in Figure 1.4, the stages include initial plowing of the surface by asperities, adhesion, plastic deformation, removal of asperities, and a steady state condition. Therefore, the friction force changes significantly during sliding before steady state frictional behavior is reached, suggesting that frictional behavior depends not only on adhesion but also on the history of sliding. The time dependent nature of the coefficient of friction is an area where little research has been focused.

Variations of the friction coefficient under extremely light loads from those at higher loads suggest that the mechanisms of friction may depend on the scale of the interaction. There is interest to understand frictional behavior at the micro- and nanoscale in order to gain additional insight into the fundamental causes of friction. As

shown in Figure 1.5, real surfaces are usually not smooth, therefore contact only takes place at the tops of the asperities during sliding indicating that the real area of contact is smaller than the apparent area of contact.

In 1958, Bowden and Tabor presented an adhesion model for friction at the micrometer scale. This model differs from the original Amontons-Coulomb model in that it assumes the frictional force is proportional to both the real area of contact A_r, due to asperities, and shear

strength at the interface τ_f, such that

$$F_f = \tau_f A_r . \tag{1.2}$$

In this formulation, the contact area is dependent on the applied normal load, the particle radius, and the elastic properties of the material. The shear strength is defined as the shear force per unit area required to cause sliding along the interface.

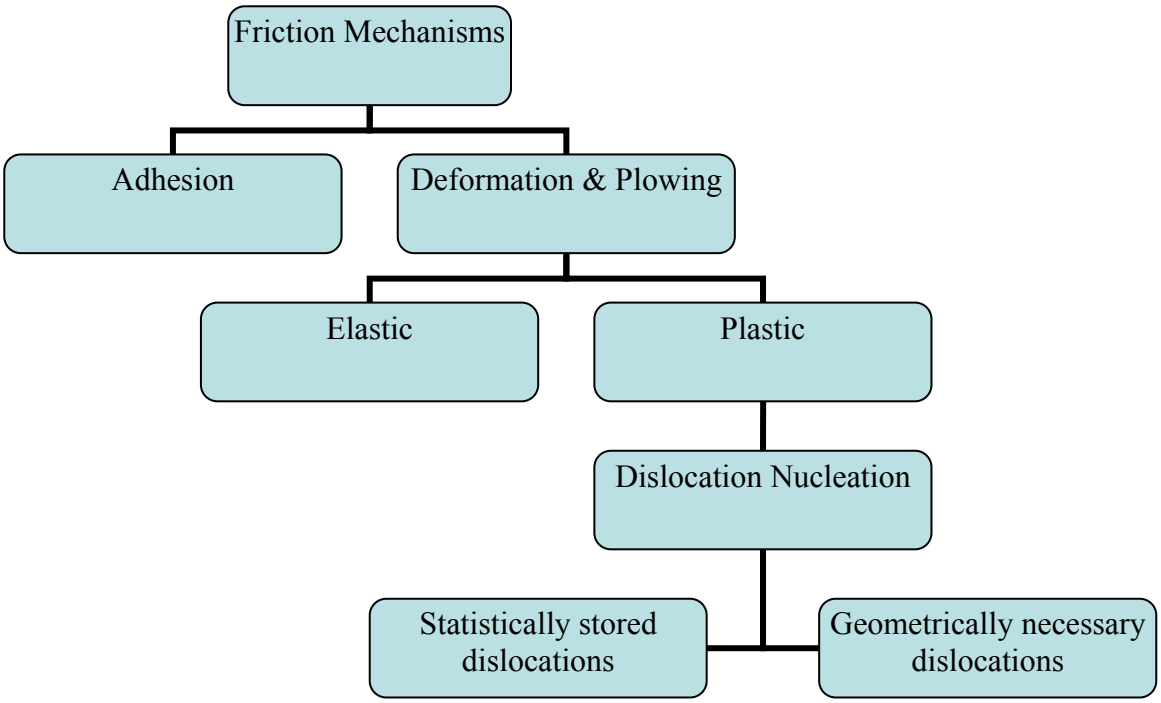

Figure 1.3 Block diagram of friction mechanisms and the generation and propagation of dislocations during plastic deformation. [Modified from Bhushan and Nosonovsky, 2003]

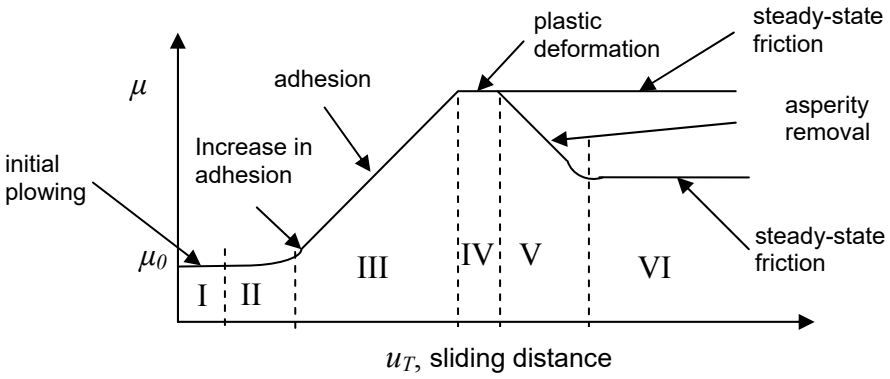

Figure 1.4 Six stages in the frictional force vs. sliding distance relation [Reprinted from Suh and Sin, 1981].

Experimental studies performed by Tambe and Bhushan [2005] on the mechanisms of friction explain the differences in friction measured experimentally at the different size scales. They identified the primary sources of nanoscale friction force as

interfacial adhesion between contacting asperities, the energy required for deformation of contacting asperities during relative motion, and stick-slip. The stick-slip phenomenon was first presented by Tomlinson [1929] and refers to alternating adhesion and sliding at the contact. The stick-slip effect is typically characterized by a sawtooth pattern in atomic scale models or experiments, as demonstrated in Figure 1.6 by the molecular statics simulation results of Kim and Suh [1994] for argon.

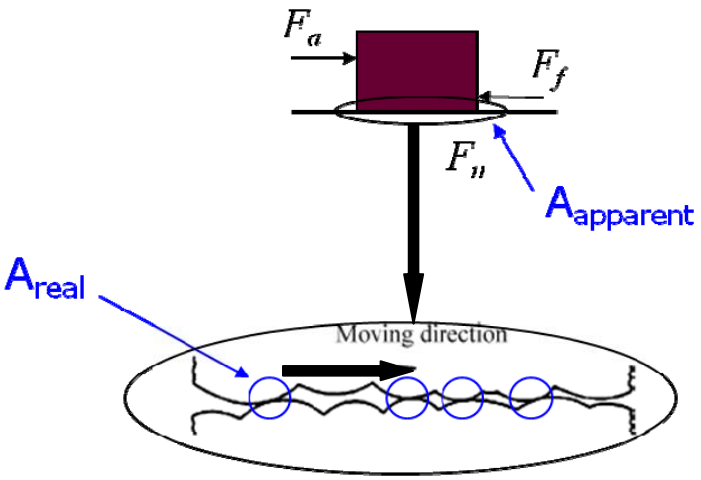

Figure 1.5 Real area of contact only takes place at the tops of the asperities during sliding.

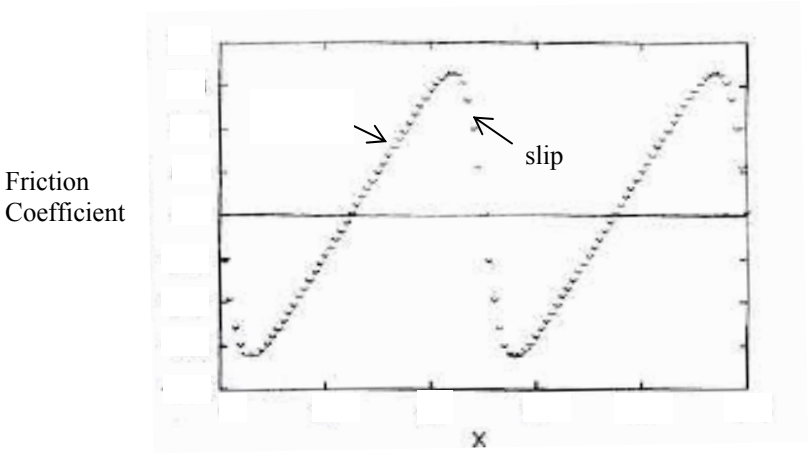

Figure 1.6 Molecular statics simulation results for Argon indicating a stick-slip effect characterized by a sawtooth pattern for the friction coefficient vs. displacement. [Reprinted from Kim and Suh, 1994].

1.3 Research Objective

The purpose of this research is to use a multiscale computational methodology to develop an internal state variable (ISV) model that captures frictional effects during the compaction of particulate materials. By using atomistic simulations we adequately capture the material behavior and effects of friction at the nanoscale. The main contribution of this research will be the addition of a friction constitutive relation to the Bammann-Chiesa-Johnson (BCJ) plasticity model [Bammann, 1990; Bammann et al., 1993] that takes into account the effect of the evolution of the hardening at the contact surface due to friction during deformation.

1.4 Dissertation Structure

Chapter I was a general introduction to the dissertation and provided the motivation behind this work and a review on the current state of multiscale friction modeling and the mechanisms of friction. Chapter II presents an overview of the general

concept of multiscale material modeling which is followed by a brief background on the MD simulation, the BCJ plasticity model, and constitutive models for particulate materials. Chapter III presents results from a two particle friction study using MD simulations and introduces a scale dependent friction relation to be included in the constitutive model for the ISV formulation. Chapter IV presents the development of a hierarchical multiscale friction model using the length scale relation from the MD simulations in an ISV framework to describe the evolution of friction hardening or softening in terms of the particle deformation. The last part of Chapter IV extends the interface friction model to represent the microstructural changes due to the particle interactions in a macroscale continuum framework. Chapter V presents conclusions and recommendations for future work.

CHAPTER II

OVERVIEW OF THEORIES AND APPROACHES

2.1 Overview of Multiscale Material Modeling

Multiscale material modeling involves performing simulations across several characteristic length and time scales. The length scales can range from the atomic level (10^{-9} m) level to the macro level (10^{-4}~10^{-2} m) with time scales varying from femtoseconds (10^{-15}) to quasi-static regimes. As shown in Figure 2.1, different modeling methods are used to perform simulations across the different scales.

Several constitutive model methodologies are used in modeling the powder metallurgy processes. These methods may be classified on the basis of length scales. At the nanoscale Molecular Dynamics simulations are used to study atomic interactions and can simulate up to 10^9 atoms and a length scale of 100 nm. Dislocation Dynamics methods are used to study dislocation motion, interactions and dislocation structure formation. At the micron scale, discrete element models analyze multi-particle behavior using numerical simulation of individual particles based on prescribed contact conditions. At the macroscale, the effects of defects and microstructures on plastic deformation and fracture using only a few representative internal state variables are incorporated into the constitutive equations for continuum models.

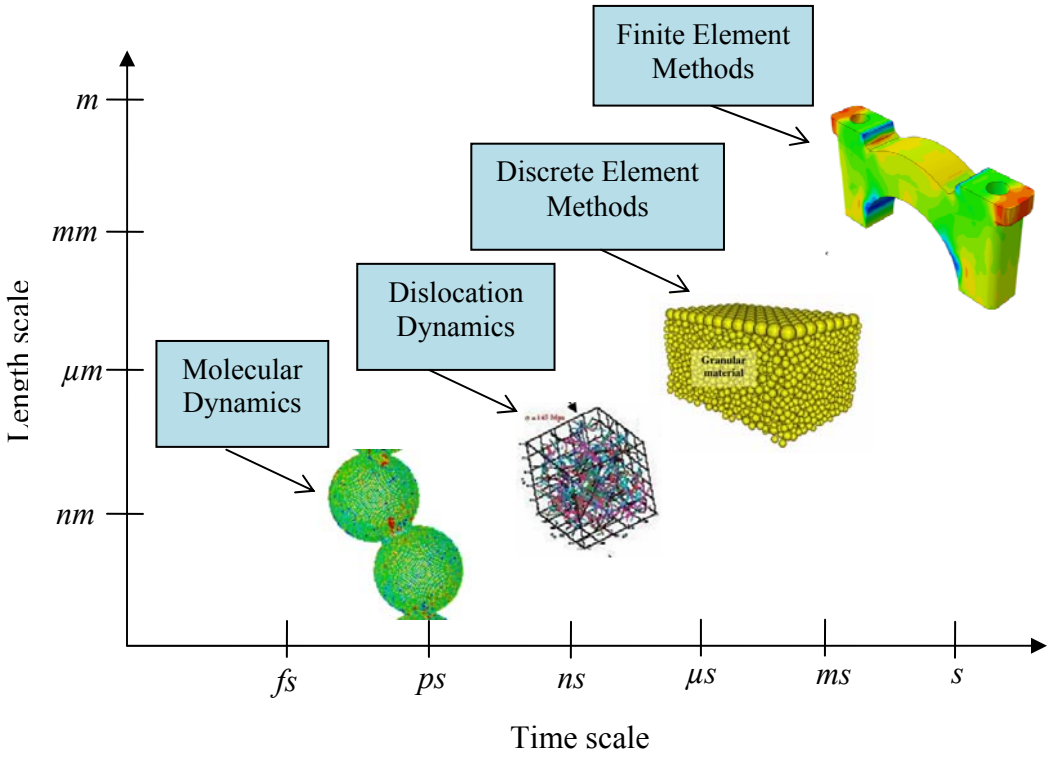

Figure 2.1 The modeling methods at different length scale and time scale.

In the current formulation, we use a hierarchical approach to link information from one scale to another. In the hierarchical approach, large-scale models use coarse-grained representations with information obtained from more detailed, small-scale models. In the hierarchical methods, simulations are run independent of the others, and the appropriate higher length scale *effects* from the lower length scale *causes* must be determined. The idea is to reduce the degrees of freedom for the higher scale analyses because too many degrees of freedom make the solution of a structural scale boundary value problem almost impossible.

2.2 Overview of Molecular Dynamic (MD) Simulations

The Molecular Dynamics simulation methods have been used to study dynamic systems of particles since the 1960s [Gullett et al., 2004]. In MD simulations, interatomic forces that move the atoms and reflect the quantum-mechanical chemical bonding are calculated. These forces are most often obtained from interatomic potentials based on a metal's lattice parameter, cohesive and vacancy formation energies, and elastic constants. Molecular dynamics codes perform the energy, force, and stress calculations based on the chosen potential. In the current study, we used the MD simulation code WARP [Plimpton, 1995]. In this MD simulation code, the equations of motion are derived based on Newton's Second Law of Motion for an N atom system

$$F_i^{\alpha} = m_{\alpha}\ddot{x}_i^{\alpha} \quad \text{i=1,2,3 and } \alpha\text{=1,2…N} \tag{2.1}$$

where F_i^{α} denotes the force in the ith direction acting on atom α; m_{α} denotes the atom's mass and x_i^{α} denotes the ith component of the atom's position. The force F_i^{α} can also be described as the derivative of the total potential energy E with respect to the position of the atom α,

$$F_i^{\alpha} = -\frac{\partial E}{\partial x_i^{\alpha}} \tag{2.2}$$

The notion of embedding energy was first proposed by Friedel [1952] and further developed by Stott and Zaremba [1980]. Daw and Baskes [1984] proposed a numerical method for calculating atomic energies for metals. Daw et al. [1993] summarized many applications of EAM. The EAM potentials are based on a semi-empirical method for which the total energy is equal to the embedding energy F, which is a function of the

electron density ρ due to neighboring atoms, plus the addition of the potential energy term φ,

$$E = \sum_i F^i \left(\sum_{i \neq j} \rho^i (r^{ij}) \right) + \tfrac{1}{2} \sum_{ij} \varphi^{ij} (r^{ij}) , \tag{2.3}$$

where i refers to the atom in question and j refers to the neighboring atoms. The EAM potential used in this study for nickel is described in Foiles et al. [1986]. The EAM potential describes the bonding of an atom in terms of the local electronic density and incorporates electrostatic and repulsive interactions between atoms. The force vector between atoms i and j is defined as

$$f_{ij}^k = \frac{\partial E}{\partial r_{ij}^k} , \tag{2.4}$$

where r_{ij}^k is a position vector between atoms. The number of superscripts denote the rank of the tensor and the subscripts denote the atom counting system. From the atomic forces, the stress tensor at atom i is calculated as

$$\beta_i^{km} = \frac{1}{\Omega_i} \sum_{j \neq i}^{N} f_{ij}^k r_{ij}^m , \tag{2.5}$$

where N is the number of nearest neighbor atoms, and Ω_i is the atomic volume.

Because MD simulations output information such as stresses and forces is in terms of each atom, estimations are often made for bulk stress calculations for comparison with macroscale mechanical properties. A continuum-like stress tensor is defined for the bulk specimen as,

$$\sigma^{km} = \frac{1}{N^*} \sum_{i=1}^{N^*} \beta_i^{km} . \tag{2.6}$$

Another common output parameter is the centrosymmetry parameter. The centrosymmetry parameter of a given atom provides a measure of the level of disturbance of that atom's environment from the symmetric crystal structure. The formula for the parameter for an FCC crystal is [Kelchner et al., 1998]

$$C_{\alpha}^{FCC} = \sum_{\beta=1}^{6} \left| \vec{r}_{\alpha,\beta} + \vec{r}_{\alpha,\beta+6} \right|^2 , \tag{2.7}$$

where α and β are atom indices and $\vec{r}$ are vectors corresponding to the size pairs of opposite nearest neighbors in the fcc lattice. The summation is taken over the six pairs of opposing neighbors of an atom. For an atom in a perfect FCC structure, the centrosymmetry parameter is zero. By plotting the atoms with a centrosymmetry parameter larger than some cutoff value (2.0 for this study), we can visualize the dislocation structure of the deforming material.

2.3 Overview of Particulate Material Constitutive Models

A constitutive law describes how a material strains or deforms both elastically and plastically when it is stressed. The response of the material to the state of stress is described by a yield surface expressed in terms of stress space. The equation of the yield surface is defined such that the state of stress inside the surface is elastic, while the stress state on the surface represents the yield point. Further deformation beyond the yield point causes the stress state to remain on the yield surface however the yield surface may change shape or size with continued plastic deformation.

Yield surfaces for particulate materials are typically expressed in terms of 3-D principal stress space (σ_1, σ_2, σ_3) or in terms of the stress invariants I_1 and J_2. The first invariant of the Cauchy stress is defined as

$$I_1 = Tr(\underline{\sigma}). \tag{2.8}$$

The second invariant of the deviatoric part of the Cauchy stress J_2, also known as the von Mises equivalent stress, is defined as

$$J_2 = \frac{1}{2}\underline{\sigma'} : \underline{\sigma'} \tag{2.9}$$

where the deviatoric stress tensor $\underline{\sigma'}$ is defined as

$$\underline{\sigma'} = \underline{\sigma} - \frac{1}{3}Tr(\underline{\sigma})\underline{I} \ . \tag{2.10}$$

For the particulate models discussed herein, the yield surfaces are depicted on hydrostatic pressure p and deviatoric stress q axes, where

$$p = -\frac{1}{3}I_1 = -\frac{1}{3}Tr(\underline{\sigma}) \quad \text{and} \tag{2.11}$$

$$q = \sqrt{3J_2} = \sqrt{\frac{3}{2}\underline{\sigma'} : \underline{\sigma'}}\,. \tag{2.12}$$

Original formulations of granular material based models, such as Mohr-Coulomb and Drucker-Prager models, included interparticle friction yet assumed an associated flow rule which led to excessive dilatency and unlimited hydrostatic compression. The Drucker-Prager yield surface with a dependence on hydrostatic pressure was initially proposed by Drucker and Prager [1952] and was primarily used for characterizing the material behavior of geoscience materials (ie. soils). As shown in Figure 2.2 (a), in 3D principal stress space the Mohr-Coulomb failure surface is a cone with a hexagonal cross section, and as shown in Figure 2.2(b) the Drucker-Prager failure surface is a cone with a circular cross-section that encloses the elastic domain for the Mohr-Coulomb yield criterion. Both surfaces describe the response of a material due to shear and normal

stress, where the failure criterion is represented by the shear failure envelope. Either of these shear plasticity models can be combined with a cap hardening model to account for deformations and densification under pressure. The cap plasticity model was introduced by Drucker et al. [1957] and later modified by DiMaggio and Sandler [1991] who implemented different shapes for the Drucker-Prager model hardening cap and added a non-associated flow potential to the shear failure region.

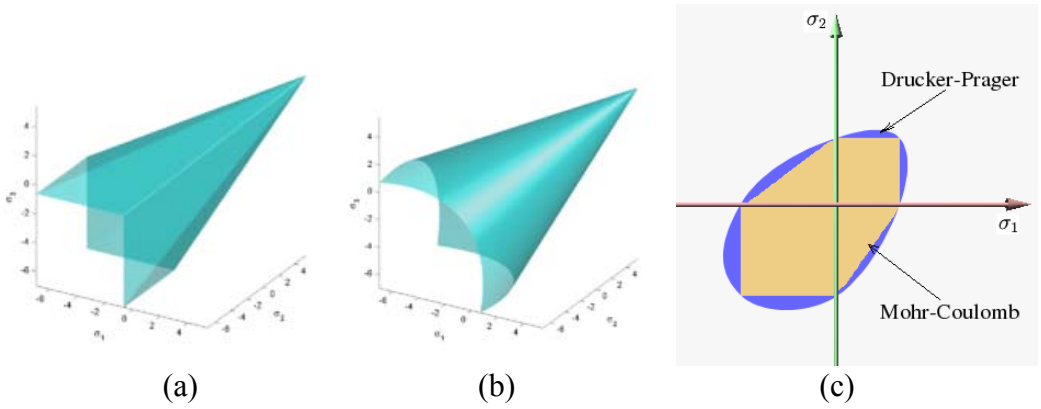

(a) (b) (c)

Figure 2.2 (a) View of Mohr-Coulomb failure surface in 3D space of principal stresses (b) View of Drucker-Prager yield surface in 3D space of principal stresses, (c) and a comparison of Drucker-Prager and Mohr-Coulomb yield surfaces in 2D principal stress space. [http://en.wikipedia.org/wiki/Yield_surface]

Thus as shown in Figure 2.3, the modified Drucker-Prager Cap Model is a double surface plasticity model consisting of an elastic region in stress space bounded by a shear yield surface, F_s, in the low pressure region which represents internal friction, and a cap yield surface, F_c, in the high pressure region which represents compression. The general equation for the shear yield surface of the model is

$$F_s = q - p\tan\varphi_f - d_0 = 0 \tag{2.13}$$

where d_0 is the material cohesion strength, φ_f is the material internal friction angle, q is the deviatoric stress, and p is the hydrostatic pressure. The cap yield surface is defined as

$$F_c = \sqrt{q^2 + \frac{1}{R^2}[p - p_a]^2} - d - (p_a - 1)\tan\varphi_f = 0, \tag{2.14}$$

where R is a material parameter called the cap eccentricity that controls the shape of the cap. The cap yield surface hardens or softens as a function of the volumetric plastic strain. Volumetric plastic compaction (when on the cap yield surface) causes hardening, while volumetric plastic dilation (when on the shear failure surface) causes softening. The Modified Drucker-Prager/ Cap model was used in the current research to formulate the macroscale continuum friction model for granular materials.

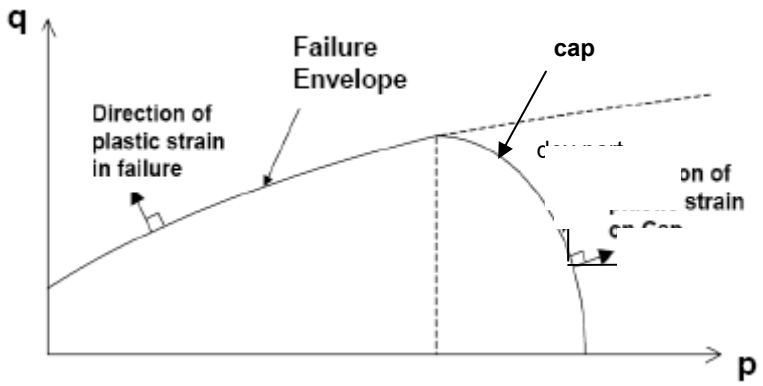

Figure 2.3 Shear failure and cap yield surfaces in p-q stress space for a particulate model.

2.4 Overview of BCJ Plasticity Model

During the powder compaction process, large material rotations and deformations occur. To describe and capture the deformation of the ductile metal particles in the continuum, we use the BCJ internal state variable (ISV) plasticity model [Bammann, 1990; Bammann et al., 1993]. ISVs are useful to model collective effects of changing

material structure involving multiple mechanisms at multiple length scales. To capture the effects in the microstructure, a representative volume element (RVE), which is a statistical representation of a material point, is used. Figure 2.4 shows the volume element with microstructural features, such as voids and dislocations, being replaced by a continuum element that describes these features using ISVs. In the BCJ plasticity model, the effect of the ISVs are captured by the plastic flow rule (commonly referred to as the plastic rate of deformation) $\underline{D}_p^d$ which, assuming a von Mises yield criterion,is expressed as

$$\underline{D}_p^d = \sqrt{\frac{3}{2}} f(\theta) \sinh\left[\frac{\sqrt{\frac{3}{2}}\left\|\underline{\sigma}' - \sqrt{\frac{2}{3}}\underline{\alpha}\right\| - \left(\kappa + \sigma_y(\theta)\right)(1-\phi)}{V(\theta)(1-\phi)}\right] \frac{\underline{\sigma}' - \sqrt{\frac{2}{3}}\underline{\alpha}}{\left\|\underline{\sigma}' - \sqrt{\frac{2}{3}}\underline{\alpha}'\right\|}. \qquad (2.15)$$

where θ is the temperature, $\underline{\alpha}$ is the kinematic hardening variable tensor, κ is the isotropic hardening variable, $f(\theta)$ is the rate dependency affecting initial yield, $V(\theta)$ is related to the magnitude of the rate dependent yield, and $\sigma_y(\theta)$ is the rate-independent yield stress. In the current study, the BCJ Plasticity model is modified to include a frictional hardening parameter in the plastic flow rule and is covered in detail in Section 4.5.

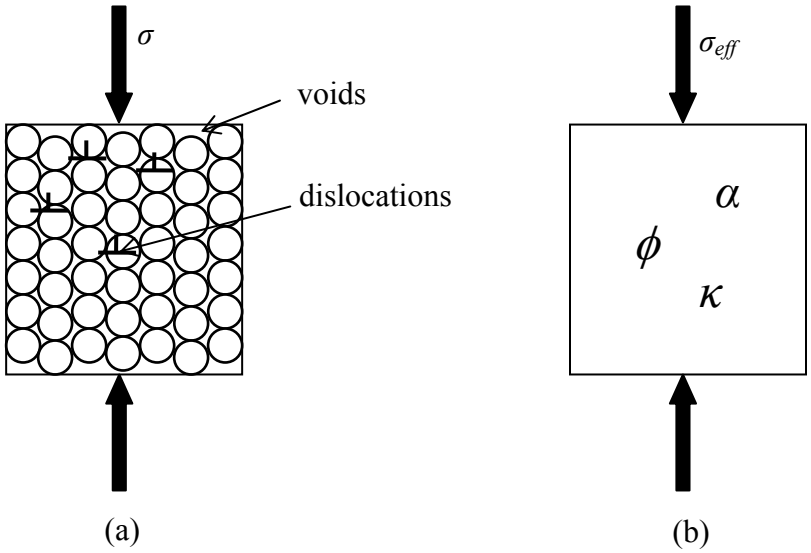

Figure 2.4 (a) Microstructural features, such as voids and dislocations, in particle model replaced by (b) a continuum element that is described by internal state variables, such as κ, $\underline{\alpha}$, and ϕ.

CHAPTER III

MULTISCALE MODELING OF FRICTION USING MOLECULAR DYNAMICS

3.1 Introduction

Beginning with the first postulates by Leonardo da Vinci in the 15th century, there have been many studies on understanding the frictional resistance between sliding surfaces. However, the the first published account by Amontons in 1699 and later studies by Coulomb in 1779 gave rise to modern macroscopic friction laws. Amontons work suggested that the friction force is dependent on the normal load and and independent of the apparent area of contact. Coulomb extended that work to show that the kinetic friction force is independent of the sliding velocity at ordinary sliding speeds. Thus, the Amontons-Coulomb law was developed as

$$F_f = \mu F_n \tag{3.1}$$

and states that the sliding friction force is proportional to the normal load but is independent of the apparent or macroscopic contact area A_a and the sliding velocity V. The frictional force F_f is the tangential force resisting the relative motion of two surfaces pressed against each other with a normal force F_n. The constant of proportionality μ is referred to as the coefficient of friction and is dependent on the material and on whether the bodies are in a state of sticking μ_s or in a state of sliding μ_k. Although early investigators, including Amontons and Coulomb, thought that friction arose from mechanical interlocking asperities, additional studies into the mechanisms of friction

disagree. Because real surfaces are usually not smooth at the microscopic level, actual contact between surfaces only takes place at the tops of the asperities during sliding, and the real microscopic area of contact is smaller than the apparent macroscopic area of contact. Based on this notion Bowden and Tabor [1950] presented an adhesion model for friction that differs from the original Amontons-Coulomb model in that it assumes friction is proportional to both the real area of contact A_r due to asperities and shear strength at the interface τ_s.

$$F_f = \tau_s A_r \tag{3.2}$$

The basis of the adhesion theory is that asperities of sliding surfaces form welded junctions with opposing surfaces during contact, and the junctions must be sheared for the surfaces to slide. Therefore, the shear force to overcome these junctions depends directly on the real area of contact which is a function of the applied normal and tangential loads. Adhesion effects are important at smaller length scales because the adhesion caused by intermolecular forces between the interfaces of materials becomes more significant. However, most theories lack the characteristic length parameters needed to capture size effects which cause surface phenomena to dominate at nano- and micro-scales.

With the development of the Surface Force Apparatus (SFA) and Atomic Force Microsope (AFM), microscale and nanoscale friction measurements became possible. Using a SFA Homola et al. [1990] experimentally obtained the friction stress at the contact between two microscale mica surfaces. Homola's research demonstrated that the frictional force is proportional to the real molecular contact area, and that the adhesion model could be used to describe the frictional behavior during atomic sliding. Later,

using AFM experiments, Carpick et al. [1996] obtained the friction stress between two nanoscale mica surfaces and determined that the friction-load relation was proportional to the area of contact predicted by the Johnson-Kendall-Roberts (JKR) theory [Johnson et al, 1971]. A comparison of the two studies revealed that the friction stress obtained using the AFM experiment was approximately 30 times larger than the values measured in the SFA experiment, suggesting a length scale effect in friction.

Because of the size dependence of friction shown experimentally [Homola et al., 1990; Carpick et al., 1996; Bhushan and Nosonovsky, 2003; Zhang et al., 2001], efforts have been made to better understand this complex process at a smaller scale using dislocation-based models. Several researchers have suggested that dislocation assisted sliding is the main mechanism responsible for the scale dependence of the shear strength at the interface for most materials. Hurtado and Kim [1999a,b] analyzed the scale dependence of friction for single asperity contacts using a discrete dislocation model and demonstrated a size dependent friction stress separated into three zones. In the first zone, the friction stress is equal to the theoretical shear strength of the solid for contact diameters less than 20 nm. In the second zone, the friction stress is equal to the Peierls stress for contact diameters between 20 nm to 20 μm. And, in the third zone, the friction stress is equal to the stress to nucleate a dislocation loop at the edge of the contact for the transition between these zones. Similarly, Bhushan and Nosonovsky [2003] considered the scale effects in friction from the nanoscale to the macroscale using a scale dependent shear strength and determined relationships for an elastic and a plastic friction coefficient as a function of a characteristic length parameter based on strain gradient plasticity and dislocation-assisted sliding. Using discrete dislocation dynamics, Deshpande et al.

[2004] analyzed the initiation of sliding in single crystals under plane strain conditions and suggested that the shear stress to initiate sliding is a function of contact size. More recently, Tambe and Bhushan [2005] decomposed nanoscale friction into several components, such as adhesion and deformation, and developed an analytical nanoscale friction model based on experiments and included a velocity dependence of the friction force.

The issue of whether friction is a thermodynamic force or kinematic variable is also an important issue when examining different size scales. In other words, some researchers have focused on the stress dependence of friction (thermodynamic force) while others have focused on the strain dependence of friction. MD simulations have revealed a size scale effect related to dislocation nucleation influencing the yield stress as a function of the volume per surface area of the specimen [Horstemeyer et al., 1998; Horstemeyer et al., 2001a,b; Gerberich et al., 2002; Horstemeyer et al., 2003]. Alternatively, other MD studies related to kinematic/geometrical effects, nanoscale fracture, and nanoscale fatigue have shown no size scale effects and have revealed self-similar, scale invariant behavior. Three examples illustrate no size scale dependence related to kinematics/geometry/strain. Horstemeyer et al. [2002] performed macroscopic single crystal experiments of copper and compared the results to MD and microscale crystal plasticity simulations for torsion and simple shear. The results showed similar strains and gradients of strain at all size scales although the stress states were different. MD, microscale crystal plasticity and macroscale internal state variable plasticity simulations were performed for the simple shear load case in [Horstemeyer et al., 2003]. These simulations clearly showed very similar strain states, but different stress states as a

function of size scale. In Solanki et al. [2005], macroscale experiments of imploding rings were compared to MD simulation results and microscale crystal plasticity simulation results, and again, the geometry changes, strain levels, and strain gradients were similar in all cases regardless of the size scale. In terms of fatigue, researchers employing MD simulations [Potirniche et al., 2005a, 2006b] have shown that nanoscale crack growth rates are similar to microcrack growth rates with the same mechanisms existing at all size scales. In terms of void growth, MD simulations [Potirniche et al., 2005b, 2006a] have showed size scale effects in the elastic regime but scale invariance quickly developed as plasticity was induced from the nucleation, movement, and interaction of dislocations. Hence the question arises regarding frictional effects on the size scale: are the frictional effects size scale dependent like the stress state or are they size scale independent like the geometric quantities or is it a combination of both?

Some MD simulations have been pursued to address such a question and to gain a more in depth understanding of the mechanisms of friction at the atomic scale. Early investigations by Landman et al. [1992] who performed MD simulations of tip-substrate systems to study adhesive interactions and their effect on wear and friction for Ni/Au and other materials revealed atomic stick-slip, material transfer, and other phenomena. MD studies were also performed by Kim and Suh [1994] to study the effect of interatomic forces on frictional behavior at the atomic-scale and to gain further insight into the fundamental causes of friction. Kim and Suh simulated AFM experiments using 2-D MD studies of argon that indicated adhesion is not the only mechanism of atomic friction as previously thought. They also observed an increase in substrate temperature due to frictional energy dissipation at the contact. Zhang and Tanaka [1997] used MD methods

to analyze the deformation of an atomic lattice caused by sliding. In comparing their results to microscale behavior, they found that slip lines generated by dislocation motion are very different from those predicted by the slip-line theory of plasticity and concluded that a new theory needed to be developed to bridge the gap between the atomic analysis and continuum mechanics. Using MD simulations Gao et al. [2004] confirmed that for nonadhering surfaces Amontons' law accurately predicted friction when compared with experimental data. Additionally, friction anisotropy at nickel interfaces have also been investigated using MD simulations [Qi et al., 2002].

In the current study, MD simulations using embedded atom method (EAM) potentials were performed to model the contact behavior of two spherical nickel nanoparticles and to study the microstructural effects of friction between the interface. Evolutions of the dislocation structures were compared for different sized particles to quantify the length scale effects of friction and the relationship between friction and the dislocation structure. Using contact laws and an adhesion law for friction, we developed a friction model that captures the atomic scale effects at the interface of the contacting surfaces from the MD simulations. The resulting interface friction model formulation combined the influence of loading angle and particle size and was validated with experimental results.

3.2 Simulation Method and Setup

MD simulations using a nickel EAM potential [Daw and Baskes, 1984; Foiles et al.,1986] were performed on two contacting single crystal nanoparticles of various sizes and contact angles subjected to a uniaxial compressive load along the y-axis which

corresponded to the [010] crystallographic direction. As shown in Figure 3.1 and Figure 3.2, the MD models consisted of two spherical fcc nickel (Ni) single crystal nanoparticles of the same diameter, *D*, (3.52 nm, 7.04 nm, 10 nm, or 14 nm). The particles had lattice orientations of <100> with origins at the particle centers. Because the models consisted of perfect lattice structures, there were no initial defects in the model. Contact angles γ of 0°, 30°, and 60° were used in the simulations and were defined as the angle between the loading axis (*y*-axis) and the normal axis of the contact surface. A half sphere was added to each end of the model to provide a fixed surface for the boundary conditions. Boundaries were defined as free surfaces in the *x*- and *z*-directions, and for each model, a few planes of atoms at the top and bottom (*xz* planes at the +*y* and –*y* extrema) of the half spheres were fixed on their perfect lattice sites.

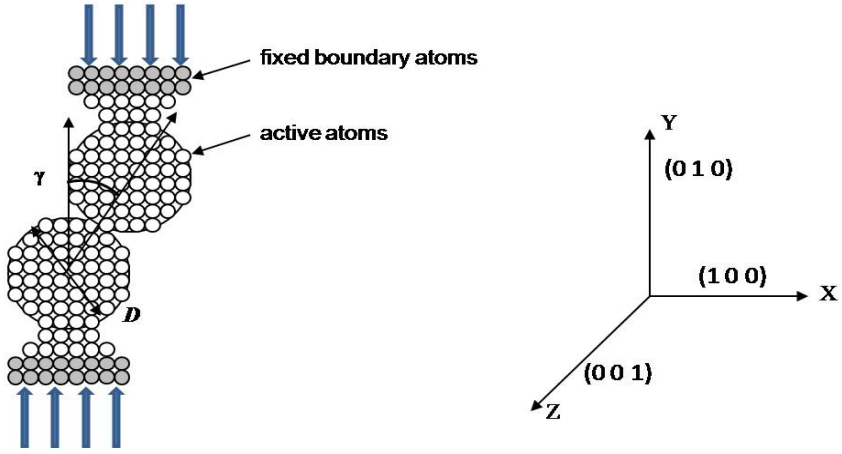

Figure 3.1. Schematic of two particle model showing active nickel atoms as white circles and fixed boundary atoms as grey. The arrows indicate the loading direction. The model setup includes contact angles of γ = 0°, 30° or 60°, diameter D=3.52, 7.04, 10 or 14.08 nm, and velocity of 0.22 nm/ps up to 20% strain. The orientation of the crystal is shown on the right.

Thermal velocities of the interior (active, non-fixed atoms) were initialized using a Boltzmann distribution at a chosen temperature of 300 K and were allowed to equilibrate for 10 ps to accommodate any surface relaxation in the system. The MD simulations were carried out using the constant volume constant temperature (NVT) conditions at a temperature of 300 K. Because moving the fixed planes of boundary atoms adds considerable energy to the active atoms, a Nosé-Hoover thermostat [Nosé, 1984; Hoover, 1985] was used during the molecular dynamics simulation to keep the active atoms at the constant temperature of 300 K. The thermostat applies a damping factor to the active atoms based on the difference between their current temperature and the desired temperature. Friction was generated by using the constant velocity method (CVM) to apply a compressive load of ±0.22 nm/ps to the upper and lower boundary atoms in the model using a linear y velocity profile given by

$$v_y = \dot{\varepsilon} y \,, \tag{3.3}$$

where the applied strain rate $\dot{\varepsilon}$ is calculated from the initial height y_{int} of the model as

$$\dot{\varepsilon} = \frac{0.22 nm / ps}{0.5 y_{\text{int}}} \,. \tag{3.4}$$

A linear velocity profile was used to avoid an initial shock to the system from an instantaneous application of velocity on the upper and lower fixed atomic planes. The interior atoms were allowed to move freely in response to the applied loading. The imposed velocity resulted in strain rates on the order of 10^8 /s. The applied strain rates were high because atomistic simulations start with an atomic frequency in which the periods are on the order of femtoseconds (10^{-15} s or fs). Therefore for smaller strain rates the MD simulations would last an inordinate amount of time. A timestep of 5 fs was

used, which is safely below the value where the dynamics becomes unstable. The models were compressed for up to 20% true strain with the applied strain at each time step calculated as

$$\varepsilon = t\dot{\varepsilon} \quad . \tag{3.5}$$

The MD simulations were performed using the MD code WARP (Plimpton, 1995) on a system of IBM Linux Superclusters using multiple parallel processors. Warp calculated the energy, force, and stress based on the chosen EAM potential for nickel [Foiles et al.,1986]. The total energy is given by the following equation

$$E = \sum_i F^i\left(\sum_{i\neq j}\rho^i(r^{ij})\right) + \tfrac{1}{2}\sum_{ij}\varphi^{ij}(r^{ij}) \quad . \tag{3.6}$$

Eq.(3.6) predicts that the total energy is equal to the embedding energy F which is a function of the electron density ρ due to neighboring atoms plus the addition of the potential energy term φ and $r_{ij}^{\ k}$ is the position vector between atoms i and j. The force between atoms is calculated from the total energy as

$$f_{ij}^{k} = \frac{\partial E}{\partial r_{ij}^{k}}, \tag{3.7}$$

where the number of superscripts denote the rank of the tensor and the subscripts denote the atom counting system. From the forces, the dipole force tensor, β, is determined for each atom and is given by

$$\beta_i^{km} = \frac{1}{\Omega_i}\sum_{j(\neq i)}^{N} f_{ij}^{k} r_{ij}^{m} \quad , \tag{3.8}$$

where N is the number of nearest neighbor atoms, r is the displacement vector, and Ω is the atomic volume. In this way β is analogous to the stress tensor at the atomic site.

Using from the MD simulations the global stress tensor over the continuum [McLellan, 1974], which is interpreted as a volume average over the specimen,

$$\sigma^{km} = \frac{1}{N}\sum^{N} \beta_i^{km} \tag{3.9}$$

where N is the total number of atoms in the specimen.

Another common output parameter is the centrosymmetry parameter. The centrosymmetry parameter provides a measure of a given atom's deviation from the symmetric crystal structure and for an FCC crystal is (Kelchner et al., 1998) given by

$$C_{\alpha}^{FCC} = \sum_{\beta=1}^{6} \left| \vec{r}_{\alpha,\beta} + \vec{r}_{\alpha,\beta+6} \right|^2 \tag{3.10}$$

where α and β are atom indices and $\vec{r}$ are vectors corresponding to the six pairs of opposite nearest neighbors in the fcc lattice. For an atom in a perfect FCC structure, the centrosymmetry parameter is zero. By plotting the atoms with a centrosymmetry parameter larger than some cutoff value (2.0 for this study), we can visualize the dislocation structure of the deforming material. Post-processing of the MD simulation data was performed using EnSight visualization software developed by Computational Engineering International (CEI), Inc.

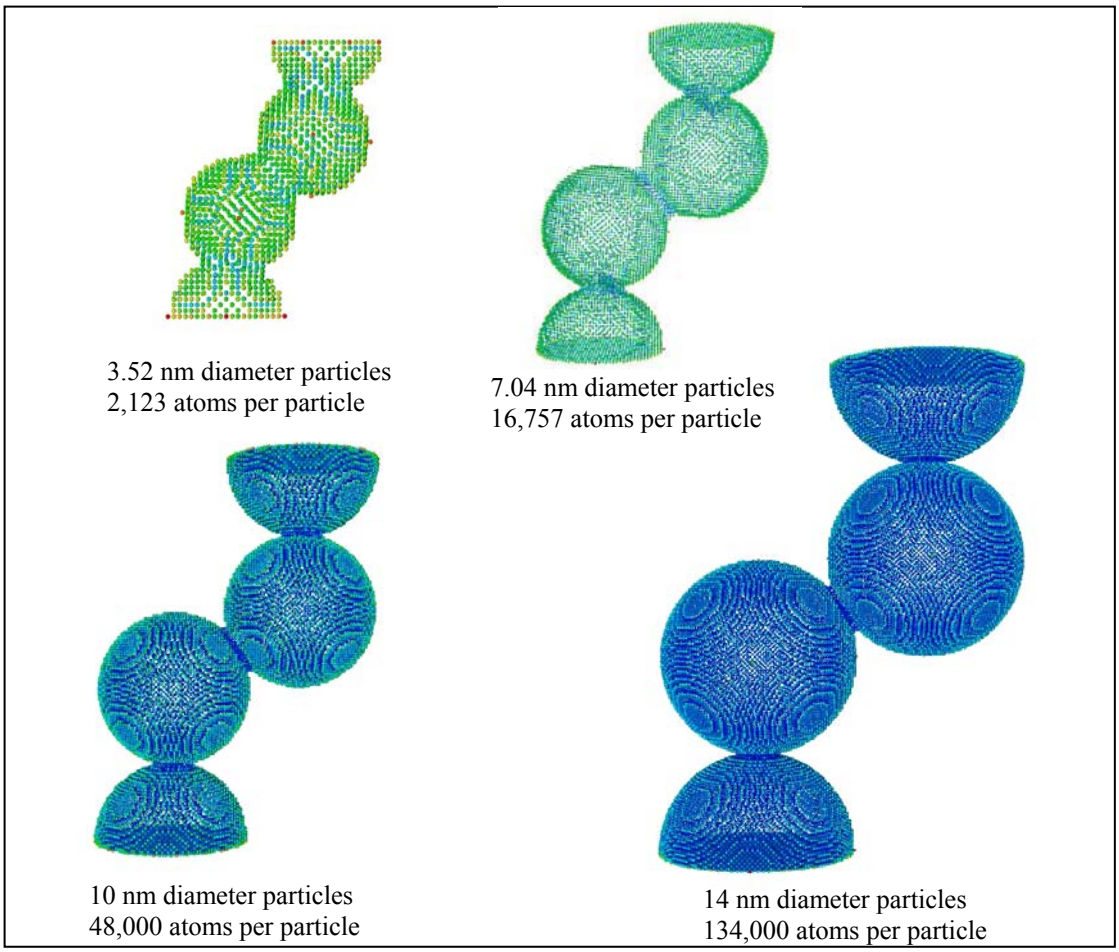

Figure 3.2. Atomic diagrams for the Ni nanoparticles with atoms in their original fcc lattice positions at 60 degree contact angle.

3.3 Results and Discussion

3.3.1 Stress-Strain Response

After the models were allowed to thermally equilibrate, we observed that stresses remained in the particles. This effect has been similarly reported by other researchers [Koh and Lee, 2006] in unstretched Au and Pt nanowires. In their simulations, Koh and Lee [2006] observed initial tensile stresses and determined that the magnitude of the initial stresses varied inversely with the proportion of surface atoms. They attributed the

presence of the initial stresses to surface relaxation in fcc transition metals. Because the surface atoms have a higher electronic cohesive energy than the interior atoms, the unrestrained surfaces tended to contract while the restrained surfaces built up tensile forces. This effect is due to the high proportion of surface atoms in the nanoscale model indicated by a low volume-per-surface-area ratio as shown in Figure 3.3 for the current simulations. As the volume-per-surface-area increases, which corresponds to an increase in particle size, the initial stresses decrease. In the MD particle models the initial stress state included shear stresses as well as tensile stresses due to the offset angle of the contacting particles. When the contact angle is zero, only initial tensile stresses were present in the model. Figure 3.3 demonstrates the relationship between the initial stresses and the volume per surface area in the MD simulation models. As indicated in Figure 3.3, both initial tension and shear stresses increased as the size of the particles decreased. It is also apparent that only the initial tensile stresses are influenced by the contact angle. As the contact angle increased, the initial tensile stresses present in the model decreased. Thus, there is a pre-existing strain in the simulation, and the simulations were started in a pre-stressed condition. To account for this effect, when the model reached equilibrium, after approximately 2% strain, the strain was reset to zero. Therefore, the initial stresses were excluded from the MD simulation results analysis.

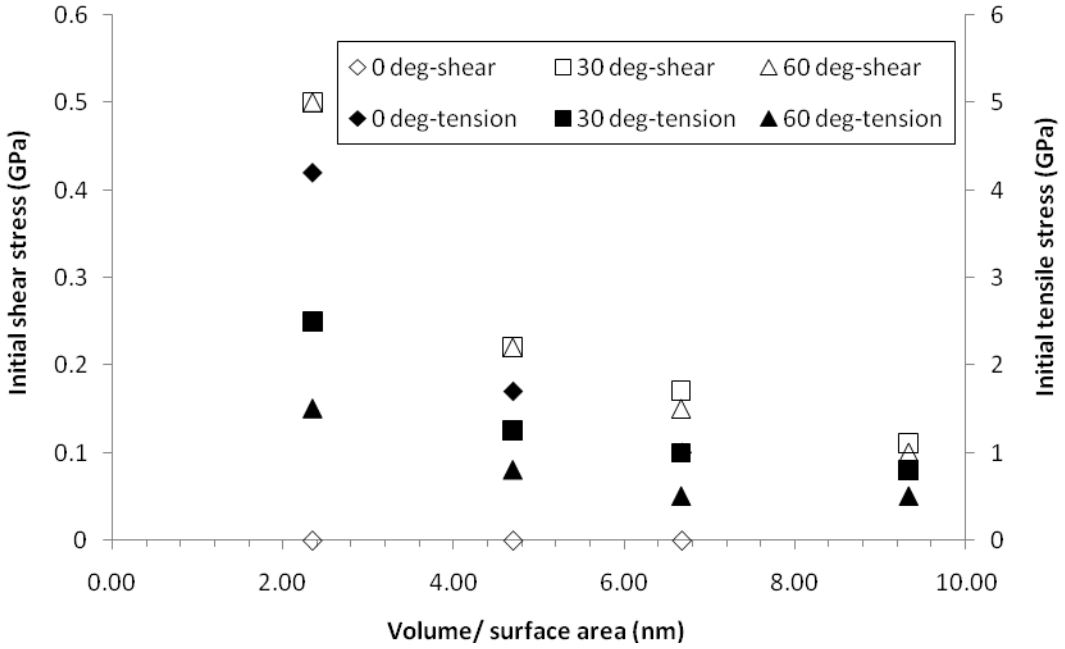

Figure 3.3. Effect of the particle size and contact angle on the initial stresses in the nanoscale model after 10 ps of thermal equilibrium.

As shown by other researchers [Horstemeyer et al., 2001a] the stress-strain behavior for the atomic simulations differ from macroscale behavior. Fluctuations due to thermal vibrations of the active atoms in addition to the micro-yield points due to dislocations initiating within the material prior to the maximum stress at the macro-yield point cause these differences. Horstemeyer et al. [2001a] showed by unloading atomic blocks of nickel at the microyield points that only the macro-yield points lead to plastic behavior and permanent deformation. The shear stress-strain responses for the current simulations are provided in Figures 3.4- 3.11 and show the shear stress-strain response and the related atomic positions based on particle size and contact angle. The stress-strain curves were generated by plotting the average global shear stress of the active atoms of the center spherical particles as a function of applied strain. The average shear stress σ_{xy} is determined from Eq. (3.9). For the 3 nm and 7 nm models in Figures 3.4-

3.7, the snapshots include all atoms in the model with the color of the atoms indicating the atomic shear stress β_{xy}^{i} (determined from Eq. (3.8). Because of the large number of atoms in the 10 nm and 14 nm models, the atomic shear stress shown in Figures 3.8- 3.11 includes only those atoms with a centrosymmetry parameter greater than 2.0. In general the stress-strain response of the different size models is similar in character. The shear stress increases as the specimens deform elastically until a single partial dislocation starts to nucleate from the particle boundary causing a slight drop in shear stress. The shear stress continues to increase with applied strain until the yield point is reached, followed by a sharp drop in shear stress corresponding to dislocation glide across slip planes within the crystalline structure. With continued deformation the shear stress again increases until the maximum shear stress is reached which is again followed by a drop in shear stress as new dislocations are emitted and glide across the particle and either form a step on the other side or, as observed in some instances, leave behind a stacking fault. Dislocation structure formation and its relation to slip is discussed in detail in the next section. This oscillating behavior of the shear stress dropping and peaking continues with increasing strain for the duration of the simulations. The sawtooth pattern of the shear stress-strain response is similar to that observed for the stick-slip behavior of nanoscale friction [Tomlinson, 1929].

From the plots and corresponding model snapshots at different stages of deformation it is apparent that the maximum negative shear stress, shown in red in the snapshots, indicates the slip resistance at the interface τ_f. The maximum global shear stress typically occurs within the interface region and influences the average shear stress response of the particles. For each model configuration, we obtained the friction stress by

averaging the atomic shear stress for the interface at the onset of slippage. The friction stress measurements from the MD simulations revealed a length scale dependence. The friction stress values are indicated on the average particle stress-strain plots in Figures 3.4- 3.11 and are also included in Table 3.1. Because of the difficulty (of the tedious nature) in obtaining the friction stress from the MD simulations, we obtained the following approximation for the friction stress based on the stress-strain plots

$$\tau_f = \sigma_{xy}^{\max} \tag{3.11}$$

where $\sigma_{xy}^{\max}$ is the maximum global shear stress of the particles.

The size dependence of the shear yield stress implies a size dependence of the shear strength at the interface as suggested by other researchers [Fang et al., 2004]. The shear yield stress from the curves are size dependent as indicated in the summary of results in Table 3.1 and agree with previous findings of Horstemeyer et al. [1998, 2001]. Additionally, the material properties from the MD simulation are provided for each model configuration and include the effective shear modulus (due to the particulate nature of the models), the shear yield stress, the normalized shear yield stress, and the friction stress are included in Table 3.1. As shown in Figure 3.12, the normalized shear yield stress from the current MD simulations compares well with the size scale effect demonstrated by previous experimental and atomistic simulation data. As the size of the material decreases, the shear yield stress approaches the maximum crystalline strength or the normalized theoretical shear strength of the material, which is 0.2 for nickel.

Table 3.1 Material properties from the MD simulations.

Particle size (nm)	Contact Angle (°)	Effective Shear Modulus, G (GPa)	Shear Yield Stress τ_y (GPa)	Normalized Shear Yield Stress τ_y/G	Friction Stress, τ_f (GPa)
3.52	30	25	1.08	0.04	1.05
3.52	60	30	1.21	0.04	1.05
7.04	30	11	0.82	0.07	0.60
7.04	60	15	0.70	0.05	0.60
10.0	30	7.8	0.55	0.07	0.50
10.0	60	7.4	0.61	0.08	0.50
14.0	30	9.7	0.55	0.06	0.45
14.0	60	9.4	0.64	0.07	0.45

Hurtado and Kim [1999a] postulated that for nanosize contacts with a radius less than 10 nm the friction stress is constant due to concurrent slip without the aid of dislocation motion. Although our MD models fall within this size range, the simulation results indicate that dislocation motion does contribute to slippage along the interface even at this small size scale. The influence of dislocation activity on the friction stress is shown to increase with specimen size even within the small nanoscale range we evaluated. Thus, the current research does appear to support suggestions from Hurtado and Kim [1999a] of a transition from primarily concurrent slip for the smallest contact model to one of dislocation assisted slip as the contact size increases. Detailed analyses on dislocation structures and mechanisms of slip observed in the current study are presented in the next section.

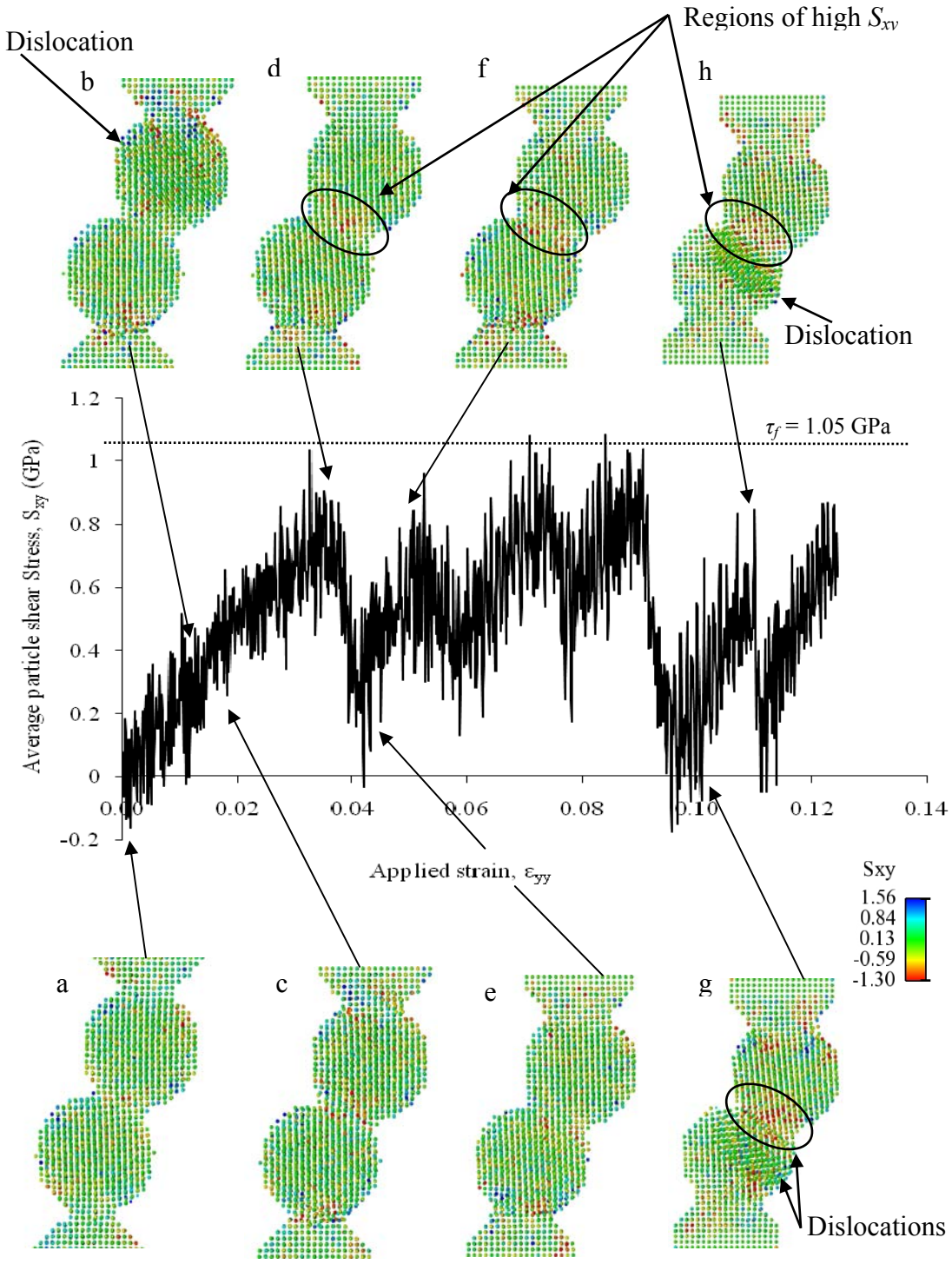

Figure 3.4 Average shear-stress strain response for 3.5 nm particles with <100> crystal lattice orientations and a 30 deg contact angle.

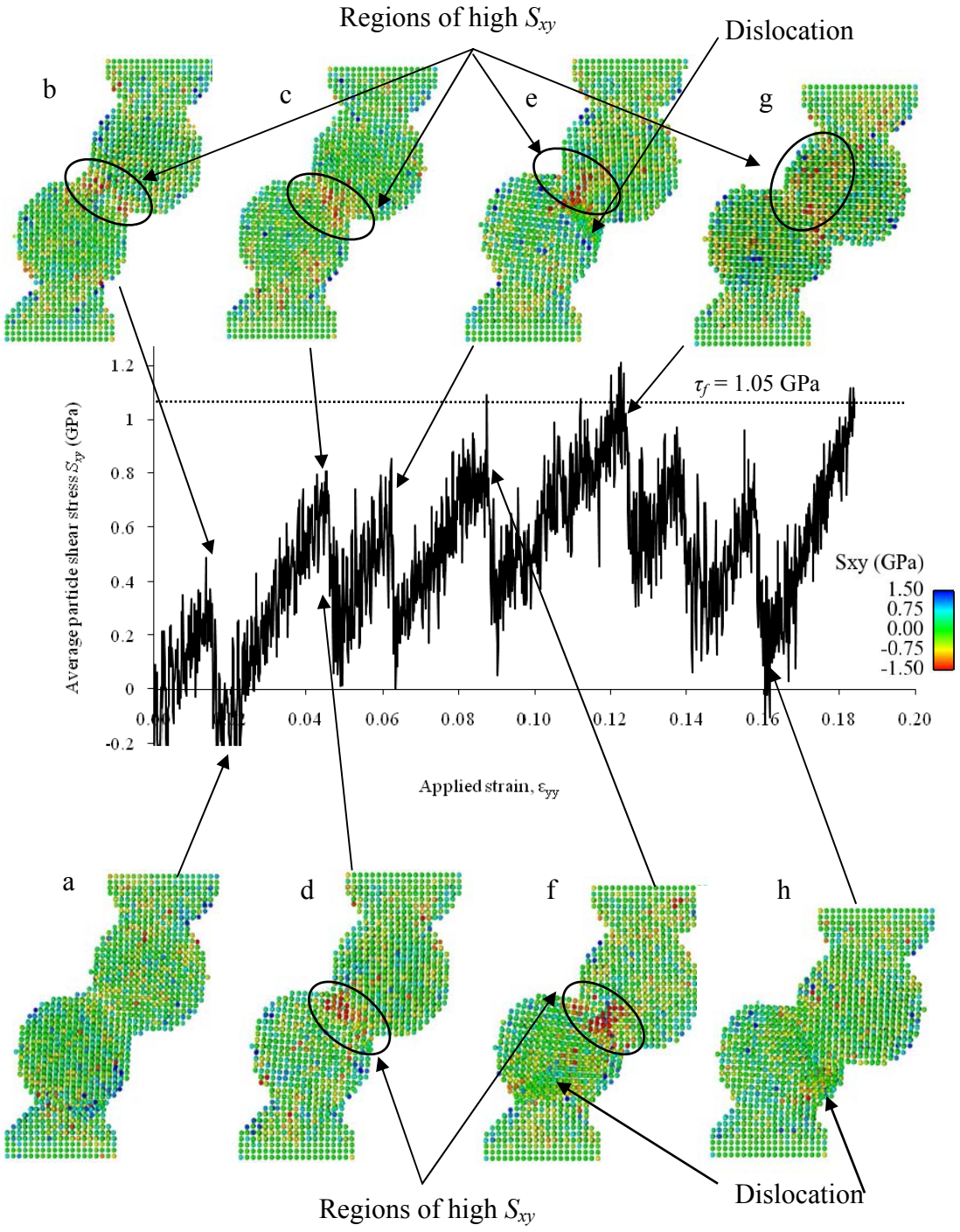

Figure 3.5 Average shear-stress strain response for 3.5 nm particles with <100> crystal lattice orientations and a 60 deg contact angle.

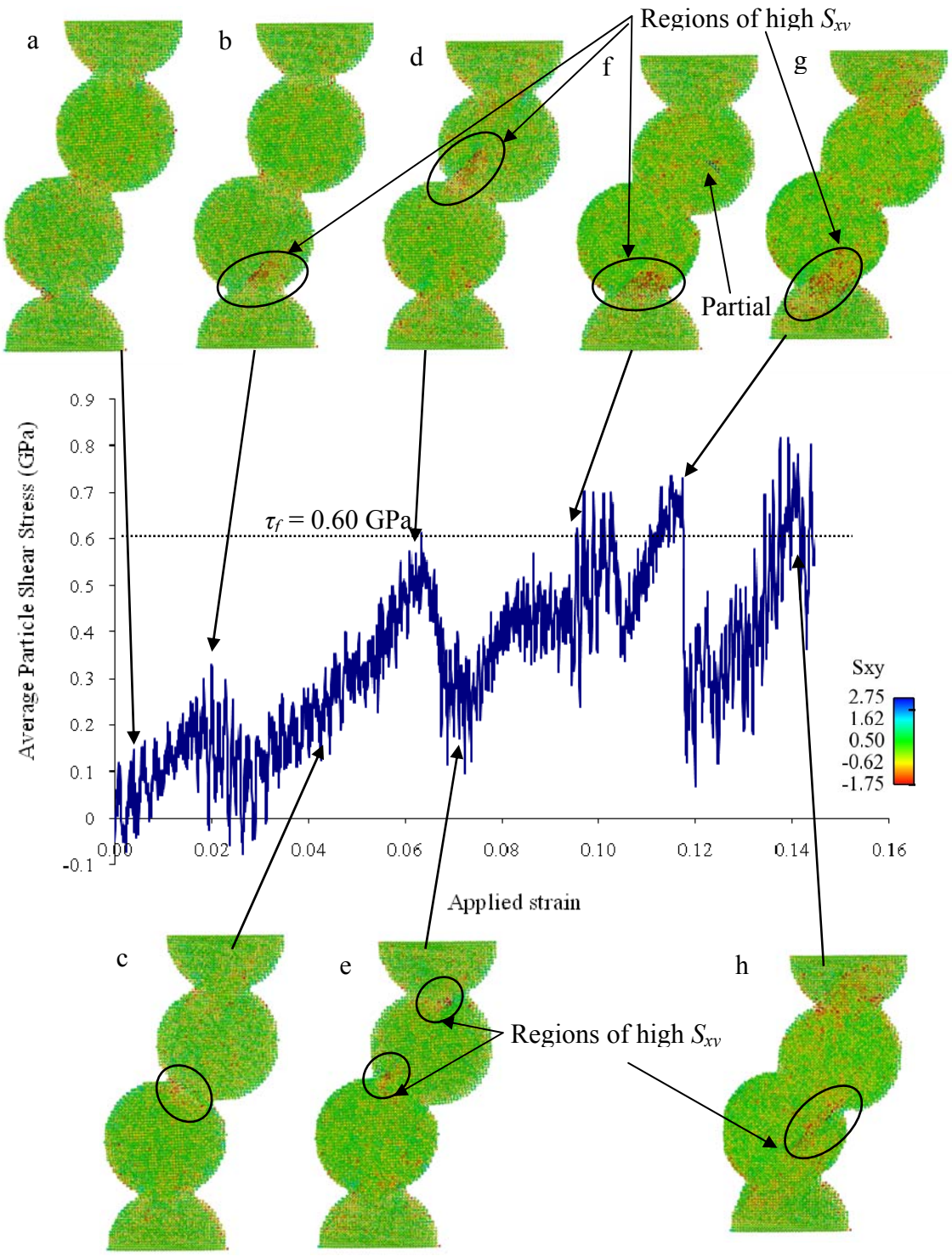

Figure 3.6 Average shear-stress strain response for 7 nm particles with <100> crystal lattice orientations and a 30 deg contact angle.

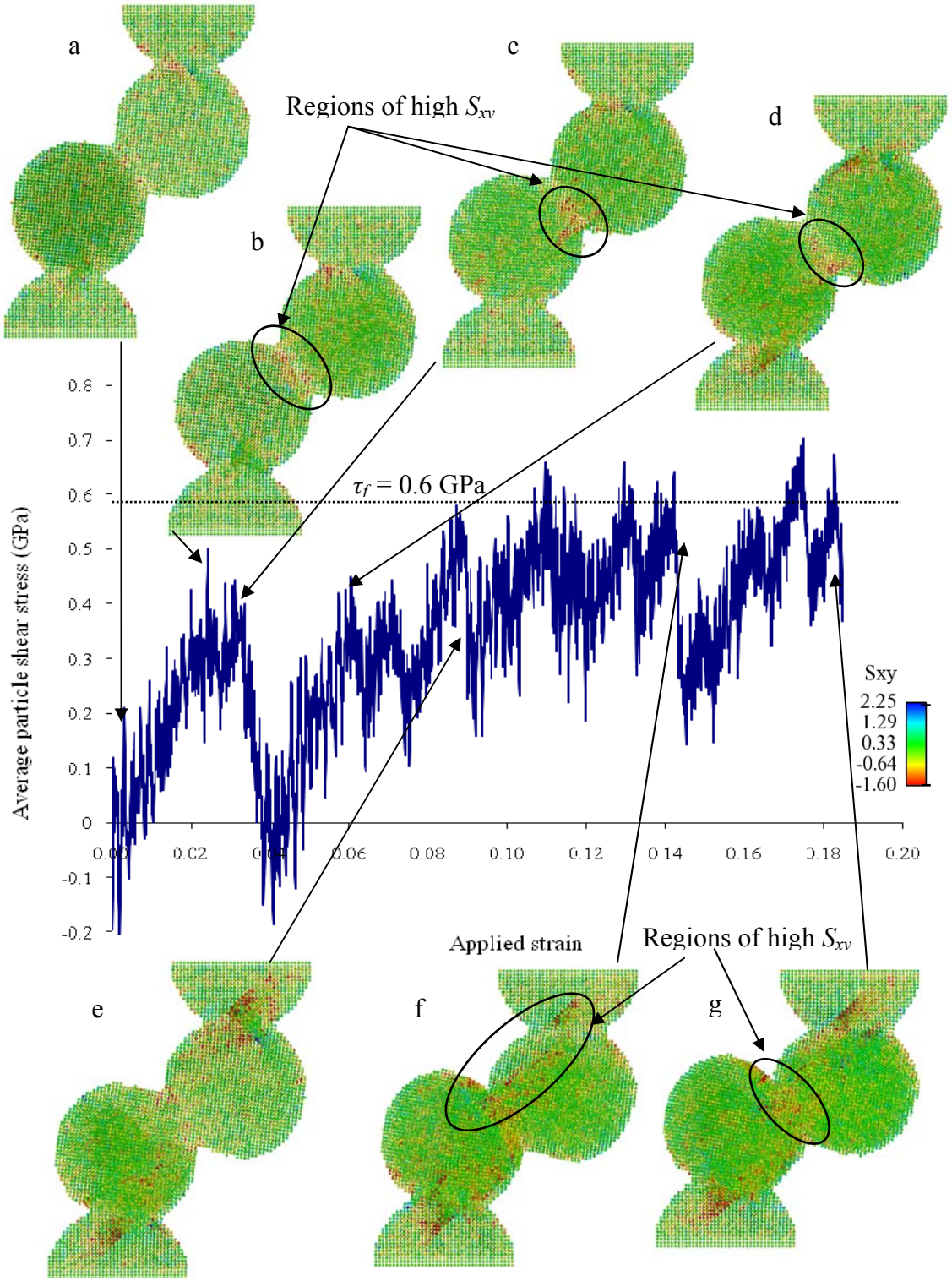

Figure 3.7 Average shear-stress strain response for 7 nm particles with <100> crystal lattice orientations and a 60 deg contact angle.

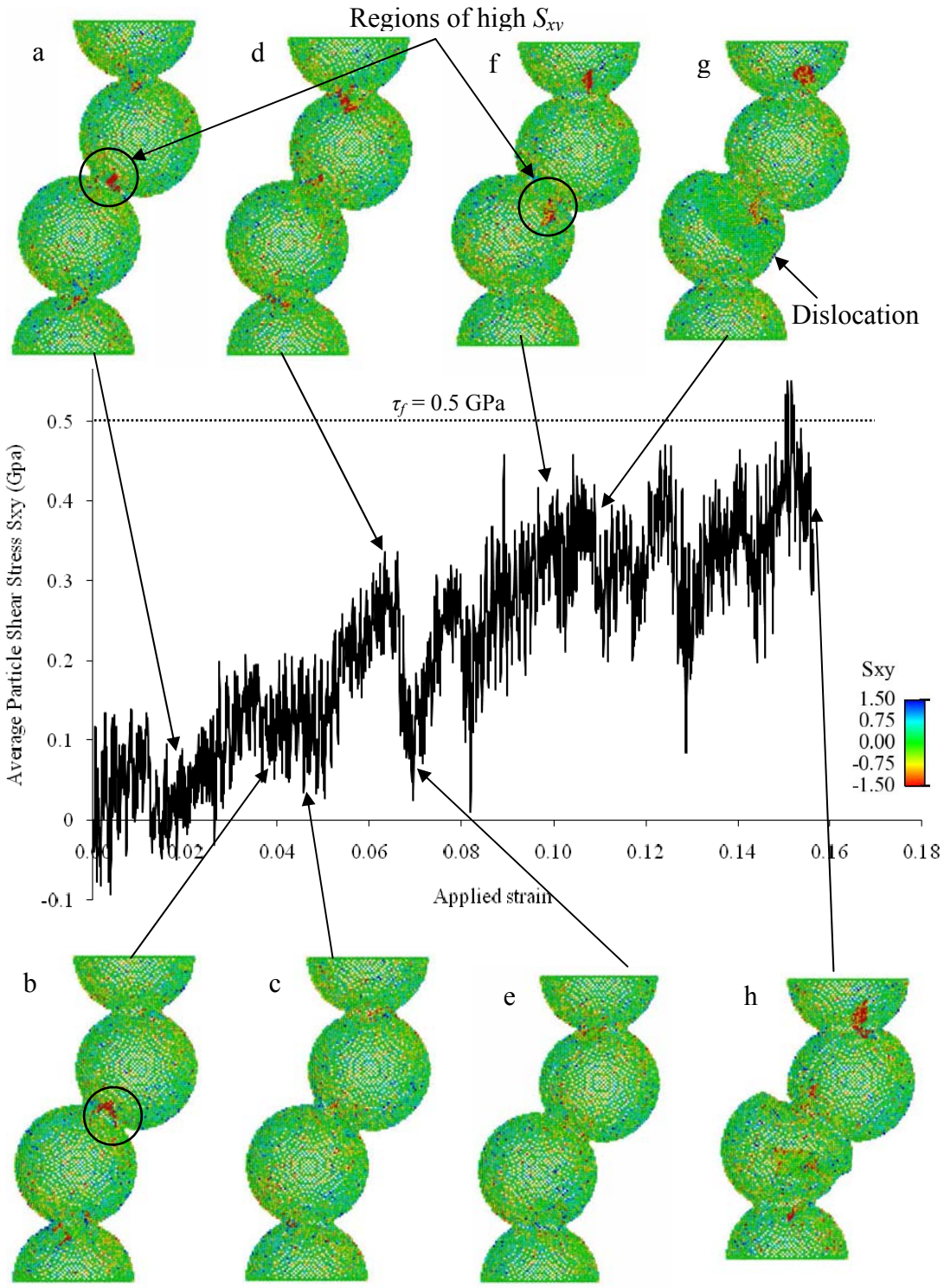

Figure 3.8 Average shear-stress strain response for 10 nm particles with <100> crystal lattice orientations and a 30 deg contact angle.

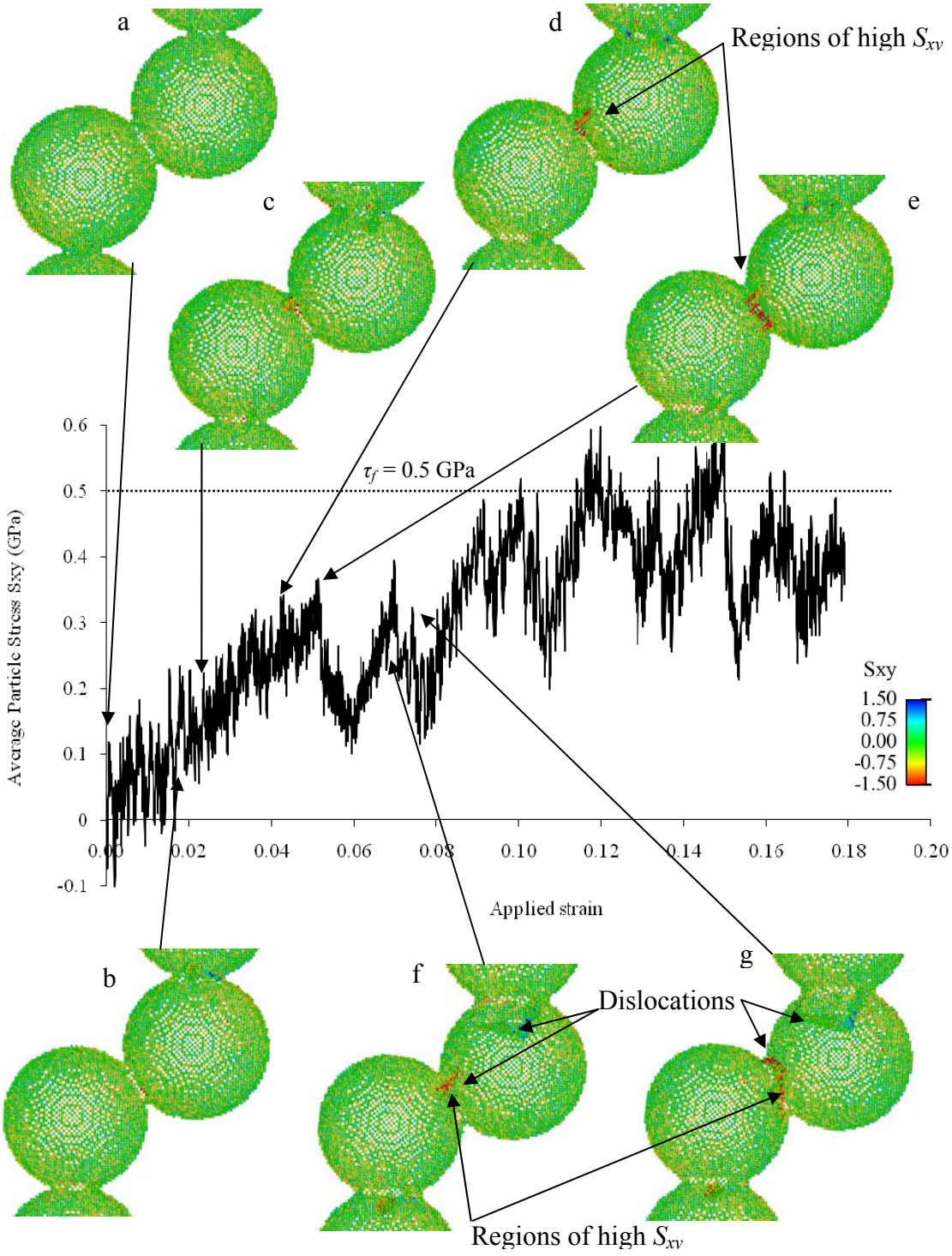

Figure 3.9 Average shear-stress strain response for 10 nm particles with <100> crystal lattice orientations and a 60 deg contact angle.

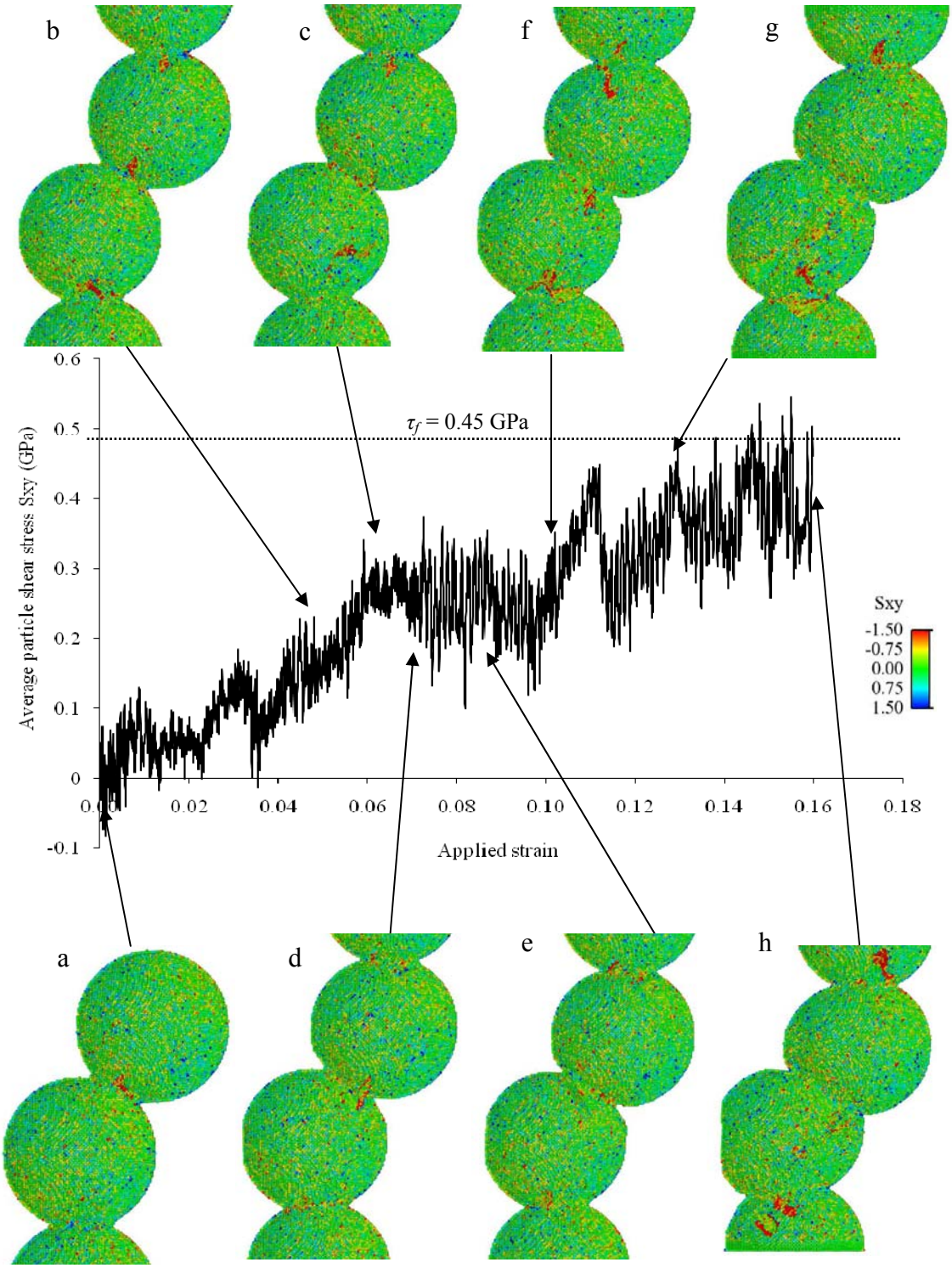

Figure 3.10 Average shear-stress strain response for 14 nm particles with <100> crystal lattice orientations and a 30 deg contact angle.

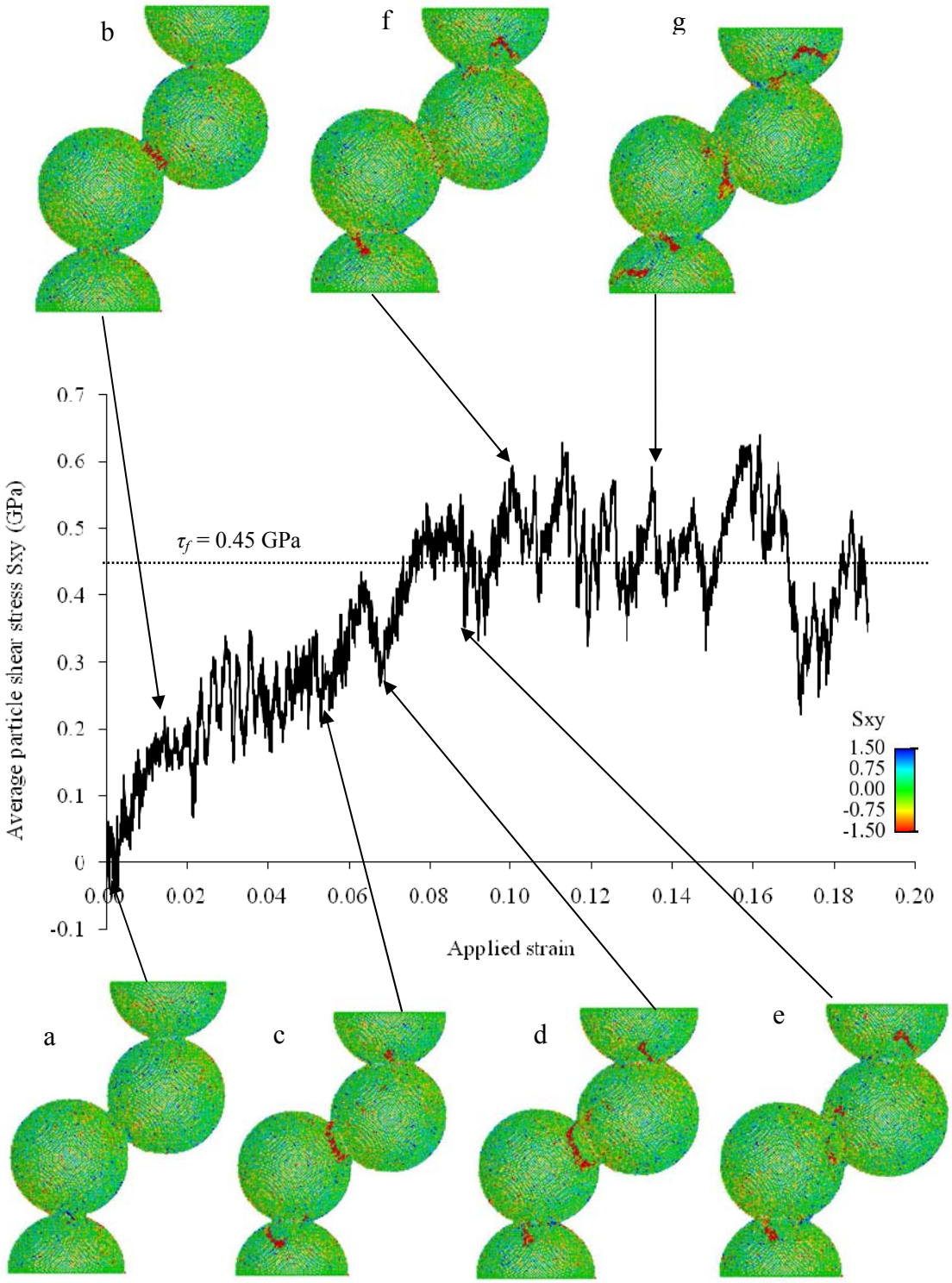

Figure 3.11 Average shear-stress strain response for 14 nm particles with <100> crystal lattice orientations and a 60 deg contact angle.

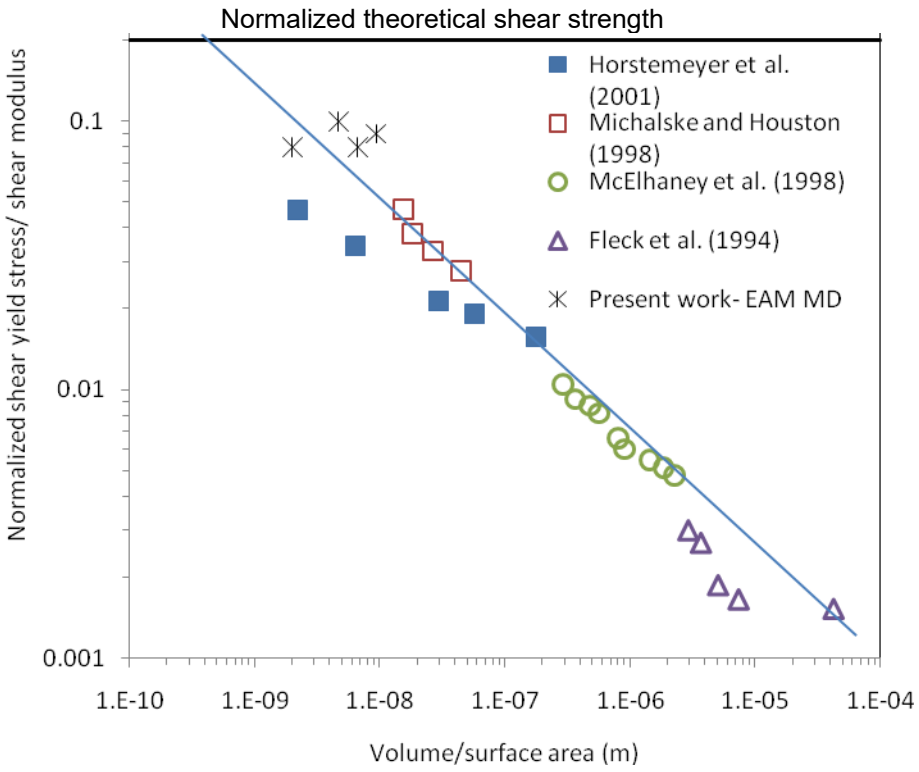

Figure 3.12 Log-log shear yield stress normalized by the shear modulus versus volume-per-surface area for nickel, gold, and copper for various experiments and MD simulations.

3.3.2 Dislocation Structures and Interfacial Slip

In this section we examine dislocation structure formation in the MD simulations to gain insight and an understanding of the underlying mechanisms of friction between the particles. The surface phenomena associated with frictional sliding result in high dislocation densities and considerable plastic straining near the contact interface. Plastic deformation involves the generation and propagation of dislocations in the bulk and at the interface. As the actual contact size decreased, surface-to-volume ratio increased (as specimen size decreased) which resulted in large plastic strains and strain gradients near the interface. Several researchers [Hurtado and Kim, 1999a,b; Bhushan and Nosonovsky,

2003] have suggested that dislocation assisted sliding is the main mechanism responsible for the scale dependence of the shear strength at the interface leading to scale dependent friction. The size effects which cause surface phenomena to dominate are not included in conventional friction theories but are clearly revealed in these simulations.

The snapshots from the MD simulations provided in Figures 3.13 – 3.16 clearly show the evolution of dislocation nucleation and glide along crystallographic planes. In the figures the centrosymmetry parameter was used to visualize the dislocations in the model. Kelchner et al. [1998] found that the centrosymmetry parameter could easily distinguish between surface atoms, stacking faults (one or two layer interruptions in the stacking sequence of the two close-packed lattices), and partial dislocations (dislocations which shift planes of atoms past each other only partially) in an MD simulation. Full dislocations shift a plane of atoms past another in a way that preserves crystal symmetry. For nickel, the centrosymmetry parameter is zero for atoms in a perfect lattice. The atoms in Figures 3.13 – 3.16 are colored according to the value of the centrosymmetry parameter, where green is for partial dislocations (4.1-4.7 $Å^2$), yellow is for stacking faults (5.4-5.75 $Å^2$), and red is for surface atoms (>18 $Å^2$). As shown in the figures, by using MD and the centrosymmetry parameter, we were able to observe the nucleation of partial dislocation loops and other complex dislocation structures in the simulation.

Figure 3.13 shows several images of the defective structure in the 3.52 nm particle, 60 degree contact model at different strains in the simulation. As observed in the figure, at the macroyield point, a partial dislocation is emitted at an edge of the contact interface and glides across the contact area causing a decrease in average particle shear stress as it dissolves into the other side of the particle boundary. The dislocation

structures consist of stacking faults surrounded by partial dislocations. Similarly at 8% strain a partial dislocation is observed nucleating from the contact boundary and causes a peak in stress prior to it gliding across the particle. A dislocation is shown to move across the contact region at 13% strain, which is also a peak stress point on the shear-stress strain curve. Thus, in the 3.52 nm particle model, one can easily distinguish nucleation and glide of single dislocations across the contact region, indicating that dislocation assisted sliding contributes to sliding at the interface.

To observe the size effect, we also studied the evolution of the dislocation structures for the 14 nm, 60 degree contact model. As shown in Figure 3.14, the resulting dislocation structure consist of stacking faults surrounded by partial dislocations similar to the structures in the 3.52 nm model. The first microyield occurred at approximately 1% strain, with dislocation activity observed starting at 2% strain. At approximately 3.5% strain a dislocation structure nucleates at the contact region and glides across the contact region causing a drop in stress. At 5.5% strain, a partial dislocation originates in the contact region, bows out from the interface, and joins with another partial dislocation forming in the lower particle. In a similar way, as shown in Figure 3.15, dislocation structures continue to nucleate and glide near the contact region at 5.5%, 8%, 10% and 11.5% strain. From the behavior observed in Figures 3.14 and 3.15 it is apparent that initially dislocation activity is primarily limited to the interface region. With increased size, the dislocation structures become much more complex as indicated in Figure 3.15. With increased strain, as shown in Figure 3.16, the dislocation structures continue to grow until slippage is observed at the contact interface when the shear stress reaches the friction stress. Also, as the particles are continually strained and plastic deformation

increases, the dislocations tend to move more toward the particle centers. The figures also indicate that dislocation formation due to friction occurs at contact boundaries and glide through the particles, as well as across the contact causing plastic deformation. When the shear force approaches the friction stress, sliding occurs along the contact interface. In some instances sliding occurs along a slip plane near the contact region instead of along the contact interface due to the slip plane being a more favorable direction. With increased loading/strain, complex dislocations form within the particles. As the stress of the particles increases, dislocations also start to emit from the particle boundaries, away from the contact region, at approximately 12.5% strain as shown in Figure 3.16. Additionally, one can distinguish dislocation assisted slip at the interface and dislocation glide through the particles. An increase in dislocation activity occurs in the lower particle up to 18% strain, as evident in Figure 3.17.

As shown in Figure 3.18, slippage along the interface was on the order of one Burgers vector, which further indicates the mechanism of interfacial slip is due to dislocation glide even for the nanoscale particle models.

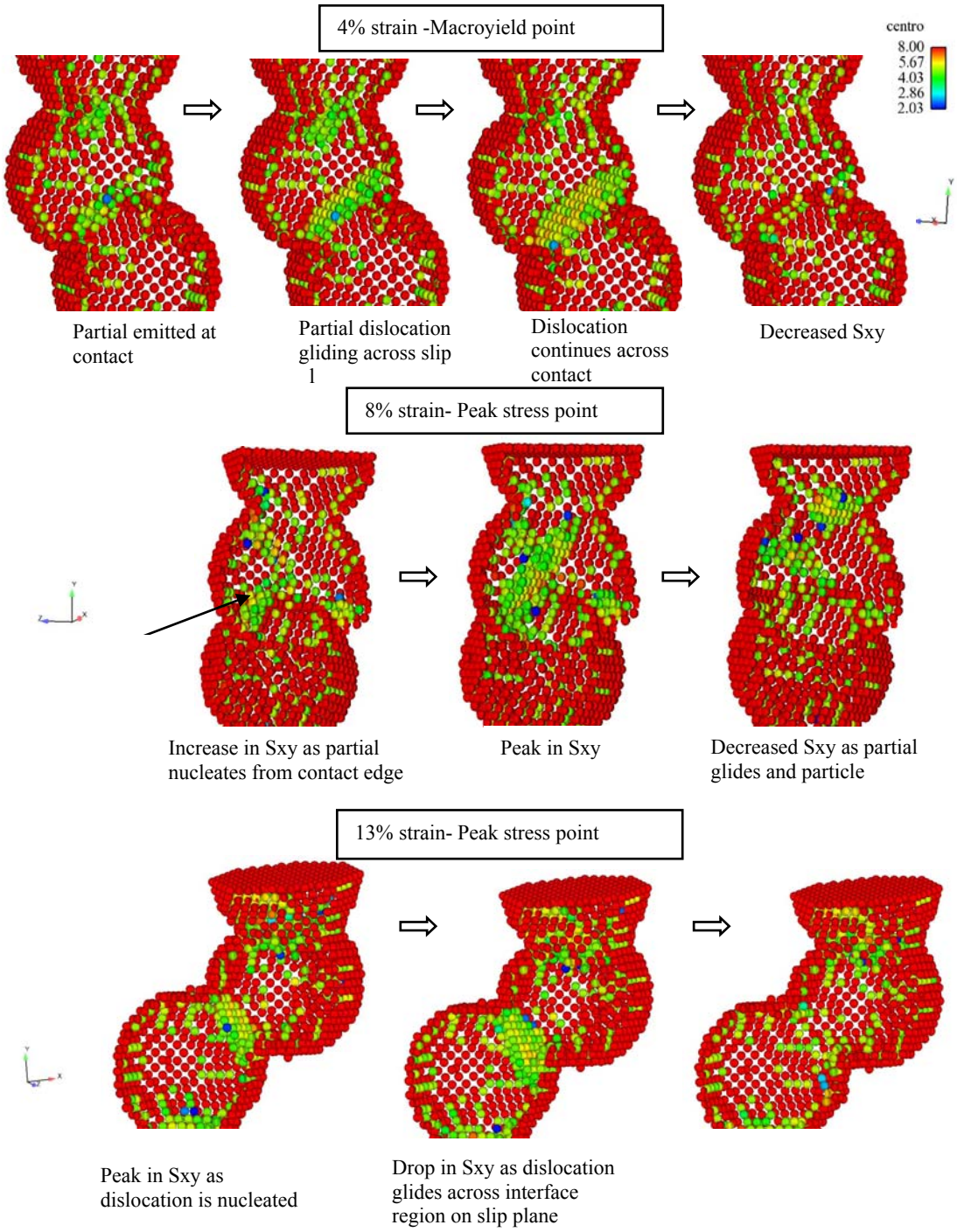

Figure 3.13 Evolution of dislocation structures and plastic deformation from MD Simulations for 3.52 nm particle model with a 60 degree contact angle. Dislocation nucleation and glide along discrete slip planes through the centers and along the interface of two contacting particles is demonstrated along with formation of complex dislocation structures attributing to plastic deformation.

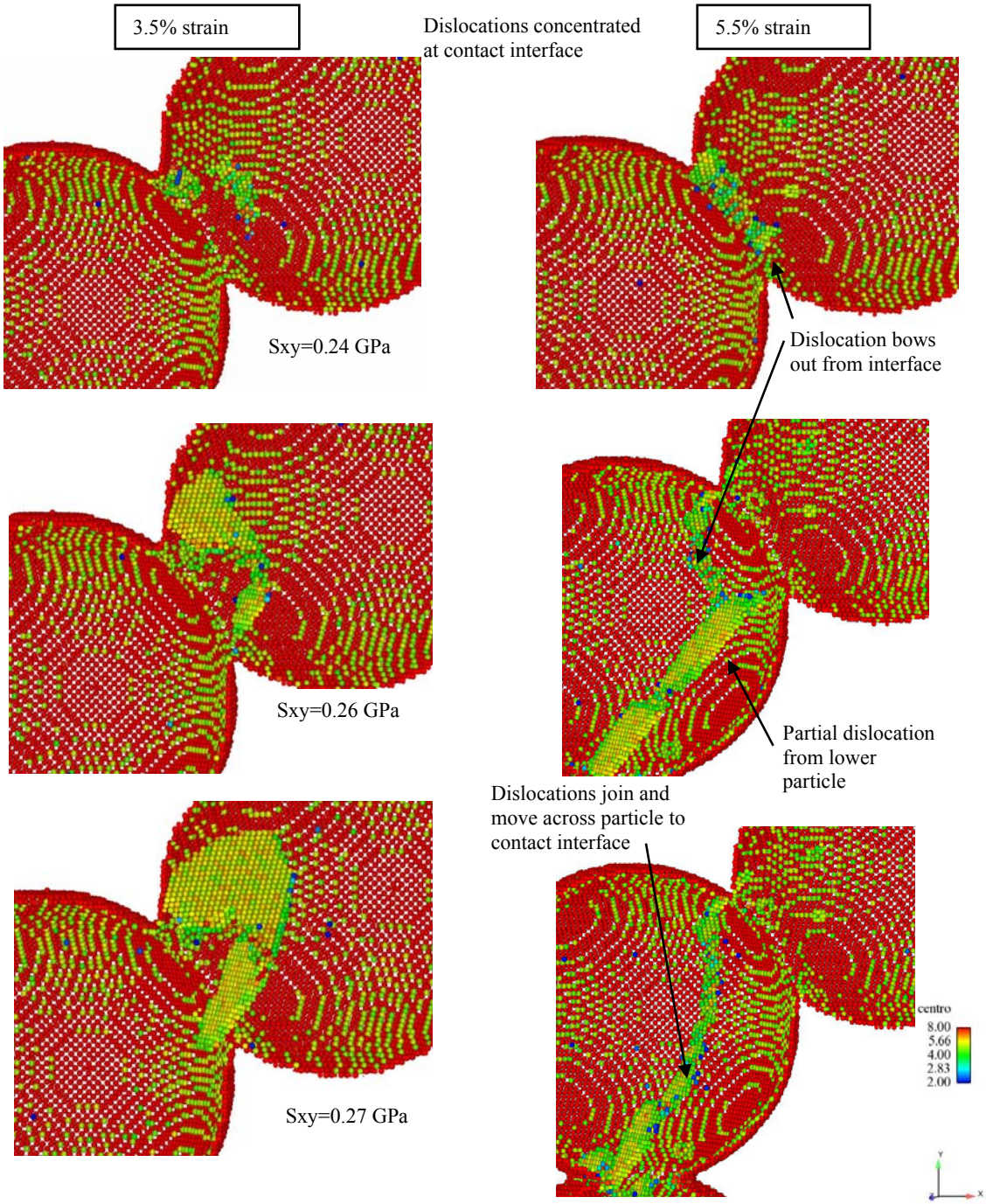

Figure 3.14 Evolution of dislocation structures and plastic deformation between 3-5% strain from MD Simulations for 14 nm particle model with a 60 degree contact angle. Dislocation nucleation and glide along discrete slip planes through the centers and along the interface of two contacting particles is demonstrated along with formation of complex dislocation structures attributing to plastic deformation.

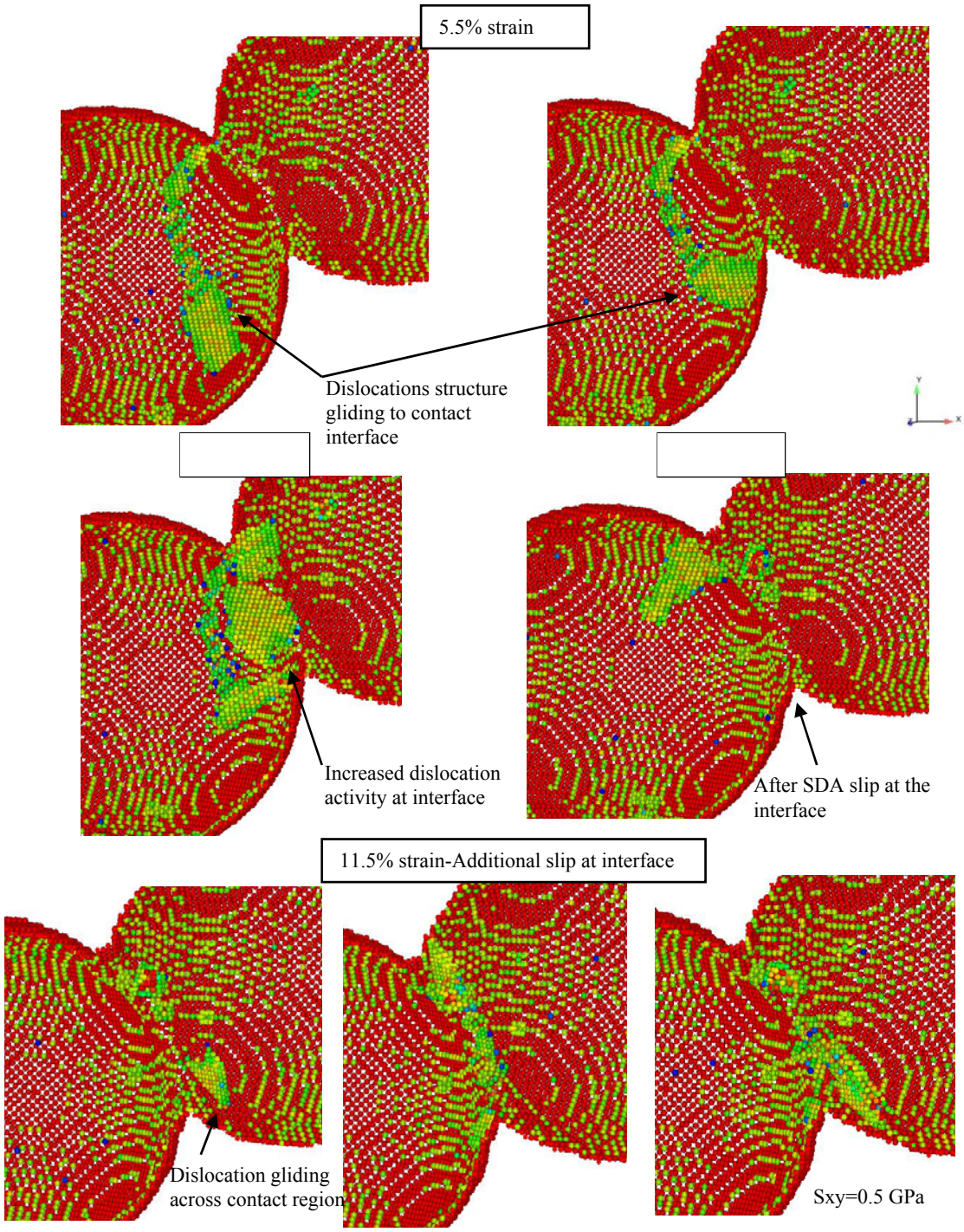

Figure 3.15 Evolution of dislocation structures and plastic deformation between 5-12% strain from MD Simulations for 14 nm particle model with a 60 degree contact angle. Dislocation nucleation and glide along discrete slip planes through the centers and along the interface of two contacting particles is demonstrated along with formation of complex dislocation structures attributing to plastic deformation.

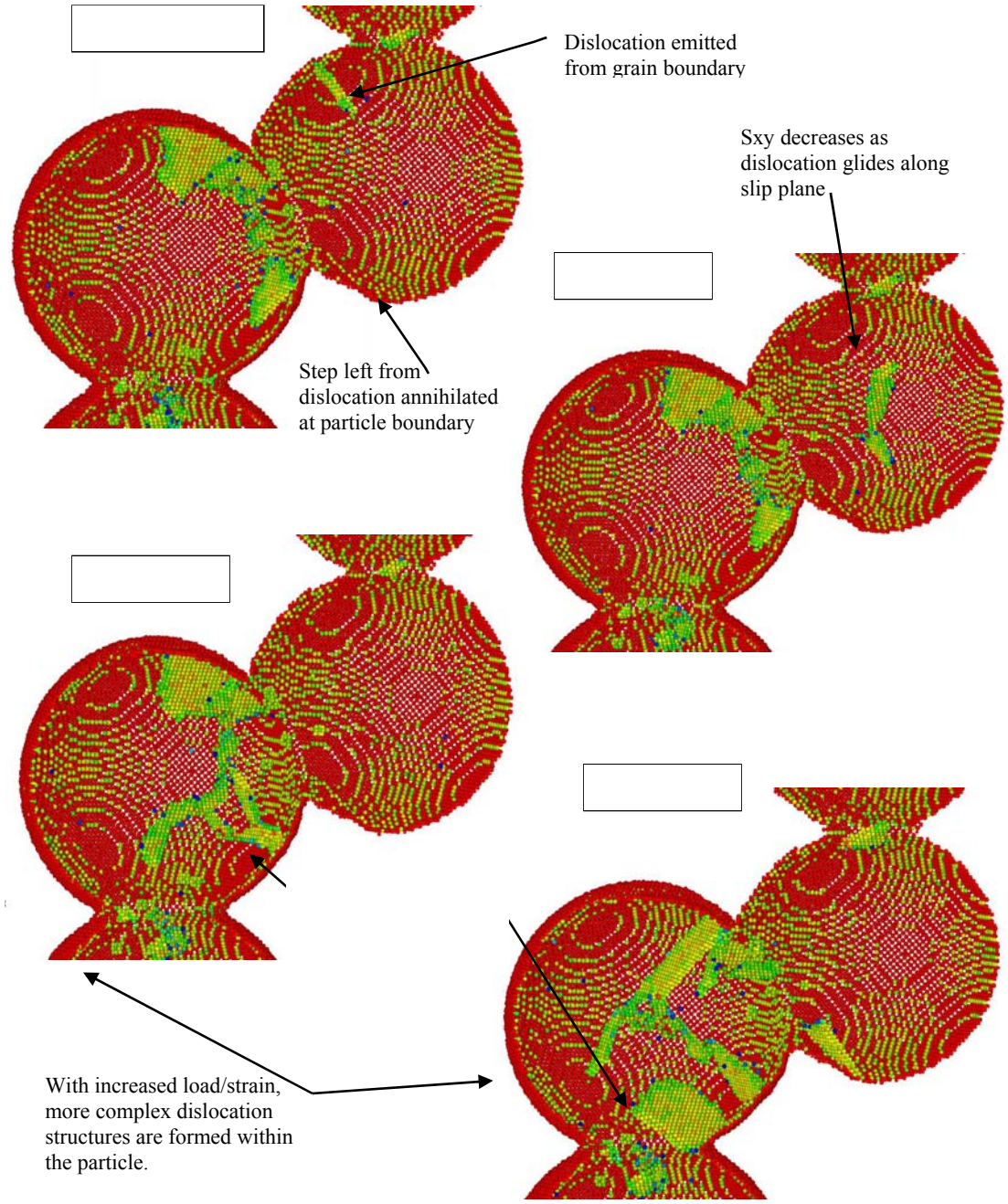

Figure 3.16 Evolution of dislocation structures and plastic deformation between 12-15% strain from MD Simulations for 14 nm particle model with a 60 degree contact angle. Dislocation nucleation and glide along discrete slip planes through the centers and along the interface of two contacting particles is demonstrated along with formation of complex dislocation structures attributing to plastic deformation.

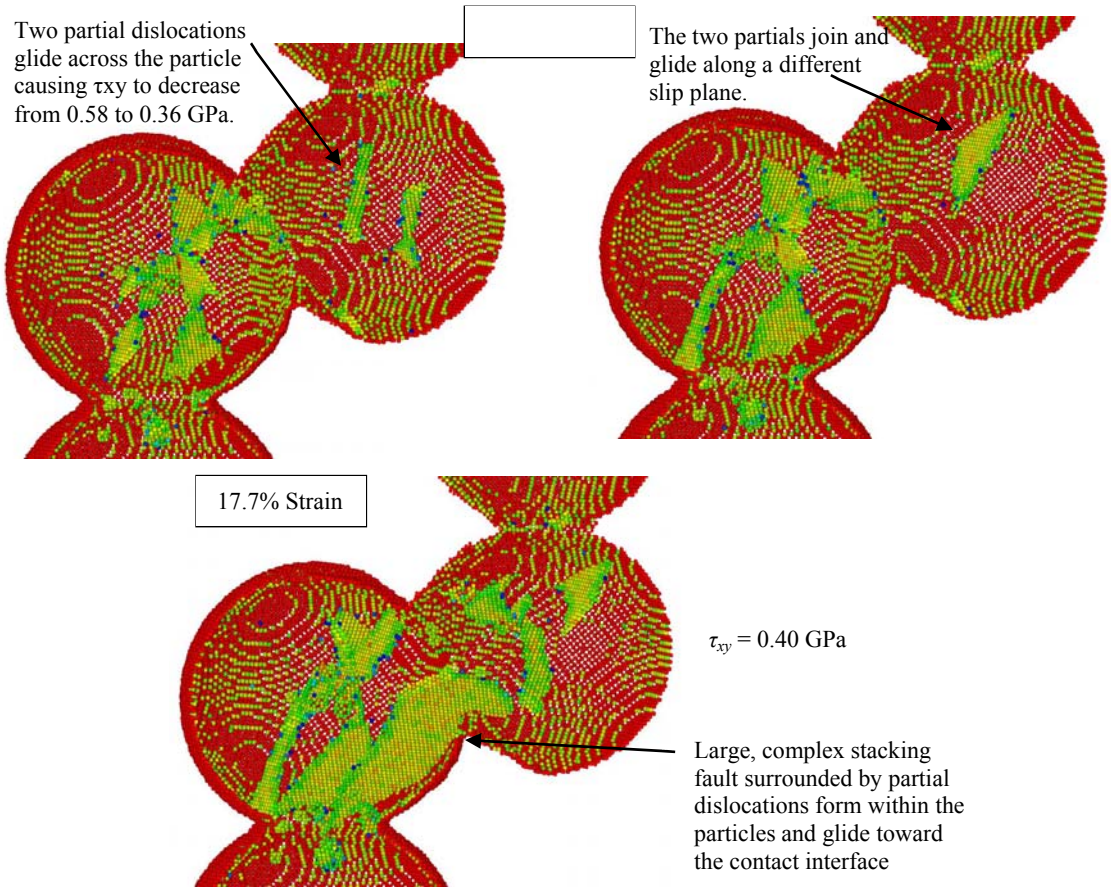

Figure 3.17 Evolution of dislocation structures and plastic deformation between 16-18% strain from MD Simulations for 14 nm particle model with a 60 degree contact angle. An increase in dislocation structures is evident with increased strain.

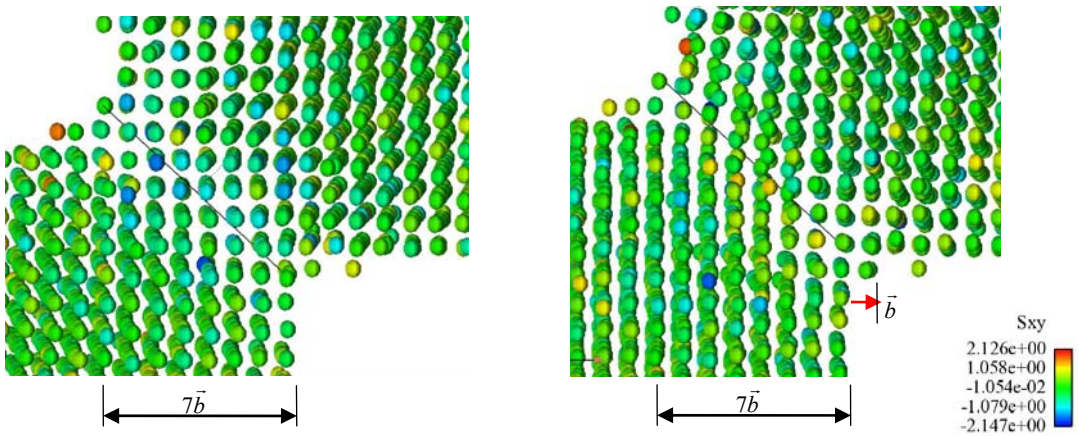

After thermal equilibrium, 0% strain

After 3% strain, τ_s = 1.05 GPa

Figure 3.18 Snapshots from MD simulation for 3.52 nm particles with 60 degree contact angle demonstrating microslip by one Burgers vector along the periphery of the interface.

3.3.3 Constitutive Model for Elastic-Plastic behavior

From a continuum perspective, we studied the contact of two nanoparticles having the same mechanical properties. From the MD simulation results, we compared measurements of the relative tangential and normal displacements of the two spherical particles with measured indentation and contact radius at the interface of the particles. The elastic constants were denoted as E_1, E_2, v_1, and v_2 for Young's modulus and Poissons ratio, respectively for particles *1* and *2*. The materials were considered elasto-plastic with the effects of strain-hardening considered. For two contacting particles with radius r_1 and r_2, the relative radius, r_c, and elastic modulus, E_c, were defined as

$$r_c = \frac{r_1 r_2}{r_1 + r_2}, \tag{3.12}$$

and

$$E_c = \left(\frac{1 - v_1^2}{E_1} + \frac{1 - v_2^2}{E_2} \right)^{-1}. \tag{3.13}$$

The effective shear modulus G_c was evaluated in terms of the effective elastic modulus as

$$G_c = \frac{E_c}{2(1+\nu)}. \tag{3.14}$$

In analyzing the contact forces we considered the tangential tractions between the two particles, as shown in Figure 3.19. The solution for the tangential traction may be expressed in terms of the interface behavior of the material, such as fully sticking (no slip), partial slipping, and gross sliding. Slip is defined as the relative tangential displacement of points on the contact surface with respect to the displacement of the undeformed regions of each particle. If a tangential force causes elastic deformation without slip at the interface, the contact is in a state of sticking and the tangential traction is defined as

$$\tau_t = \frac{4Gu_t}{\pi a(2-\nu)}, \tag{3.15}$$

where u_T is the relative tangential displacement of the particle centers. The elastic tangential displacement is directly proportional to the tangential force because it is independent of contact area. Thus the tangential force may be derived as [Johnson, 1987]

$$F_t = \tau_t(2\pi a^2) = \frac{8Gu_t a}{(2-\nu)}. \tag{3.16}$$

The distribution of tangential traction is radially symmetrical and increases radially, as represented by the following relation, [Johnson, 1987]

$$\tau_t(r) = \frac{F_t}{2\pi a}\left(1-\frac{r^2}{a^2}\right)^{-1/2}. \tag{3.17}$$

As the applied tangential traction increases, microslip is inevitable at the edge (periphery) of the contact which results in a state of partial slipping or stick-slip

condition. As shown in Figure 3.18, small relative motion or slip over part of the interface occurs, while the remainder of the interface deforms without relative motion resulting in adherence or "sticking" in those regions. Therefore, the displacement at the interface may be separated into an elastic or adhering component

$$u_t = u_t^e + u_t^p \tag{3.18}$$

The slip at the contact continues to increase with tangential loading until gross sliding occurs and the whole contact interface is sliding.

A condition of gross sliding occurs when the relative slip at the interface is equivalent to the relative tangential displacement of the particle center. When the contact is sliding, Coulomb law of friction is assumed,

$$\vec{F}_t = -\mu \| F_n \| \vec{t} \ , \tag{3.19}$$

where μ is the friction coefficient, F_n is the normal force at the contact point, F_t is the tangential force is greater than or equal to the friction force F_f at the contact, and $\boldsymbol{t}$ is the unit vector parallel to the contact plane.

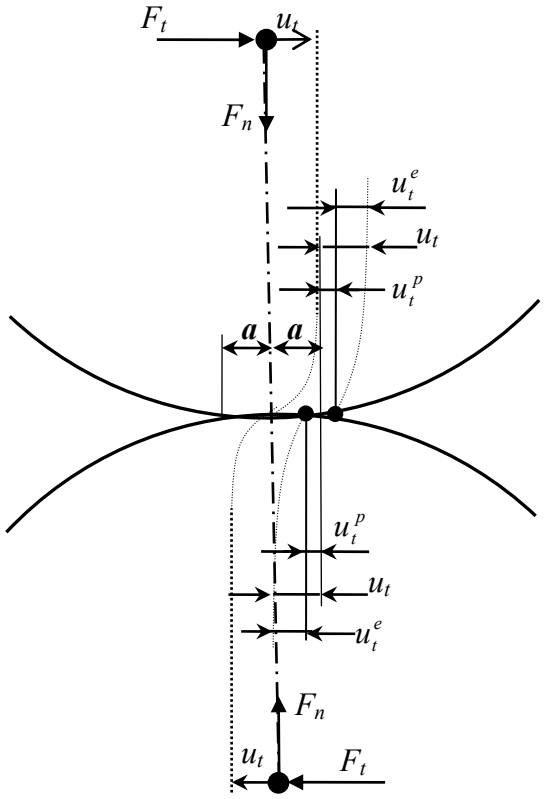

Figure 3.19. Friction force is proportional to the tangential relative motion of the particle u_t with reference to the relative tangential motion at the contact interface.

Examination of the interface region of the MD simulations indicated that the particles were initially in a state of sticking at the interface. However, once the tangential traction was large enough to shear the contacting atoms, which implies equal to or greater than the friction stress ($\tau \geq \tau_f$), microslip occurred and the atoms on the periphery of the contact slipped by one Burgers vector as shown in Figure 3.18. To evaluate the slip behavior in the MD simulation further, we also measured the tangential displacement at the contact and compared it to the actual displacement of the particle centers to determine the friction phenomena. As shown in Figure 3.20, a plot of tangential force versus

tangential displacement also indicates sticking and slipping behavior in the MD simulations.

As described in a previous study [Stone et al., 2008], the following macroscopic plastic contact equation [Storåkers et al., 1997] gave the best correlation for the normal load obtained from measurements of the normal displacement h in the MD models,

$$F_n = 3\pi\sigma_0(2^{n/2})(3^{-n})c(n)^{2+n}(r_c^{1-n/2})(h^{1+n/2}) \tag{3.20}$$

where

$$h = \frac{a^2}{2c(n)^2 r_c} \tag{3.21}$$

and $c(n)^2 = 1.43\exp(-0.97(n))$ [Larsson and Storåkers, 2000] is related to the size of the contact area and ranges from 0.5 for linear elasticity to 1.45 for perfectly plastic behavior. To consider strain-hardening based on a power law form, the following constitutive equation for the contact was applied

$$\sigma = \sigma_0 \varepsilon^n, \tag{3.22}$$

where σ_0 is a material constant, n is the hardening coefficient and σ and ε are the stress and strain in the uniaxial case. For linear elasticity, n = 1 and $\sigma_0 = E$, while for perfect plasticity, n = 1 and $\sigma_0 = \sigma_y$, the yield strength of the material. As shown in Figure 3.21a, Eq. (3.20) results in a nonlinear dependence of the normal load on the contact area. The normal indentation was determined from measurements of the contact radius a throughout the MD simulations based on Eq. (3.20) and captured the size effect in the model as indicated when plotted again the normal load as shown in Figure 3.21b and is largely affected by the contact angle as indicated. The size dependence of the normal load is captured by the indentation Eq. (3.21). Figure 3.22 shows a plot of normal

indentation (displacement) h versus contact radius for the elasto-plastic analysis. The normal displacement or indentation, h, of the two particles is due primarily to deformation in the contact region and as shown in Figure 3.22 was independent of the contact angle. Because friction has been shown by previous researchers [Johnson, 1987] to have little effect, if any, on the normal load, we assumed that the stresses and deformation due to normal pressure and tangential traction are independent of each other.

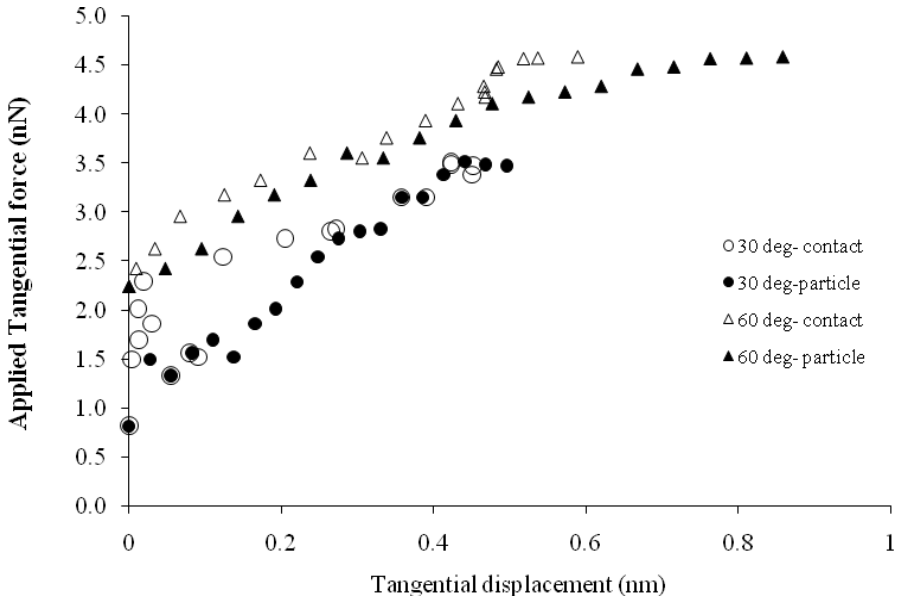

(a)

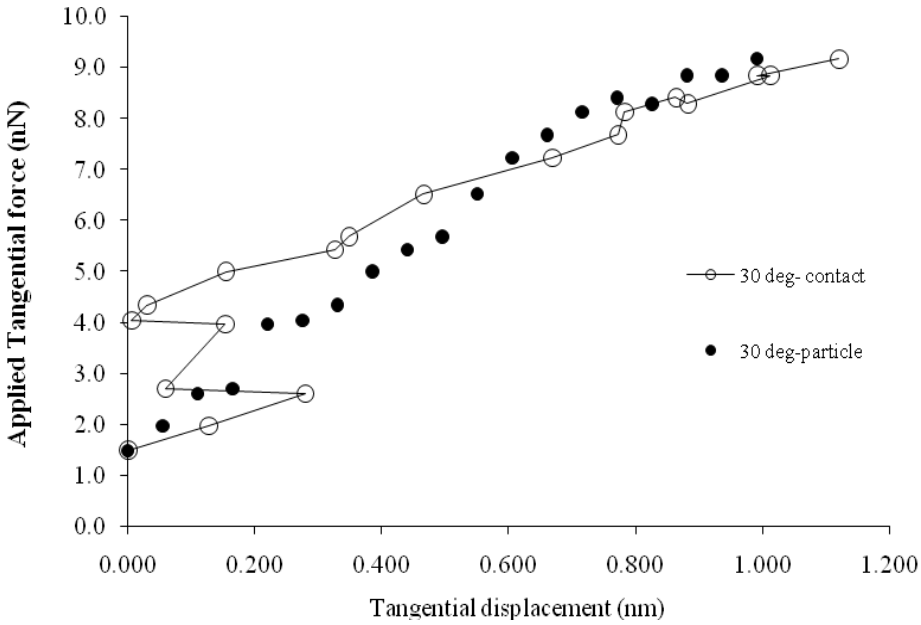

(b)

Figure 3.20 Comparison of tangential force versus tangential displacement of the particle centers and tangential displacement of the contact interface from the MD simulations for (a) 3 nm dia. particle model and for (b) 7nm dia. particle model results.

(a)

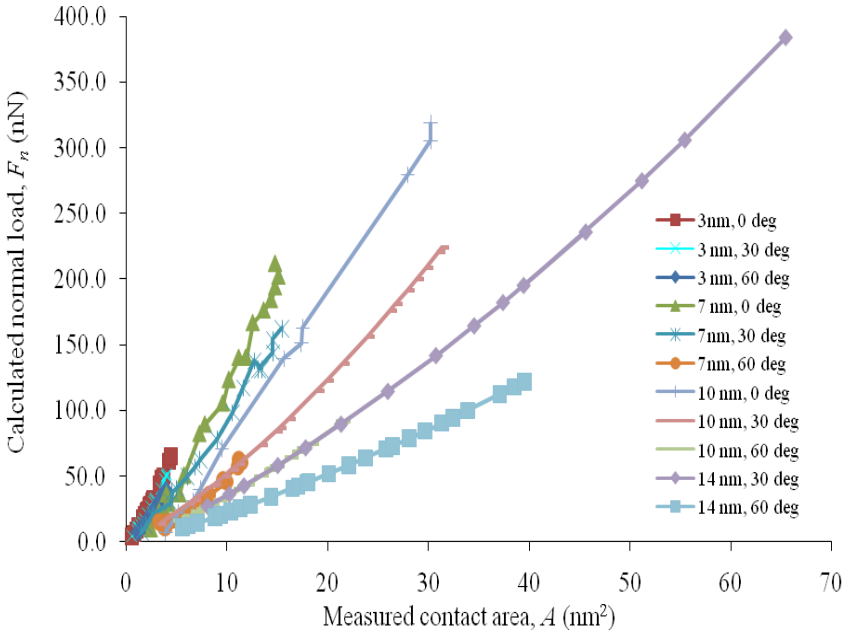

(b)

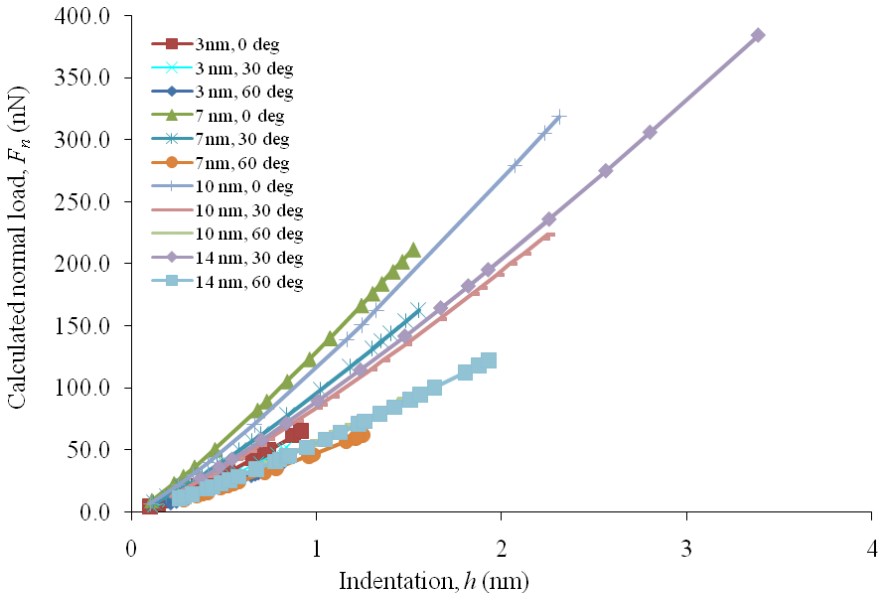

Figure 3.21 Calculated normal load [Storåkers et al., 1997] versus (a) measured contact area and (b) versus normal indentation (MD EAM simulations) for various particle sizes and contact angles.

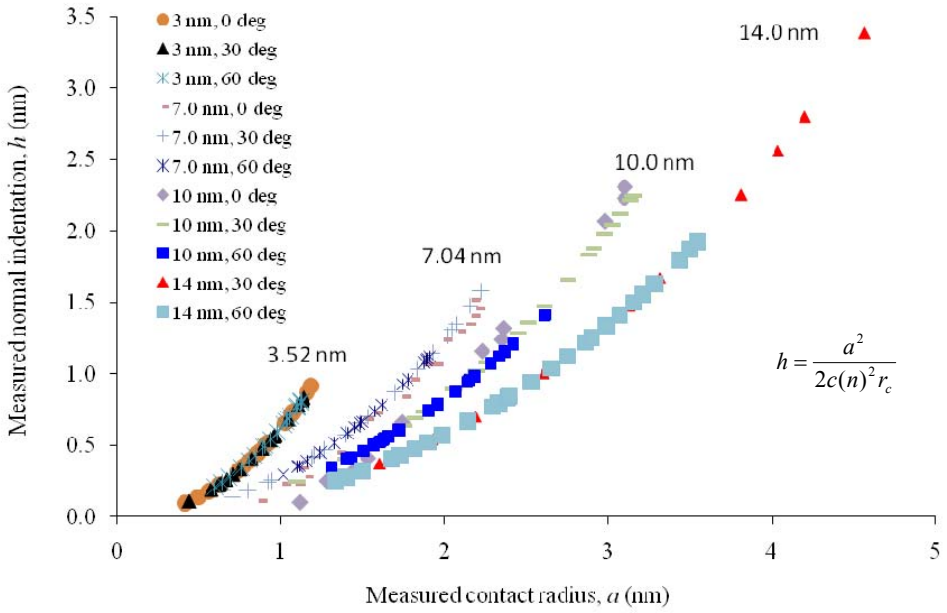

Figure 3.22 Measured normal indentation vs. measured contact radius from MD EAM simulations for various particle sizes and contact angles.

3.4 Scale-Dependent Friction Model

The classical theory of adhesion first postulated by Bowden and Tabor [1950] suggests that the friction force F_f to glide across a single asperity is proportional to the real area of adhesive contact A_r such that

$$F_f = \tau_f A_r, \tag{3.23}$$

where τ_f is the average shear strength during sliding and is independent of contact area. The adhesion theory results in a linear dependence of the friction force on the contact area and an independence of the coefficient of friction on the normal load. However, the wide variation in ratio of friction stress to shear modulus measured experimentally in AFM and SFA indicate that the friction stress is not independent of contact size for all contact sizes [Homola et al, 1990; Carpick et al., 1996]. Although we observed a size dependence in friction stress at the nanoscale, within each model we assume that any

change in friction stress with respect to the dynamic contact area of a given simulation is negligible. Figure 3.23 includes a plot of the friction forces versus contact radius. The results reveal that while particle size has some effect on friction force, the particle contact angle has the largest effect.

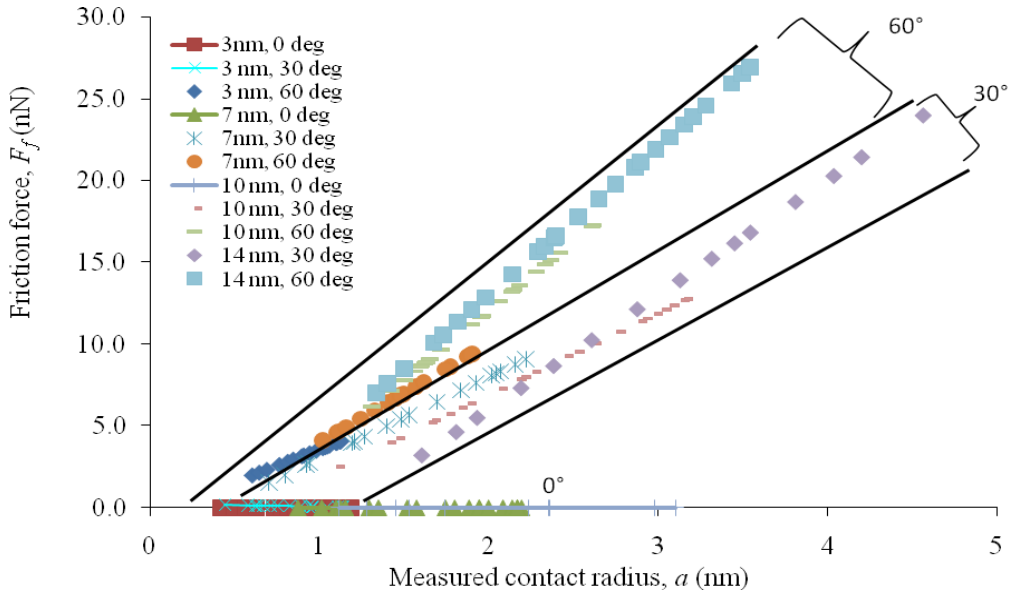

Figure 3.23 Friction force versus measured contact radius for various particle size and contact angles.

Because the coefficient of friction is the proportionality parameter between the tangential and normal loads, we plotted the tangential force versus normal force for both the 30 degree and 60 degree contact angles as shown in Figures 3.24-3.27 to quantify the coefficient of friction with different specimen sizes. The plots include the friction force calculated based on Eq. (3.23) where the friction stress is measured directly from the MD model and from using the approximation based on the maximum global shear stress given by Eq. (3.11). As indicated in the figures, there is a good correlation between the plots from each method, indicating that the global shear stress measurement gives a good

approximation for the friction stress. Figures 3.24-3.27 also indicate that a nonlinear relation exists between the normal and tangential forces that can be described by the following power law relation,

$$F_f = C_0\left(F_{adh} + F_n\right)^n \tag{3.24}$$

where C_0 is a constant and n is a hardening parameter. The fitting parameters for the MD simulations are provided in Table 3.2.

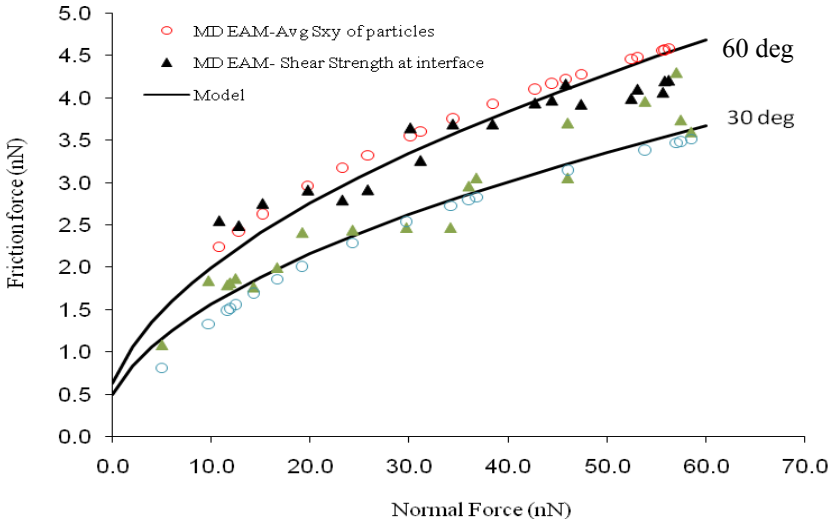

Figure 3.24 EAM MD simulation results for tangential force vs. normal force for a 3.5 nm spherical particles.

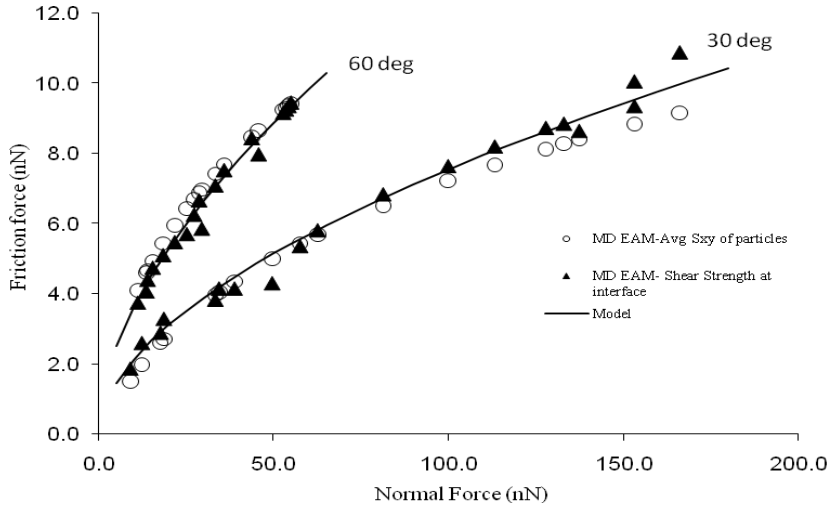

Figure 3.25 EAM MD simulation results for tangential force vs. normal force for a 7.0 nm spherical particles.

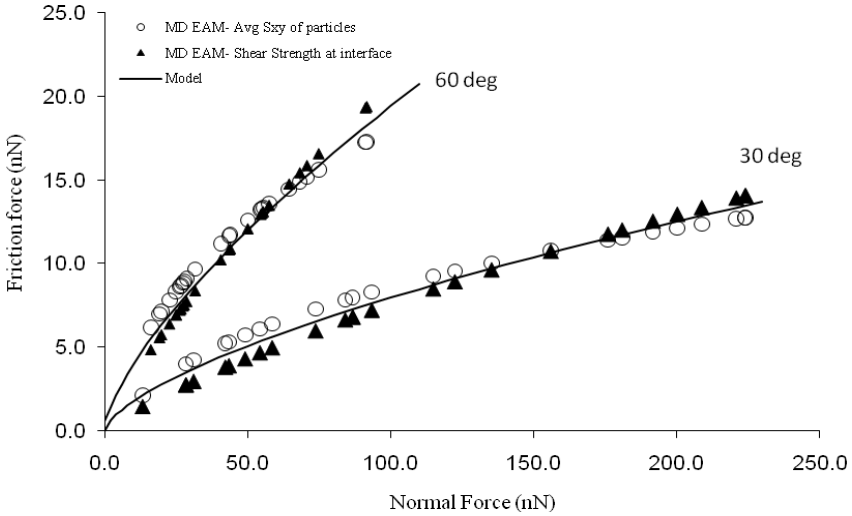

Figure 3.26 EAM MD simulation results for tangential force vs. normal force for a 10.0 nm spherical particles.

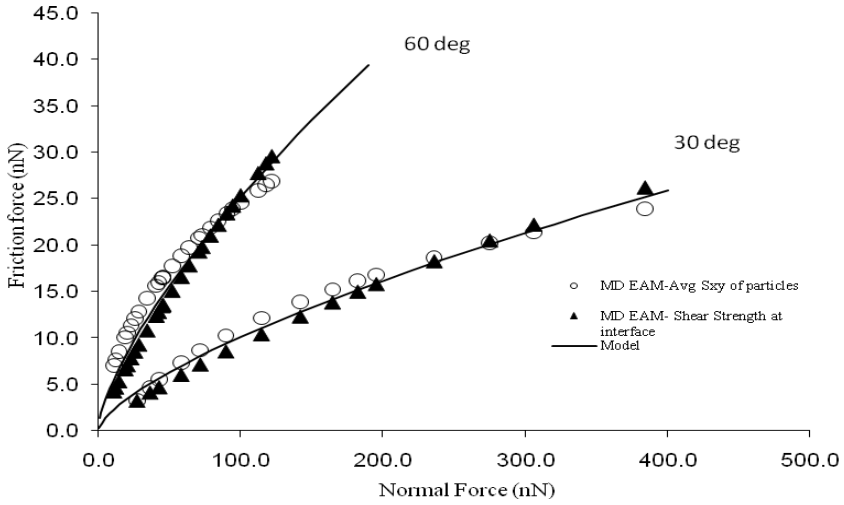

Figure 3.27 EAM MD simulation results for tangential force vs. normal force for a 14.0 nm spherical particles.

Table 3.2 Friction model parameters for the MD simulation results.

Particle size (nm)	Contact angle (deg.)	C_0	n (exponent)	F_{adh} (nN)
3.52	30	0.47	0.5	1.10
3.52	60	0.60	0.5	1.10
7.04	30	0.60	0.55	0
7.04	60	0.95	057	0.5
10.0	30	0.40	0.65	0
10.0	60	0.77	0.7	0.4
14.0	30	0.44	0.68	0.5
14.0	60	1.0	0.7	0.5

The non-linear relationship between the friction force F_f and the normal load F_n is due to the non-linear dependence of the real contact area on the normal F_n and adhesive forces F_{adh}. However, as indicated in Figures 3.24-3.27, the size effect becomes much more significant as the contact angle is increased due to increased adhesion at the interface. A comparison of the friction force versus normal force based on particle size is given in Figure 3.28 for the 30 degree contact model and in Figure 3.29 for the 60 degree contact model.

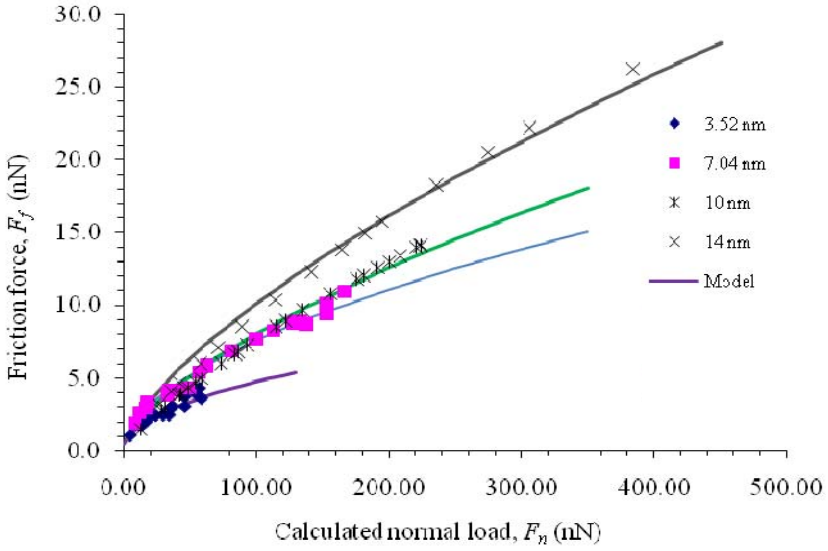

Figure 3.28. EAM MD simulation results for tangential force vs. normal force for a 30 degree contact angle.

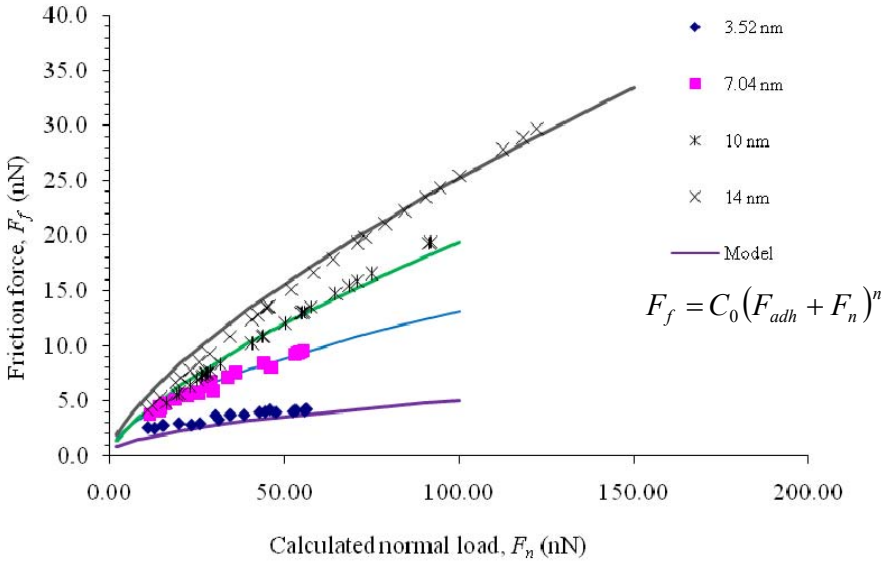

Figure 3.29 EAM MD simulation results for tangential force vs. normal force for a 60 degree contact angle.

For comparison with other research studies, when the contact interface is in a state of slipping, we assumed that the coefficient of friction is defined based on the classical Coulomb friction law,

$$\mu = \frac{F_t}{F_n} \tag{3.25}$$

However, as observed in Figures 3.24 - 3.27, the tangential/normal force ratios from the MD simulations is not constant. Therefore, the coefficient of friction is not constant and was shown to be dependent on contact angle and particle size. To study the evolution of the coefficient of friction, we plot the coefficient of friction as given by Eq. (3.25) versus applied strain. The excellent correlation of the normal indentation to the plastic work hardening model, the contact indicates that the contact deformation is primarily plastic. Therefore we assume that the applied strain is equivalent to the plastic strain in our formulation. As shown in Figure 3.30 for the 30 degree contact model and Figure 3.31 for the 60 degree contact model, the coefficient of friction decreases to a saturation value with increased strain. A listing of the saturation values for each model configuration is given in Table 3.3.

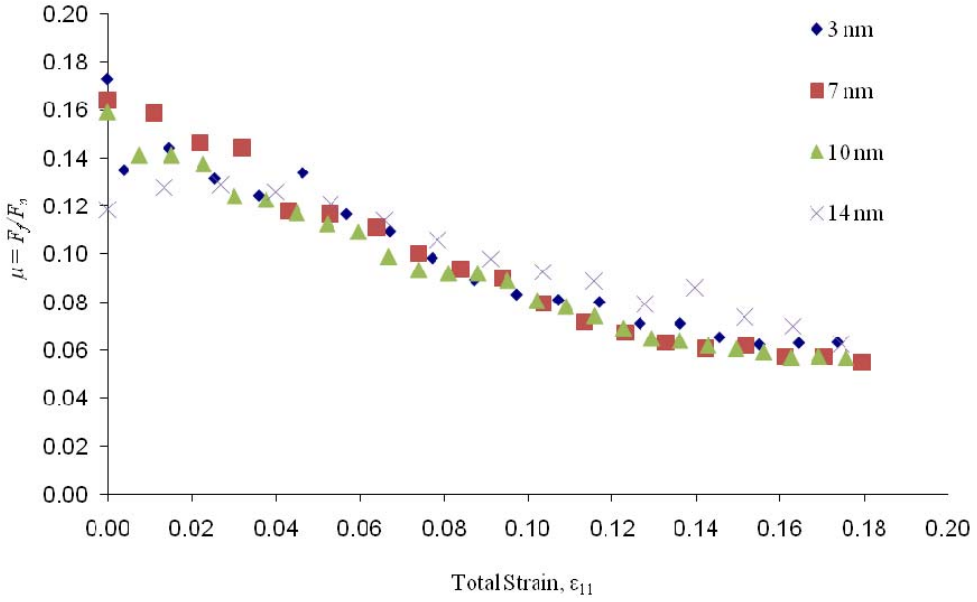

Figure 3.30 MD simulation results for the evolution of the coefficient of friction for a 30 degree contact angle between the spherical particles.

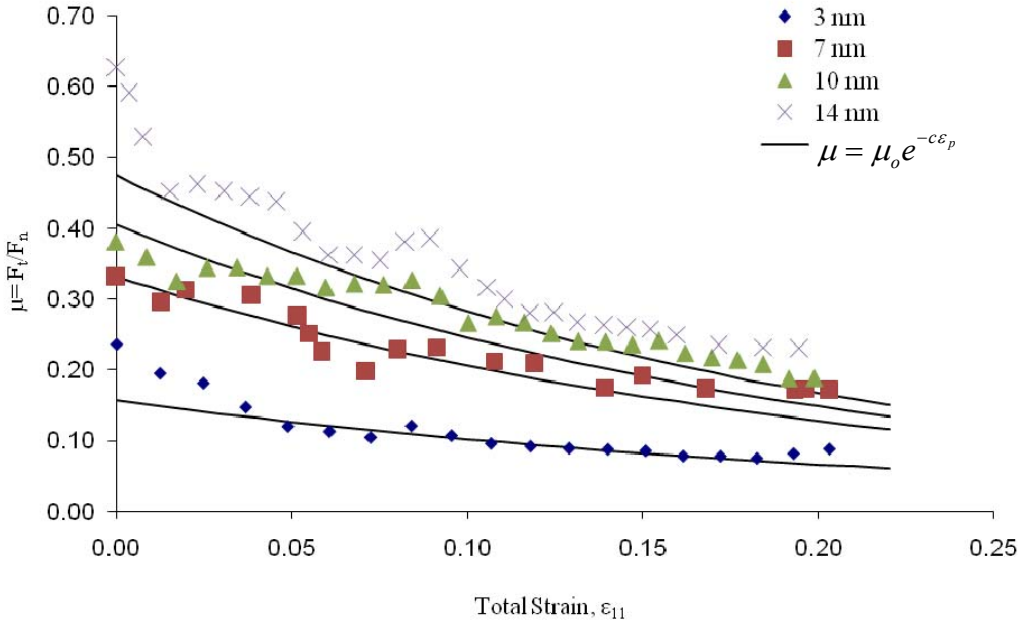

Figure 3.31 Correlated friction evolution equation from MD simulation data for 60 degree contact angle between the spherical particles.

Table 3.3 Coefficient of friction saturation values from the MD simulations.

Particle size (nm)	Contact Angle (degrees)	μ_0	μ_{sat}	Contact Angle (degrees)	μ_0	μ_{sat}
14	60	0.63	0.23	30	0.14	0.06
10	60	0.38	0.21	30	0.15	0.06
7.04	60	0.33	0.16	30	0.16	0.05
3.52	60	0.24	0.06	30	0.17	0.06

The evolution of the coefficient of friction with applied strain is represented by the following relation for the coefficient of friction in terms of the length scale parameter, V/A_s in meters,

$$\mu = \mu_o e^{-c\varepsilon_p} \tag{3.26}$$

where,

$$\mu_o = 0.208 \ln \frac{V}{A_s} + 4.3235 \tag{3.27}$$

and

$$c = 0.6088 \ln \frac{V}{A_s} + 16.473 \tag{3.28}$$

are material parameters that account for the length scale effects. The friction formulation in Eq.(3.26) is consistent with work by previous researchers who have shown a relation between the coefficient of friction and plastic strain or displacement at the interface [Fredriksson, 1976]. Coefficient of friction increased as the contact angle increased between the nanoparticles. To show its capability, the friction model results for nanosized particles through particles 100 μm in diameter are included in Figure 3.32.

The friction evolution in Eq.(3.26) is determined from integrating the following rate form of the coefficient of friction as

$$\dot{\mu} = -c\mu\left\|\underline{D}_p\right\|. \tag{3.29}$$

In this way, the friction model can be integrated into an ISV formulation for including length scale frictional effects based on adhesive forces and deformation at the interface information obtained from the MD simulations.

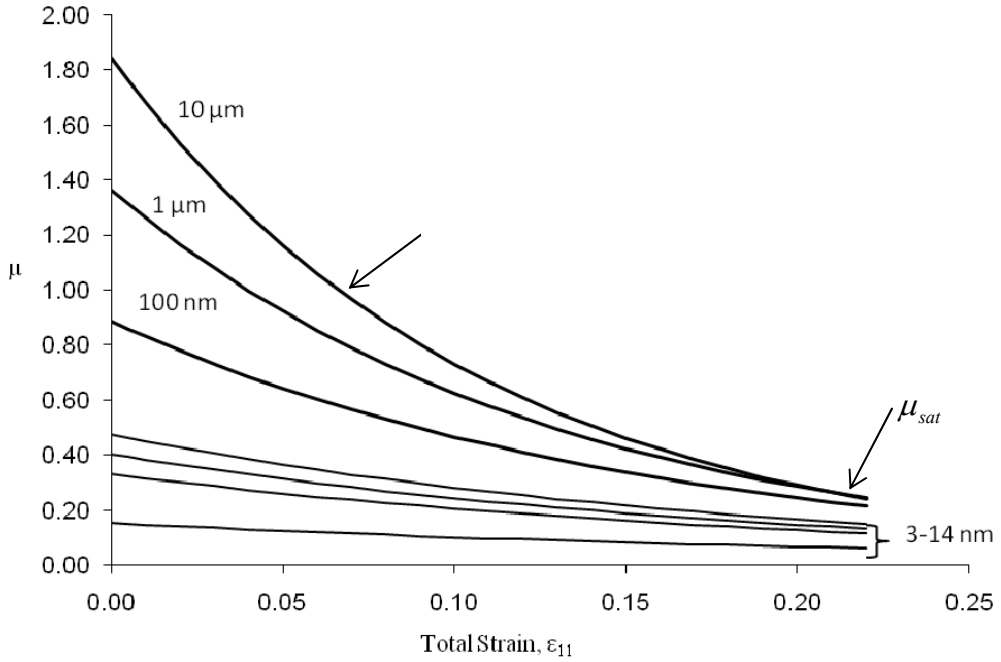

Figure 3.32 Friction evolution model for 60 degree contact angle between two spherical particles applied to particles in the micrometer range.

3.5 MD Results Comparison with Experimental Data

To validate the friction model results, we compared the saturated coefficient of friction values from the MD simulation to experimental data by others [Hanlon et al., 2005, Mishra et al., 2004, Surender et al., 2004]. Figure 3.33 shows a plot of the coefficient of friction versus grain size for the MD simulation results compared to experimental data with grain sizes of 8, 22 and 61 μm. The MD friction measurements compared favorably with the previous experimental studies. A comparison of the MD

simulation and friction model results to experimental saturated coefficient of friction data in the micrometer and millimeter range is shown in Figure 3.34 and shows a very good correlation between the model and the simulation and experimental data.

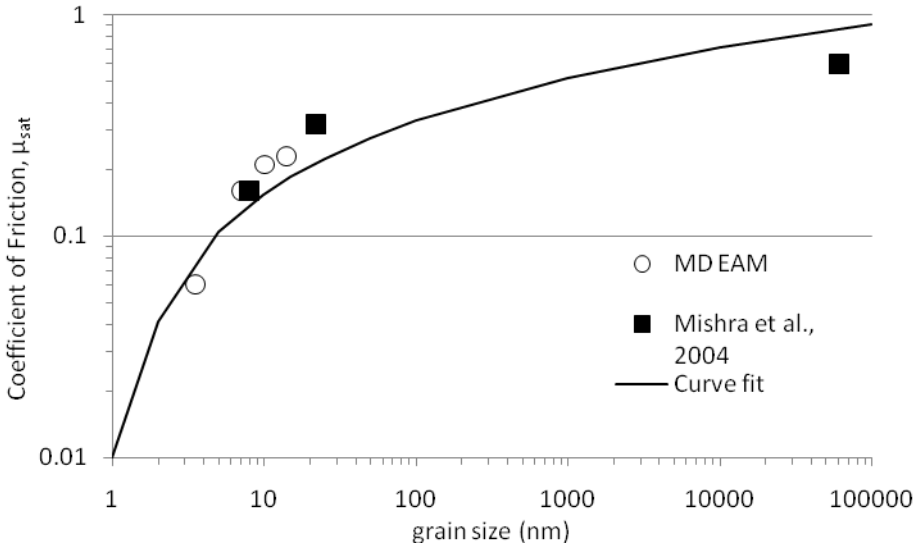

Figure 3.33 Comparison of saturated coefficient of friction between the MD simulation and the experimental results for Ni grain sizes of 8, 22 and 61 μm.

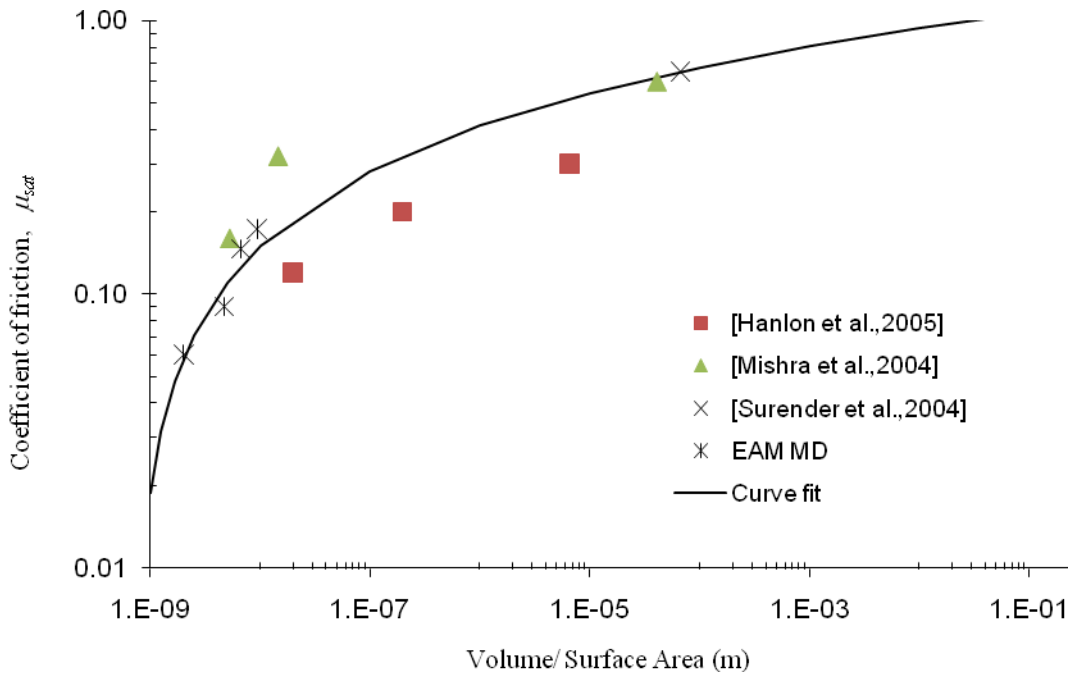

Figure 3.34 Comparison of saturated coefficient of friction values between the model prediction and experimental and MD simulation results based on volume per surface area.

3.6 Summary of Chapter 3

In this study we examined the interparticle contact behavior of two nickel nanoparticles of various diameters and contact angles using MD simulations with EAM potentials to describe the atomic interactions. Specifically we calculated the normal load at the contact by applying measurements from the MD simulation to macroscale plasticity with a work hardening formulation. By comparing measurements of the relative tangential and normal displacements of the two spherical particles with measured indentation and contact radii at the interface of the particles and by examining the interface region, we determined the initial state of the interface to be sticking with microslip occurring after the tangential traction was large enough to shear the atoms at contact. Using the measured shear strength at the interface, the friction force was

evaluated based on the adhesion law for friction. The coefficient of friction was determined from the classical friction law based on the ratio of the friction force to normal force. The coefficient of friction was evaluated and quantified based on a proposed evolution equation which takes particle size and contact angle into account. A continuum internal state variable friction rate equation was formulated from the atomistic simulations and multiscale experimental data for nickel. The internal state variable friction equation is a function of the volume-per-surface-area parameter and can adequately represent all length scales of importance from the nanoscale to the microscale.

CHAPTER IV

HIERARCHICAL MULTISCALE FRICTION MODEL USING MOLECULAR DYNAMICS SIMULATIONS AND INTERNAL STATE VARIABLE PLASTICITY THEORY

4.1 Introduction

Accurate modeling and simulation of interfacial friction and the effect of friction on surface properties is an important area of research, because friction plays an important role in nearly all contact behavior between surfaces. Most model developments are based on describing the behavior of the friction stress during loading of the two contacting bodies. Because the contact behavior between surfaces is a key contributor to the friction, friction modeling must also include some aspect of contact modeling in its derivation. From the definition of the elastoplastic contact laws, the forces between the surfaces are determined. Differences in the coefficient of friction between the nanoscale and macroscale have been observed experimentally [Suh and Sin, 1981; Bhushan and Nosonovsky, 2003]. Because of the scale dependence of the friction stress observed experimentally, a multiscale approach in developing the friction model is desired so as to capture the length scale effect of friction and to include the small scale phenomenon that results from friction and affects the microstructure at the macroscale.

Previous friction models have been developed based on Molecular Dynamics (MD) simulations, discrete dislocation dynamics, and finite element simulations. These computer simulation methods have been pursued to complement experimental studies of friction. Previous macroscale constitutive friction model formulations are typically phenomenological based on empirical relationships for the stress and strain behavior at the interface without any physical interpretation. The drawback with the empirical (analytical) friction models is that their usage is typically limited to the range of conditions for which they were curve-fitted and does not capture the length scale effects of friction. Early developments of friction constitutive laws have been done by several researchers [Cheng et al., 1985; Anand, 1993; Seguchi et al., 1974; Fredriksson, 1976; Michalowski and Mroz, 1978]. Raous et al. [1999] presented a constitutive friction model that coupled adhesion friction and unilateral contact. Scale dependent models are typically physics-based and use dislocation-based formulations to capture the lower length scale phenomena that contribute to the differences in friction stress measured experimentally. The scale dependence of the friction stress for single asperity contacts using a discrete dislocation model was also investigated by Hurtado and Kim (HK) [1999a,b]. Adams et al. [2003] later incorporated the HK model into a multi-asperity, multiscale model for contact and friction. Dominik and Tielens [1996] studied a theoretical model for sliding friction between two micron-sized elastic spheres. Using discrete dislocation dynamics, Deshpande et al. [2004] analyzed the initiation of sliding in single crystals and found that the shear stress is a function of contact size. However, Bhushan and Nosonovsky [2003] used a different approach and developed a model based

on the scale-dependent distribution of surface heights combined with scale-dependent shear strength due to dislocation nucleation from Frank-Read sources.

In the current study, MD simulations were used to describe the friction stresses at the interface based on the underlying microstructural state and dislocation mechanics and used to capture the influence of deformation behavior on friction. Molecular Dynamics simulations with EAM potentials were performed to study the microstructural effects of friction between two contacting surfaces. In Chapter 3, evolutions of the dislocation structures were compared for different sized particles to quantify the length scale effects of friction and the relationship between friction and the dislocation structure. ISVs relate to the changes in the internal structure of a material and are useful to model collective effects of changes in the material structure involving multiple mechanisms at multiple length scales. From the nanoscale studies a multiscale friction model based on internal state variable theory was developed. The constitutive model was coupled with the Bammann-Chiesa-Johnson (BCJ) rate-dependent plasticity model to capture the deformation behavior due to dislocations at the interface.

For simplicity, the current model formulation is developed for the frictional behavior of dry, unlubricated contact surfaces. The proposed model is rate-independent and isothermal while accounting for frictional effects and plastic deformation at the interface. From the interface constitutive laws we formulate an interface friction model that considers the effect of adhesion and stick-slip during contact between the particles. The model is based on classical kinematic assumptions using the multiplicative decomposition of the total deformation gradient into elastic and plastic components and is modified to include friction components. In the formulation the internal state variables

(ISVs) are derived from thermodynamical principles and plastic deformation due to dislocations is related to hardening ISVs.

4.2 Kinematics

Kinematics describe the motion of a body without considering the masses or forces that bring about the motion. To describe the motion two frames of reference are used: the material (or Lagrangian) frame, in which X represents a point on the body in its reference configuration and the spatial (or Eulerian) frame, in which x represents a point on the body in its current configuration/ physical position. Thus, the current configuration is a function of the reference configuration and time,

$$\underline{x} = \chi(\underline{X}, t) \,. \tag{4.1}$$

The deformation of a small volume of the material is represented by the deformation gradient, $\underline{F}$, and from which the spatial frame can be written in terms of the material frame as

$$dx = \underline{F} dX \,. \tag{4.2}$$

All equations are written in the current configuration. The tensors are denoted with underlines and vectors with over bars. Finite plasticity is based on earlier formulations by Kröner [1960] and Lee [1969] in which the deformation gradient $\underline{F}$ can be multiplicatively decomposed into elastic $\underline{F}_e$ and plastic parts $\underline{F}_p$

$$\underline{F} = \underline{F}_e \underline{F}_p \,, \tag{4.3}$$

where the elastic deformation gradient $\underline{F}_e$ represents the elastic stretching and rotating of the crystal lattice in the deformed (or current) configuration. The inelastic deformation gradient $\underline{F}_p$ represents local deformation associated with the dislocation motion which

leads to an intermediate (or relaxed) configuration. To further define the plastic deformation, we separated it into volumetric, $\underline{F}_p^v$ and deviatoric components $\underline{F}_p^{dev}$ that include the plastic deformations due to frictional contacts, $\underline{F}_p^f$ as well as the plastic deformations due to dislocations $\underline{F}_p^d$. Therefore, the deformation gradient for the proposed model is now defined as

$$\underline{F} = \underline{F}_e \underline{F}_p^f \underline{F}_p^d \underline{F}_p^v \ . \tag{4.4}$$

The decomposition of the deformation gradient as represented by Eq. (4.4) results in the deformation process shown in Figure 4.1.

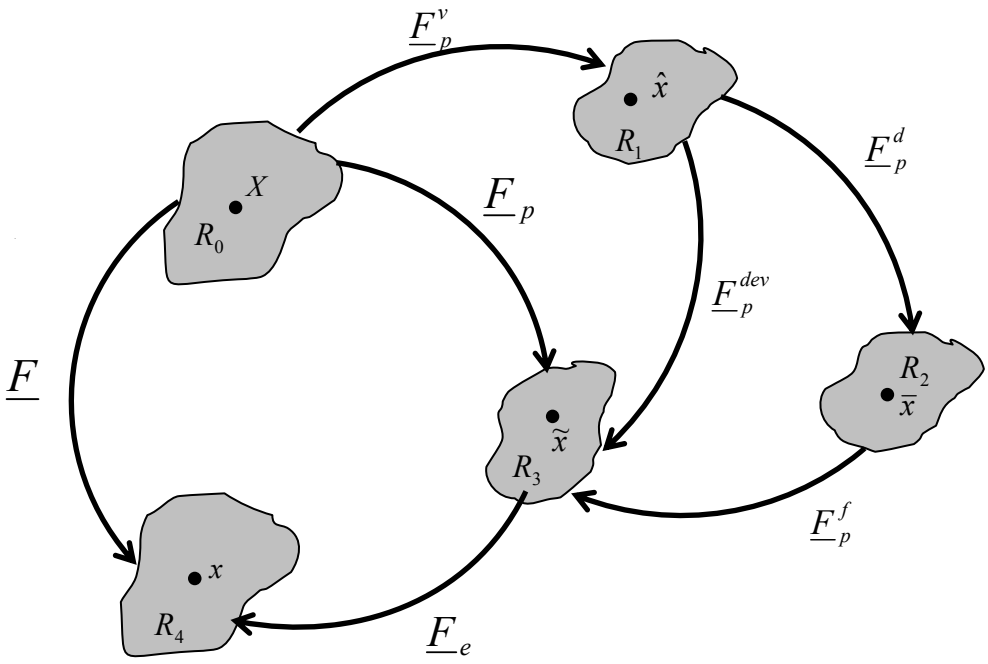

Figure 4.1. Multiplicative decomposition of the deformation gradient.

Using the deformation gradient, we may express the velocity gradient in the current configuration as

$$\underline{\ell} = \dot{\underline{F}}\underline{F}^{-1} = \underline{\ell}_e + \underline{\ell}_p^f + \underline{\ell}_p^d + \underline{\ell}_p^v . \tag{4.5}$$

While the elastic part is naturally defined in the current configuration, the other parts of the velocity gradients are naturally defined with respect to intermediate configurations that can be mapped to the current configuration. Velocity gradients in their natural configurations will be denoted by $\underline{L}$. Thus, the current configuration of the elastic, plastic, and thermal velocity gradients are expressed in terms of their natural configurations are

$$\underline{\ell}_e = \dot{\underline{F}}_e \underline{F}_e^{-1}, \tag{4.6}$$

$$\underline{\ell}_p^f = \underline{F}_e \dot{\underline{F}}_p^f \underline{F}_p^{f^{-1}} \underline{F}_e^{-1} = \underline{F}_e \tilde{\underline{L}}_p^f \underline{F}_e^{-1}, \tag{4.7}$$

$$\underline{\ell}_p^d = \underline{F}_e \underline{F}_p^f \dot{\underline{F}}_p^d \underline{F}_p^{d^{-1}} \underline{F}_p^{f^{-1}} \underline{F}_e^{-1} = \underline{F}_e \underline{F}_p^f \bar{\underline{L}}_p^d \underline{F}_p^{f^{-1}} \underline{F}_e^{-1}, \tag{4.8}$$

$$\underline{\ell}_p^v = \underline{F}_e \underline{F}_p^f \underline{F}_p^d \dot{\underline{F}}_p^v \underline{F}_p^{v^{-1}} \underline{F}_p^{d^{-1}} \underline{F}_p^{f^{-1}} \underline{F}_e^{-1} = \underline{F}_e \underline{F}_p^f \underline{F}_p^d \hat{\underline{L}}_p^v \underline{F}_p^{d^{-1}} \underline{F}_p^{f^{-1}} \underline{F}_e^{-1} \tag{4.9}$$

In order to apply our previous formulation for the velocity gradient, we next derived expressions for the deformation gradients based on physical interpretation of the material behavior with respect to each configuration.

The inelastic volumetric deformation gradient $\underline{F}_p^v$ represents the volume change due to a decrease in voids (or pores) that arises from inelastic deformation during particle consolidation and maps the reference configuration R_0 to the intermediate configuration R_1 as shown in Figure 4.1. The derivation of $\underline{F}_p^v$ is based on the formulation by Horstemeyer et al. [2000]. While in the original formulation the void volume change represents damage, in a porous model, the void volume fraction is associated with densification. To represent the volume change or density change for constant mass

between R_0 and R_1, we consider the Jacobian of the deformation gradient, J, which can also be expressed as the determinant of the volumetric deformation gradient

$$J = \det\left(\underline{F}_p^v\right) = \frac{\hat{v}}{V_0} = \frac{\rho_0}{\rho_1}. \tag{4.10}$$

where $\hat{v}$ the total volume in the intermediate configuration, V_0 is the total volume in the reference configuration, ρ_0 is the reference density, and ρ_1 is the intermediate density. The volume in the intermediate state is equal to the volume in the current state due to inelastic incompressibility defined in the mapping. The total volume in the current configuration is the sum of the volume in the reference configuration and the volume change from the reference to the intermediate configuration (void volume),

$$\hat{v} = V_0 + V_v. \tag{4.11}$$

Therefore the porosity, φ, can naturally be defined as the ratio of void volume (change in volume from the reference to intermediate state) to the total volume in the intermediate state

$$\phi = \frac{V_v}{V_0 + V_v}. \tag{4.12}$$

From a mechanics perspective, the porosity is sometimes expressed in terms of the fractional density ρ which gives

$$\rho = 1 - \phi. \tag{4.13}$$

By combining the equations above, it follows that the Jacobian may be expressed in terms of the porosity parameter as

$$J = \det\left(\underline{F}_p^v\right) = \frac{1}{1-\phi}. \tag{4.14}$$

Assuming that the change in porosity causes only an isotropic volumetric change in the material allows the volumetric deformation gradient to be written as

$$\underline{F}_p^v = \frac{1}{(1-\phi)^{1/3}} \underline{I} \,. \tag{4.15}$$

Thus, from Eq. (4.15) the volumetric velocity gradient becomes

$$\hat{\underline{L}}_p^v = \dot{\underline{F}}_p^v \underline{F}_p^{v^{-1}} = \frac{\dot{\phi}}{3(1-\phi)} \underline{I} \,. \tag{4.16}$$

Additionally, the velocity gradient can be additively decomposed into symmetric, $\underline{d}$, and antisymmetric parts, $\underline{w}$, in the current configuration as

$$\underline{\ell} = \underline{d} + \underline{w} \,, \tag{4.17}$$

where $\underline{d}$ is the rate of deformation and $\underline{w}$, is plastic spin. The velocity gradient is defined in the intermediate configurations as

$$\tilde{\underline{L}}_p^f = \tilde{\underline{D}}_p^f + \tilde{\underline{W}}_p^f \,, \; \overline{\underline{L}}_p^d = \overline{\underline{D}}_p^d + \overline{\underline{W}}_p^d \text{ and } \hat{\underline{L}}_p^v = \hat{\underline{D}}_p^v + \hat{\underline{W}}_p^v \,. \tag{4.18}$$

Therefore, by assuming $\hat{\underline{W}}_p^v = 0$ we obtained the volumetric rate of deformation in the intermediate configurations as

$$\hat{\underline{D}}_p^v = \hat{\underline{L}}_p^v = \frac{\dot{\phi}}{3(1-\phi)} \underline{I} \,. \tag{4.19}$$

In the current model formulation we also assumed that $\underline{W}_p^f = 0$ and $\underline{W}_p^d = 0$ and will include the antisymmetric effects for these configuration in future model developments. Therefore the plastic rate of deformation due to frictional contacts and sliding at the interface may be expressed as

$$\tilde{\underline{D}}_p^f = \tilde{\underline{L}}_p^f \,. \tag{4.20}$$

And similarly, the plastic rate of deformation due to dislocations is defined as

$$\underline{\overline{D}}_p^d = \underline{\overline{L}}_p^d \ . \tag{4.21}$$

The formulation for the plastic rates of deformation will follow in the section on plasticity. Thus, the total rate of deformation in the current configuration becomes

$$\underline{d} = \underline{l} = \underline{l}_e + \underline{l}_p^d + \underline{l}_p^f + \underline{l}_p^v . \tag{4.22}$$

Thus, we can determine the elastic rate of deformation by subtracting the inelastic rates from the total rate of deformation which becomes the following in the current configuration

$$\underline{d}_e = d - d_p^d - \underline{d}_p^f - \underline{d}_p^v \tag{4.23}$$

Therefore, the elastic part of the constitutive law is written in rate form as

$$\dot{\underline{\sigma}} = \underline{\underline{C}}_e : \underline{d}_e = \underline{\underline{C}}_e : \left(\underline{d} - \underline{d}_p^d - \underline{d}_p^f - \frac{\dot{\phi}}{3(1-\phi)} \underline{I} \right) \tag{4.24}$$

where $\dot{\sigma}$ is the rate of the Cauchy stress tensor and C_e is the elastic stiffness matrix.

$$\dot{\underline{\sigma}} = \lambda(1-\phi) tr(\underline{d}_e) 1 + 2G(1-\phi)\underline{d}_e - \frac{\dot{\phi}}{1-\phi}\underline{\sigma} \tag{4.25}$$

where λ is the Lamé constant, G is the shear modulus, and $\underline{\sigma}$ is the Cauchy stress. The Cauchy stress is convected with the elastic spin $\underline{W}_e$ where $\overset{o}{\underline{\sigma}}$ is the objective derivative of $\underline{\sigma}$ assuming a Jaumann rate where the continuum spin equals the elastic spin ($\underline{W} = \underline{W}_e$),

$$\overset{o}{\underline{\sigma}} = \dot{\underline{\sigma}} - \underline{W}_e \underline{\sigma} + \underline{\sigma}\underline{W}_e \tag{4.26}$$

4.3 Thermodynamics

The constitutive relations must satisfy the laws of thermodynamics. The thermodynamic equations are written in the current configuration and follow the formulations by Coleman and Gurtin [1967]. The first law can be written in terms of the rate of change in internal energy as

$$\rho\int_B \frac{\partial u}{\partial t} = \int_B \underline{\sigma} : d dv + \int_B \rho r dv - \int_{\partial B} q \cdot \hat{n} da \,, \tag{4.27}$$

with the local form given by

$$\rho \dot{u} = \underline{\sigma} : \underline{d} + \rho r - \nabla \cdot q \,, \tag{4.28}$$

where $\dot{u}$ is the rate of change of internal energy, r is radiation or heat supply generated within the body, and q is conduction. The second law of thermodynamics states that the rate of entropy increase must be greater than or equal to the rate of entropy input to the system. Thus the second law may be written as

$$\rho \dot{s} \geq \rho \frac{r}{\theta} - \nabla \cdot \left(\frac{q}{\theta} \right) \tag{4.29}$$

We assume Helmholtz free energy ψ to be

$$\psi = u - \theta \cdot s \,, \tag{4.30}$$

where u is internal energy, s is a dissipation function for entropy, θ is absolute temperature. The rate form of Eq. (4.30) becomes

$$\dot{u} = \dot{\psi} + \dot{\theta} \cdot s + \theta \cdot \dot{s} \tag{4.31}$$

Combining the rate form of the Helmholz free energy in Eq. (4.31) with the first law in Eq. (4.28) and substituting the results into the second law in Eq. (4.29) results in the Clausius-Duhem inequality

$$-\rho\left(\dot{\psi}+\dot{\theta}s\right)+\underline{\sigma}:\underline{d}-\frac{q}{\theta}grad\,\theta\geq 0\,. \tag{4.32}$$

The free energy ψ may be characterized by observable variables, such as temperature and strain and by hidden or internal state variables, such as damage, isotropic hardening, and kinematic hardening. Because we are interested in the frictional effects during deformation, we consider a strain-like parameter ε_f, related to the hardening at the interface, as an internal state variable for friction. The free energy potential is a function of the observable state variables and the internal state variables. Thus the free energy may be written as

$$\psi=\psi\left(\underline{E}_e,\underline{\beta},\varepsilon_{ss},\varepsilon_f,\phi\right) \tag{4.33}$$

where $\underline{E}_e$ is elastic strain; $\underline{\beta}$ is kinematic hardening, ε_{ss} is isotropic hardening, ε_f is frictional hardening and φ is damage. We also assume that entropy, stress, and temperature are dependent upon these variables per the principle of equipresence- which states that if a variable is present in one constitutive relation it should be present in all the other constitutive equations unless proven otherwise.

Because elasticity is reversible, we are not interested in its history. However, for inelastic behavior, we need to capture the history. To include the history of the deformation, we must include the evolution of the internal variables. Thus, we differentiate the free energy equation which gives

$$\dot{\overline{\psi}}=\frac{\partial\overline{\psi}}{\partial\underline{E}_e}:\underline{d}_e+\frac{\partial\overline{\psi}}{\partial\underline{\beta}}:\dot{\underline{\beta}}+\frac{\partial\overline{\psi}}{\partial\varepsilon_{ss}}\cdot\dot{\varepsilon}_{ss}+\frac{\partial\overline{\psi}}{\partial\varepsilon_f}\cdot\dot{\varepsilon}_f+\frac{\partial\overline{\psi}}{\partial\phi}\cdot\dot{\phi}. \tag{4.34}$$

Thus, for an isothermal behavior the Clausius-Duhem inequality becomes

$$-\rho\left(\frac{\partial\overline{\psi}}{\partial\underline{E}_e}:\underline{d}_e+\frac{\partial\overline{\psi}}{\partial\underline{\beta}}:\dot{\underline{\beta}}+\frac{\partial\overline{\psi}}{\partial\varepsilon_{ss}}\cdot\dot{\varepsilon}_{ss}+\frac{\partial\overline{\psi}}{\partial\varepsilon_f}\cdot\dot{\varepsilon}_f+\frac{\partial\overline{\psi}}{\partial\phi}\cdot\dot{\phi}\right)+\underline{\sigma}:\underline{D}\geq 0 \qquad (4.35)$$

After substituting the relation for the elastic deformation rate Eq. (4.23) and grouping like terms, the Clausius-Duhem inequality becomes

$$\left(\underline{\sigma}-\rho\frac{\partial\overline{\psi}}{\partial\underline{E}_e}\right):\underline{d}_e+\underline{\sigma}:\left(\underline{d}_p^d+\underline{d}_p^f+\underline{d}_p^v\right)$$

$$-\rho\frac{\partial\overline{\psi}}{\partial\underline{\beta}}:\dot{\underline{\beta}}-\rho\frac{\partial\overline{\psi}}{\partial\varepsilon_{ss}}\cdot\dot{\varepsilon}_{ss}-\rho\frac{\partial\overline{\psi}}{\partial\varepsilon_f}\cdot\dot{\varepsilon}_f-\rho\frac{\partial\overline{\psi}}{\partial\phi}\cdot\dot{\phi}\geq 0 \qquad (4.36)$$

Following the work of Coleman and Noll to ensure satisfaction of the entropy inequality, we obtain the following relations for stress

$$\underline{\sigma}=\rho\frac{\partial\overline{\psi}}{\partial\underline{E}_e} \qquad (4.37)$$

and the plastic dissipation becomes

$$\underline{\sigma}:\left(\underline{d}_p^d+\underline{d}_p^f+\underline{d}_p^v\right)-\rho\frac{\partial\overline{\psi}}{\partial\underline{\beta}}:\dot{\underline{\beta}}-\rho\frac{\partial\overline{\psi}}{\partial\varepsilon_{ss}}\cdot\dot{\varepsilon}_{ss}-\rho\frac{\partial\overline{\psi}}{\partial\varepsilon_f}\cdot\dot{\varepsilon}_f-\rho\frac{\partial\overline{\psi}}{\partial\phi}\cdot\dot{\phi}\geq 0 \qquad (4.38)$$

which can physically be interpreted as the inelastic work minus the changes in internal energy due to the internal state variables. The equation can also be expressed in terms of the deviatoric and volumetric parts, such that

$$\underline{\sigma}':\left(\underline{d}_p^d+\underline{d}_p^f\right)-ptr\left(\underline{d}_p^v\right)-\rho\frac{\partial\overline{\psi}}{\partial\underline{\beta}}:\dot{\underline{\beta}}-\rho\frac{\partial\overline{\psi}}{\partial\varepsilon_{ss}}\cdot\dot{\varepsilon}_{ss}-\rho\frac{\partial\overline{\psi}}{\partial\varepsilon_f}\cdot\dot{\varepsilon}_f-\rho\frac{\partial\overline{\psi}}{\partial\phi}\cdot\dot{\phi}\geq 0 \qquad (4.39)$$

where $\underline{\sigma}=\underline{\sigma}'-p\underline{I}$ and the hydrostatic pressure is $p=-1/3Tr(\underline{\sigma})$.

4.4 Kinetics

Kinetics is concerned with the forces acting on a body. While kinematics is not size scale dependent, kinetics is size scale dependent because as volume per surface area

decreases, dislocation interaction dominates resulting in size independent yield. Thus the size scale parameters should be found in the constitutive equations for the internal or "hidden" state variables and not the observable state variable (like strain) since it is length scale invariant. Therefore, to capture the material behavior, kinetics will be used to determine the evolution of the state variables and plastic strain rate which are related to the micromechanics of the material. Dislocations provide the mechanism of plastic deformation for metals. The microstructure which evolves during the deformation is also affected by the strain rate and temperature. In order to formulate our constitutive model, we assume a quadratic form of the Helmholz free energy that is a convex function, is always positive, and is dependent on the elastic strain and state variables which gives

$$\rho\psi = \frac{1}{2}\underline{E}_e : \underline{\underline{C}}_e : \underline{E}_e + \frac{1}{2}C_\beta \underline{\beta}^2 + \frac{1}{2}C_{ss}\varepsilon_{ss}{}^2 + \frac{1}{2}C_f \varepsilon_f{}^2 + \frac{1}{2}C_\phi \phi^2 \tag{4.40}$$

where $\underline{\underline{C}}_e$ is the elastic modulus and C_β, C_{ss}, C_f, and C_φ are material constants. By defining $\underline{\sigma}$, $\underline{\alpha}$, κ, f, and Y as the conjugate stresses (or forces) to the strain-like state variables it follows that the thermodynamic stress conjugates become

$$\underline{\sigma} = \rho\frac{\partial\psi}{\partial\underline{E}_e} = \underline{\underline{C}}_e : \underline{E}_e \ , \tag{4.41}$$

$$\underline{\alpha} = \rho\frac{\partial\psi}{\partial\underline{\beta}} = C_\beta \underline{\beta} \ , \tag{4.42}$$

$$\kappa = \rho\frac{\partial\psi}{\partial\varepsilon_{ss}} = C_{ss}\varepsilon_{ss} \, , \tag{4.43}$$

$$\tau_f = \rho\frac{\partial\psi}{\partial\varepsilon_f} = C_f \varepsilon_f \, , \text{ and} \tag{4.44}$$

$$Y = \frac{\partial\psi}{\partial\phi} = C_\phi \phi \, . \tag{4.45}$$

For the elastic relation in Eq. (4.41), the stress is a function of the deformation and is a form of Hooke's Law. In the above equations the back stress $\underline{\alpha}$ is the thermodynamic force related to kinematic hardening; the isotropic hardening stress κ is the thermodynamic force related to isotropic hardening; the friction stress τ_f is the thermodynamic force related to frictional hardening; and the energy release rate Y is the thermodynamic force related to the damage variable. After substituting terms, the plastic dissipation in Eq. (4.39) may be rewritten in terms of the stress conjugates as

$$\underline{\sigma}' : \left(\underline{d}_p^d + \underline{d}_p^f\right) - ptr\left(\underline{d}_p^v\right) - \underline{\alpha} : \underline{\dot{\beta}} - \kappa \cdot \dot{\varepsilon}_{ss} - \tau_f \cdot \dot{\varepsilon}_f - Y \cdot \dot{\phi} \geq 0 . \tag{4.46}$$

Because the evolution of the state variables and rates of plastic deformation are related to the micromechanics of the material we need expressions for $\dot{\kappa}, \underline{\dot{\alpha}}, \dot{\tau}_f, \dot{\phi}, \underline{d}_p^d$, and $\underline{d}_p^f$ to capture this behavior in the material model. The volumetric rate of plastic deformation was defined by Eq. (4.19) and is a function of $\dot{\phi}$.

4.4.1 Isotropic Hardening

Isotropic hardening parameter is a scalar variable which represents the mechanical strength of a material and controls the amount of hardening resulting from statistically stored dislocations (SSDs). The SSDs accumulate by a statistical trapping process during plastic slip and are associated with deformation of the lattice. The accumulation of dislocations, which is related to crystallographic slip, is the driving force behind isotropic hardening. Therefore, the evolution of the isotropic hardening parameter, which represents the lattice deformation or strains due to statistically stored dislocations can be written in terms of a hardening minus recovery event [Bammann et al., 1993] as

$$\dot{\kappa} = H_{\kappa}(\theta)\left\|\underline{d}_p^d\right\| - \left[R_{do}(\theta)\left\|\underline{d}_p^d\right\| + R_{s\kappa}(\theta)\right]\kappa^2 \tag{4.47}$$

where H_κ represents the isotropic hardening modulus, $R_{d\kappa}$ represents the dynamic recovery constant and $R_{s\kappa}$ represents the static recovery constant.

4.4.2 Kinematic Hardening

Kinematic (or anisotropic) hardening has been linked to back stress in the body and represents the geometrically necessary dislocations (GNDs) created during deformation, such as pile-ups at the grain boundaries. The GNDs preserve lattice compatibility and to accomplish the required lattice rotation. The GND densities also influence plastic slip through a back stress, which counteracts the local resolved shear stress and is related to the heterogeneity of the GND field after removal of the external load. The evolution of the kinematic hardening variable is expressed as [Bammann et al., 1993]

$$\overset{o}{\underline{\alpha}} = \dot{\underline{\alpha}} - \underline{W}_e\underline{\alpha} + \underline{\alpha}\underline{W}_e = H_{\alpha}(\theta)\underline{d}_d^p - \left[R_{d\alpha}(\theta)\left\|\underline{d}_d^p\right\| + R_{s\alpha}(\theta)\right]\|\underline{\alpha}\|\underline{\alpha} \tag{4.48}$$

where H_α is the anisotropic hardening modulus and $R_{d\alpha}$ describes the dynamic recovery and $R_{s\alpha}$ represents the static recovery constant.

4.4.3 Damage

In modeling the compaction of a particulate material, damage is analogous with the void volume fraction and is associated with densification. The total damage can be defined in terms of a coalescence variable multiplied with the void volume fraction [Horstemeyer et al., 2000]

$$\phi = c\left(\phi_{particles} + \phi_{pores}\right), \tag{4.49}$$

where c is the coalescence variable; $\phi_{particles}$ is the volume fraction of voids nucleated from inclusion particles; and ϕ_{pores} is the volume fraction of voids from pre-existing pores. Following the work of Horstemeyer et al. [2000] we assumed that the damage originating from inclusion particles is represented by a nucleation variable η and the void volume v as

$$\phi_{particles} = \eta v \tag{4.50}$$

Therefore, the evolution for the damage is

$$\dot{\phi} = \dot{c}\left(\phi_{particles} + \phi_{pores}\right) + c\left(\dot{\eta} v + \eta \dot{v} + \dot{\phi}_{pores}\right), \tag{4.51}$$

The evolution equation for the void nucleation variable η is given by

$$\dot{\eta} = \left\| \underline{d}_p \right\| \frac{\sqrt{d}}{K_{IC} f^{1/3}} \eta \left\{ a\left[\frac{4}{27} - \frac{J_3^2}{J_2^3} \right] + b \frac{J_3}{J_2^{3/2}} + c \left\| \frac{I_1}{\sqrt{J_2}} \right\| \right\} \exp\left(-Q/\theta \right), \tag{4.52}$$

where Q is a temperature dependent material constant. The material parameters a, b, and c relate to the volume fraction of nucleation events arising from local microstresses in the material and are determined experimentally. The stress state dependence in Eq. (4.52) is captured by using the stress invariants denoted by I_1, J_2, and J_3. I_1 is the first invariant of stress as defined in Eq. (2.8). J_2 is the second invariant of the deviatoric stress defined by Eq. (2.9). J_3 is the third invariant of the deviatoric stress ($J_3 = \frac{1}{3} tr\left(\underline{\sigma}'\right)^3$). Also in Eq. (4.52), f is the volume fraction of the second phase particles, d is a length scale parameter related to the most influential microstructural feature on void nucleation, typically particle size, and K_{IC} is the bulk fracture toughness. The evolution equation for void growth factor v for voids nucleated from second phase particles is given by

$$\dot{v} = \frac{3}{2} v \left[\frac{1}{2} \frac{V(\theta)}{Y(\theta)} \frac{I_1}{\sqrt{3J_2}} + \left(1 - \frac{V(\theta)}{Y(\theta)}\right)(1 + 0.4319) \right]^{Y(\theta)/V(\theta)} \underline{d}_p, \tag{4.53}$$

where $V(\theta)$ determines the magnitude of rate dependence on yielding and $Y(\theta)$ is the rate-independent yield stress. The evolution equation for the coalescence variable is given by

$$\dot{c} = C_{coal} \left[\eta \dot{v} + \dot{\eta} v \right] \exp(C_{CT} \theta) \left(d_0 / d \right)^z \tag{4.54}$$

where d_0 is the initial particle size, and C_{CT} , C_{coal} , and z are model constants. The evolution of the internal state variable for damage is controlled by the void growth rule of cocks and Ashby [1980],

$$\dot{\phi}_{pores} = \left[\frac{1}{(1 - \phi_{pores})^m} - (1 - \phi_{pores}) \right] \sinh \left[\frac{2\left(2^{V(\theta)/Y(\theta)} - 1\right) I_1}{\left(2^{V(\theta)/Y(\theta)} + 1\right) 3\sqrt{3J_2}} \right] \left\| \underline{d}_p \right\|, \tag{4.55}$$

where m is a void growth constant.

4.4.4 Frictional Hardening/Softening

The frictional hardening/softening parameter, τ_f, is a scalar variable which represents the mechanical strength of a material and controls the amount of hardening/softening resulting from dislocation climb in a region near the interface. The lattice deformation or strains due to friction can be written in terms of the dislocation density at the interface as [Bammann, 1990]

$$\varepsilon_f = b\sqrt{\rho_f} \tag{4.56}$$

where b is the magnitude of the Burgers vector. Therefore the rate form of the frictional strain is

$$\dot{\varepsilon}_f = \frac{1}{2}\frac{b}{\sqrt{\rho_f}}\dot{\rho}_f \,. \tag{4.57}$$

Following the work of Kocks [1976] and Mecking [1975], we assume that dislocations are trapped and stored as they move through the body and that the dislocation density storage (or hardening) occurs at a rate inversely proportional to the mean free path of the dislocation and recovers dynamically in proportion to the dislocation density.

$$\frac{d\rho_f}{dE_p} = c_1\frac{1}{\lambda} - c_2\rho_f \;, \tag{4.58}$$

where $E_p = \int_0^t \|d_p\| dt$ is the total plastic deformation.

From the geometry, the stored dislocations are inversely proportional to the mean free path λ and the mean free path is inversely proportional to the square root of the dislocation density.

$$\lambda = \frac{1}{\sqrt{\rho_f}} \tag{4.59}$$

Thus, we have the following formulation for the evolution of stored dislocation density where the incremental dislocation density per plastic strain is a dislocation storage minus recovery event

$$\frac{d\rho_f}{dE_p} = c_1\sqrt{\rho_f} - c_2\rho_f \tag{4.60}$$

where c_1 and c_2 are assumed to be constant. Applying the chain rule we obtain the rate form of the stored dislocation density as

$$\dot{\rho}_f = \frac{d\rho_f}{dt} = \frac{d\rho_f}{dE_p}\frac{dE_p}{dt} = \left(c_1\sqrt{\rho_f} - c_2\rho_f\right)\|\underline{d}_p\| \tag{4.61}$$

Substituting Eq. (4.61) into Eq. (4.57) we obtain the evolution of the frictional strain in terms of the dislocation density,

$$\dot{\varepsilon}_f = \frac{1}{2}\left(c_1 b - c_2 b\sqrt{\rho_f}\right)\left\|\underline{d}_p\right\| \tag{4.62}$$

Following the work of Friedel [1964] who related the shear yield strength to the dislocation density at the initiation of yield, we approximated the relation of the shear yield strength (or friction stress) at the contact interface to the dislocation density at the interface as

$$\tau_f = mGb\sqrt{\rho_f}\,, \tag{4.63}$$

where G is the shear modulus and m is a constant. By substituting Eq. (4.56) into Eq. (4.63) we can express the frictional stress in terms of the frictional strains as

$$\tau_f = mG\varepsilon_f\,, \tag{4.64}$$

which agrees with our definition of the thermodynamic stress conjugate for friction in Eq. (4.44) assuming a quadratic form of the Helmholz free energy,

$$\tau_f = \rho\frac{\partial\psi}{\partial\varepsilon_f} = C_f\varepsilon_f\,. \tag{4.65}$$

By defining the coefficient of friction as the ratio of the frictional stress to the normal contact pressure,

$$\mu = \frac{\tau_f}{\tau_n}\,, \tag{4.66}$$

we can express the friction stress in terms of the coefficient of friction as $\tau_f = \mu\tau_n$. Thus, the frictional strains in terms of the coefficient of friction becomes

$$\varepsilon_f = \frac{\mu\tau_n}{mG}\,. \tag{4.67}$$

By differentiating, we obtain the rate form of the frictional hardening parameter in terms of the coefficient of friction as

$$\dot{\varepsilon}_f = \frac{\tau_n}{mG}\dot{\mu} + \frac{\mu}{mG}\dot{\tau}_n \,. \tag{4.68}$$

From the MD simulations, we obtained the coefficient of friction as a function of the plastic strain in terms of the length scale parameter, V/A_s (in meters),

$$\mu = \mu_o e^{-cE_p} \tag{4.69}$$

where,

$$\mu_o = 0.208 \ln \frac{V}{A_s} + 4.3235 \quad \text{and} \tag{4.70}$$

$$c = 0.6088 \ln \frac{V}{A_s} + 16.473 \,. \tag{4.71}$$

Thus, the internal frictional strain in terms of the plastic strain is

$$\varepsilon_f = \frac{\tau_n \mu_0 e^{-c\|E_p\|}}{mG} \,. \tag{4.72}$$

Differentiating Eq. (4.72), we obtain the rate form of the frictional strain as

$$\dot{\varepsilon}_f = -\frac{c\tau_n \mu_0 e^{-c\|E_p\|}}{mG}\|\underline{d}_p\| + \frac{\mu_0 e^{-c\|E_p\|}}{mG}\frac{\partial \tau_n}{\partial E_p}\|\underline{d}_p\| \,. \tag{4.73}$$

After grouping like terms and substituting Eq. (4.72) into Eq. (4.73), we obtain the following form of the internal frictional strain rate

$$\dot{\varepsilon}_f = \left(\frac{k_n}{\tau_n}\varepsilon_f - c\varepsilon_f\right)\|d_p\| \,, \tag{4.74}$$

where,

$$k_n = \frac{\partial \tau_n}{\partial E_p} \tag{4.75}$$

can be determined from experimental data or from the MD simulation as shown in Figure 4.2 in the current study.

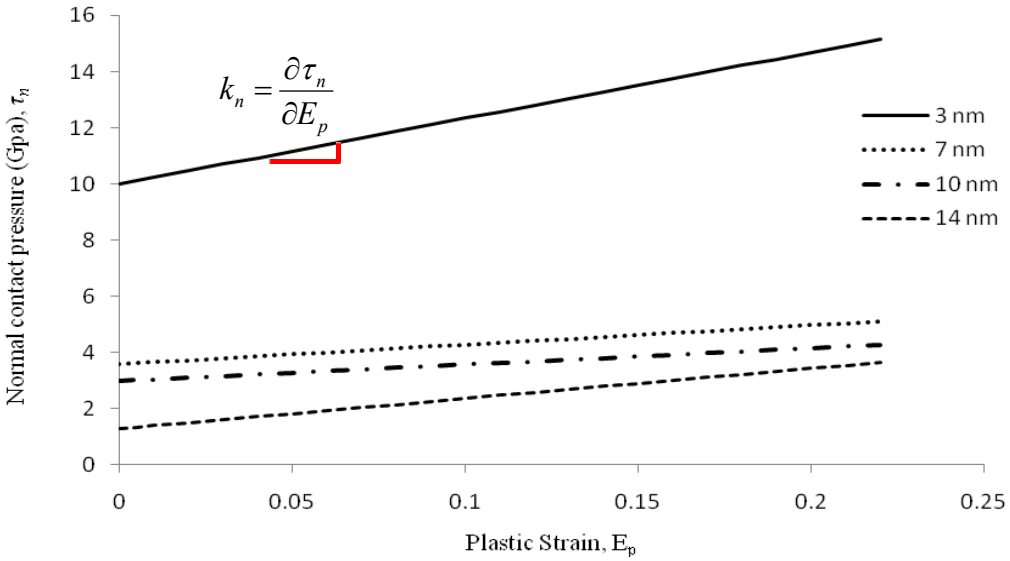

Figure 4.2 MD Simulation results of normal contact pressure versus effective plastic strain.

Eq. (4.74) can be written in terms of hardening minus recovery as

$$\dot{\varepsilon}_f = \left(H_f - R_f\right)\varepsilon_f \left\| \underline{d}_p \right\| \tag{4.76}$$

where,

$$H_f = \frac{k_n}{\tau_n} \text{ and } R_f = c \ . \tag{4.77}$$

Therefore, by combining Eq. (4.65) and (4.76), we obtain the evolution of the frictional hardening parameter, which represents the lattice deformation or strains as

$$\dot{\tau}_f = C_f \left(H_f - R_f\right)\varepsilon_f \left\| \underline{d}_p \right\| \tag{4.78}$$

Using the results of the MD simulation, we obtained the hardening modulus H_f and the dynamic recovery constant R_f. A plot of the frictional hardening/softening parameter from Eq. (4.78) versus plastic strain (assuming m=0.3) for the MD simulation results is given in Figure 4.3. The results show a softening in the 3 nm, 7nm and 10 nm models, with essentially the same response for the 7 and 10 nm models. In comparison, the 14 nm model shows slight hardening, prior to gradual softening due to friction. This can be attributed to the much more significant dislocation structures noted in the MD simulations for the 14 nm model.

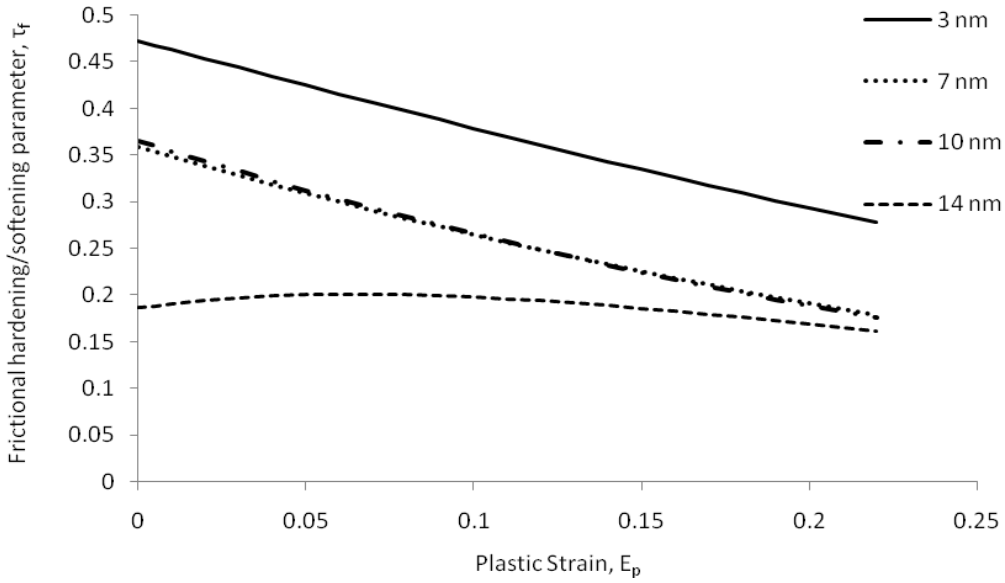

Figure 4.3 Evolution of frictional softening/hardening parameter with length scale dependence.

4.5 Plasticity and Slip

To describe the deformation of ductile materials, an internal state variable plasticity model was used [Bammann et al., 1993]. For the symmetric part of the plastic velocity gradient we represented the dissipations of the irreversible mechanisms, such as

plastic dissipation, damage, frictional sliding, or microstructural variations [Chaboche, 1997], using two independent potentials of dissipation. The first potential Φ_p^d is related to the plastic strain and hardening process (dynamic recovery). The second potential Φ_p^f is related to slip at the interface. The third potential Φ_p^v is related to damage mechanisms. Thus the pseudo potential Φ_p related to the plastic hardening of particles can therefore be decomposed into three parts:

$$\Phi_p = \Phi_p^d + \Phi_p^f + \Phi_p^v \tag{4.79}$$

The plastic potential is associated with the Lagrange multipliers λ_p [Chaboche, 1997]. The plastic deformation rate is represented by its volumetric and deviatoric parts as follows:

$$\underline{D}_p = \dot{\lambda} \frac{\partial \Phi_p}{\partial \underline{\sigma}} = \dot{\lambda}_p \left(-\frac{1}{3} \frac{\partial \Phi_p}{\partial p} \bar{I} + \frac{\partial \Phi_p}{\partial q} \bar{n} \right) \tag{4.80}$$

where λ_p is the plastic or Lagrange multiplier. Similarly, the potentials Φ_p^d and Φ_p^f are respectively associated with the Lagrange multipliers λ_p and λ_f [Chaboche, 1997]. Thus, the associated flow rule becomes

$$\underline{d}_p = \underline{d}_p^f + \underline{d}_p^d + \underline{d}_p^v = \dot{\lambda}_s \frac{\partial \Phi_p^f}{\partial \|\underline{\sigma}'\|} \underline{n} + \dot{\lambda}_p \frac{\partial \Phi_p^d}{\partial \|\underline{\sigma}'\|} \underline{n} - \frac{1}{3} \dot{\lambda}_p \frac{\partial \Phi_p^d}{\partial p} \underline{I} \tag{4.81}$$

Thus we assume that when the interface is in a state of sliding, $\underline{d}_p^f \neq 0$ and frictional sliding dominates the plastic deformation at the interface. On the contrary, when the interface is in a state of sticking, we assume that $\underline{d}_p^d$ dominates the plastic deformation

and $\underline{d}_p^f = 0$. As shown in Figures 4.4a, assuming a von Mises yield criterion, we define the rate dependent yield surface for the plastic straining as

$$f_v^d\left(\underline{\sigma},\underline{\alpha},\kappa,\tau_f,\sigma_y,\sigma_v\right)=\sqrt{\frac{3}{2}}\left\|\underline{\sigma'}-\sqrt{\frac{2}{3}}\underline{\alpha}\right\|-\left(\kappa+\tau_f+\sigma_y(\theta)+\sigma_v\right)(1-\phi) \tag{4.82}$$

where τ_f is the frictional hardening/softening parameter effects the size of the yield surface and σ_v is the viscous stress and captures the rate dependency of the yield surface. For a ductile material in the case of the elasto-viscoplasticity, the plastic multiplier λ_p can be defined as a scalar function of the viscous stress determined by the distance from the stress state to the elastic domain, and is expressed in the form of a hyperbolic sine function,

$$\dot{\lambda}_p = f(\theta)\sinh\left[\frac{f^d}{(1-\phi)V(\theta)}\right], \tag{4.83}$$

where f^d is the rate independent yield function from Eq. (4.82) that excludes the viscous stress ($f^d = f_v^d + \sigma_v$). In associative plasticity, we assume that the plastic dissipation potential is normal to the yield function. Therefore, we define the plastic flow rule (commonly referred to as the rate of plastic deformation) as [Bammann, 1993]

$$\underline{d}_p^d = \sqrt{\frac{3}{2}}f(\theta)\sinh\left[\frac{\sqrt{\frac{3}{2}}\left\|\underline{\sigma'}-\sqrt{\frac{2}{3}}\underline{\alpha}\right\|-\left(\kappa+\tau_f+\sigma_y(\theta)\right)(1-\phi)}{V(\theta)(1-\phi)}\right]\frac{\underline{\sigma'}-\sqrt{\frac{2}{3}}\underline{\alpha}}{\left\|\underline{\sigma'}-\sqrt{\frac{2}{3}}\underline{\alpha'}\right\|} \tag{4.84}$$

The temperature dependent functions *V(θ),* which determines the magnitude of rate dependence on yielding, σ_y which is the rate-independent yield stress, and *f(θ)* which determines when the rate dependence affects initial yielding are defined as

$$V(\theta) = C_1 \exp\left(\frac{-C_2}{\theta}\right) \tag{4.85}$$

$$\sigma_y(\theta) = C_3 \exp\left(\frac{C_4}{\theta}\right) \tag{4.86}$$

$$f(\theta) = C_5 \exp\left(\frac{-C_6}{\theta}\right) \tag{4.87}$$

The constants C_1, C_2, C_3, C_4, C_5 and C_6 are determined by uniaxial isothermal compression tests with different strain rates and temperatures.

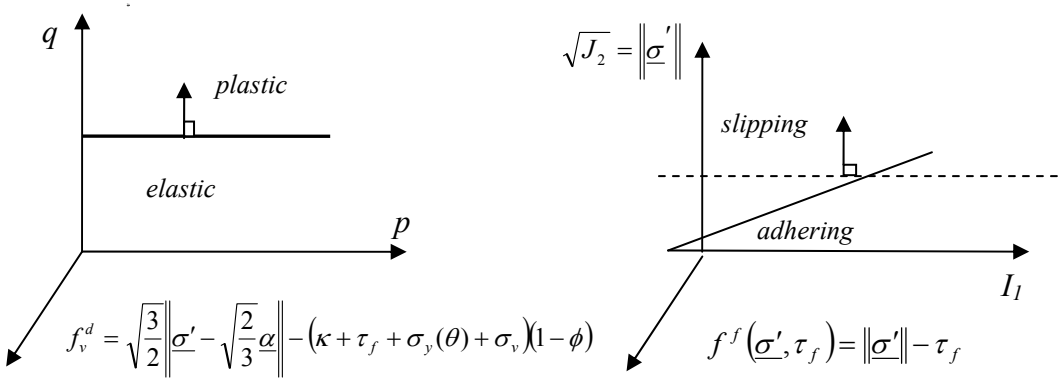

(a) (b)

Figure 4.4 (a) The rate dependent yield surface for plastic deformation due to dislocations and damage, and (b) slip surface for plastic deformations due to friction.

The yield surface for slipping at the interface, shown in Figure 4.4(b), is defined as

$$f^f(\underline{\sigma}', \tau_f) = \|\underline{\sigma}'\| - \tau_f \tag{4.88}$$

When the interface is in a state of slipping, the relative tangential traction equals the frictional stress (or slip resistance), which is defined as a function of the contact pressure and the state of the interface and is the basis of the slip condition given by

$$f^f\left(\underline{\sigma}', \tau_f\right) = \left\| \underline{\sigma}' \right\| - \tau_f \leq 0 \tag{4.89}$$

The rate of deformation at the interface is assumed to be decomposed into elastic (adhering) and plastic (sliding) parts

$$\underline{d}^f = \underline{d}_e^f + \underline{d}_p^f \tag{4.90}$$

When the stress state at the interface is such that $f^f\left(\underline{\sigma}', \tau_f\right) < 0$, the interface is elastic and is adhering and $\underline{D}_p^f = 0$. When the state of stress at the interface is such that $f^f\left(\underline{\sigma}', \tau_f\right) = 0$, $\underline{D}_p^f = 0$. Assuming an isotropic frictional contact, which implies that sliding occurs only in the direction opposite to the tangential reaction, the plastic dissipation potential is defined as

$$\Phi_p^f = \left\| \underline{\sigma}' \right\| + C \tag{4.90}$$

which results in a non-associative flow rule for friction such that

$$\underline{d}_p^f = \dot{\lambda}_f \frac{\partial \Phi_p^f\left(\underline{\sigma}'\right)}{\partial \sigma'} = \dot{\lambda}_f \frac{\underline{\sigma}'}{\left\| \underline{\sigma}' \right\|} \tag{4.91}$$

For rate independent plasticity, we have

$$\dot{f}^f\left(\underline{\sigma}', \tau_f\right) = \dot{\sigma}' : \frac{\partial f^f}{\partial \underline{\sigma}'} + \dot{\tau}_f \frac{\partial f^f}{\partial \tau_f} = 0 \tag{4.92}$$

Therefore, after substituting Eq. (4.78) for $\dot{\tau}_f$ and the following equations for the partial derivatives into Eq. (4.92)

$$\frac{\partial f^f}{\partial \underline{\sigma}'} = \frac{\underline{\sigma}'}{\left\| \underline{\sigma}' \right\|} \quad \text{and} \quad \frac{\partial f^f}{\partial \tau_f} = -1, \tag{4.93}$$

we obtained the following expression,

$$\dot{\sigma}' : \frac{\underline{\sigma}'}{\|\underline{\sigma}'\|} - C_f \left(H_f - R_f\right)\varepsilon_f \left\|\underline{d}_p\right\| = 0 \ . \tag{4.94}$$

Next, we decompose the total plastic rate of deformation into volumetric, frictional, and deviatoric parts which gives us

$$\left(\underline{\underline{C}}_e : \underline{d}_p^d\right) : \frac{\underline{\sigma}'}{\|\underline{\sigma}'\|} - C_f \left(H_f - R_f\right)\varepsilon_f \left\|\underline{d}_p^d\right\| - C_f \left(H_f - R_f\right)\varepsilon_f \left\|\underline{d}_p^f\right\|$$

$$- C_f \left(H_f - R_f\right)\varepsilon_f \left\|\underline{d}_p^v\right\| = 0 \tag{4.95}$$

By combining Eq.(4.91) and Eq.(4.95) and solving for the friction multiplier, we obtain

$$\dot{\lambda}_f = \left[\frac{C_e}{\left(C_f \left(H_f - R_f\right)\varepsilon_f\right)} - 1\right]\left\|\underline{d}_p^d\right\| - \underline{d}_p^v \cdot \frac{\underline{\sigma}'}{\|\underline{\sigma}'\|} \tag{4.96}$$

Therefore, the frictional rate of deformation due to sliding becomes

$$\underline{d}_p^f = \left[\frac{C_e}{\left(C_f \left(H_f - R_f\right)\varepsilon_f\right)} - 1\right]\left\|\underline{d}_p^d\right\| \cdot \frac{\underline{\sigma}'}{\|\underline{\sigma}'\|} - \underline{d}_p^v \tag{4.97}$$

As shown in Figure 4.5, because friction is primarily a surface affect, in the micromechanical FEA model the particles are divided into two regions: a surface region and an interior region. For analysis in the surface region we introduce a switching parameter χ for the slipping condition. When the condition at the interface is slipping, χ=1 and $f^f\left(\underline{\sigma}', \tau_f\right) = 0$. When the condition at the interface is adhering, χ=0 and $f^f\left(\underline{\sigma}', \tau_f\right) < 0$. Therefore, the total plastic rate of deformation in the surface region is represented by the following relations

$$\underline{d}_p^{surface} = \underline{d}_p^d + \chi \underline{d}_p^f + \underline{d}_p^v \tag{4.98}$$

or in expanded form as

$$\underline{d}_p^{surface} = \sqrt{\frac{3}{2}} f(\theta) \sinh\left[\frac{\sqrt{\frac{3}{2}}\left\|\underline{\sigma}' - \sqrt{\frac{2}{3}}\underline{\alpha}\right\| - \left(\kappa + + \tau_f + \sigma_y(\theta)\right)(1-\phi)}{V(\theta)(1-\phi)}\right] \frac{\underline{\sigma}' - \sqrt{\frac{2}{3}}\underline{\alpha}}{\left\|\underline{\sigma}' - \sqrt{\frac{2}{3}}\underline{\alpha}'\right\|} +$$

$$+ \chi\left(\left[\frac{C_e}{\left(C_f\left(H_f - R_f\right)\varepsilon_f\right)} - 1\right]\left\|\underline{d}_p^d\right\| \cdot \frac{\underline{\sigma}'}{\|\underline{\sigma}'\|} - \underline{d}_p^v\right) + \frac{\dot{\phi}}{3(1-\phi)}\underline{I} \tag{4.99}$$

Therefore, when the condition at the interface is slipping (lying outside the slip surface) or χ=1, Eq. (4.99) becomes

$$\underline{d}_p^{surface} = \left[\frac{C_e}{\left(C_f\left(H_f - R_f\right)\varepsilon_f\right)}\right]\left\|\underline{d}_p^d\right\| \cdot \frac{\underline{\sigma}' - \underline{\alpha}}{\|\underline{\sigma}' - \underline{\alpha}\|} \tag{4.100}$$

and the volumetric effects vanish from the expression. However, when the interface is adhering (lying within the slip surface) or χ=0, Eq. (4.99)

$$\underline{d}_p^{\text{int}} = \sqrt{\frac{3}{2}} f(\theta) \sinh\left[\frac{\sqrt{\frac{3}{2}}\left\|\underline{\sigma}' - \sqrt{\frac{2}{3}}\underline{\alpha}\right\| - \left(\kappa + \tau_f + \sigma_y(\theta)\right)(1-\phi)}{V(\theta)(1-\phi)}\right] \frac{\underline{\sigma}' - \sqrt{\frac{2}{3}}\underline{\alpha}}{\left\|\underline{\sigma}' - \sqrt{\frac{2}{3}}\underline{\alpha}'\right\|} + \frac{\dot{\phi}}{3(1-\phi)}\underline{I} \tag{4.101}$$

and the frictional rate of deformations due to slipping vanish.

For plastic deformation behavior within the interior region, the frictional rate of plastic deformation is equal to zero ($\underline{d}_p^f = 0$). The total plastic rate of deformation in the interior region is defined as

$$\underline{d}_p^{\text{int}} = \underline{d}_p^d + \underline{d}_p^v \tag{4.102}$$

or in expanded form as

$$\underline{d}_p^{\text{int}} = \sqrt{\frac{3}{2}} f(\theta) \sinh\left[\frac{\sqrt{\frac{3}{2}}\left\|\underline{\sigma}' - \sqrt{\frac{2}{3}}\underline{\alpha}\right\| - (\kappa + \sigma_y(\theta))(1-\phi)}{V(\theta)(1-\phi)}\right] \frac{\underline{\sigma}' - \sqrt{\frac{2}{3}}\underline{\alpha}}{\left\|\underline{\sigma}' - \sqrt{\frac{2}{3}}\underline{\alpha}'\right\|} + \frac{\dot{\phi}}{3(1-\phi)}\underline{I} \tag{4.103}$$

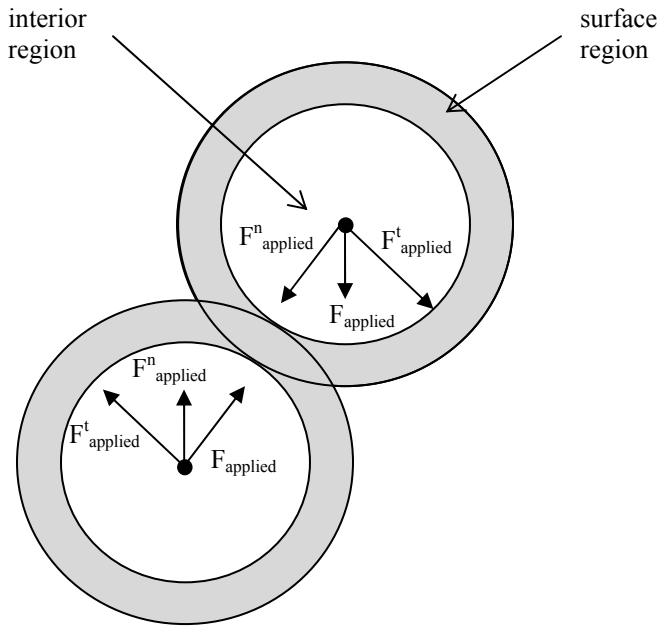

Figure 4.5 Micromechanical finite element model setup with particles defined with a surface region for capturing the frictional effects in the model and an interior region for plastic deformations.

4.6 Modified Drucker-Prager/ Cap Plasticity Model

We considered the modified Drucker-Prager cap plasticity model for the deformation behavior of the granular materials during compaction. Using the cap plasticity model we can include the volume effects during consolidation of the particulate materials, as well as account for frictional effects and elasto-plastic deformation within a macroscopic continuum. This double surface plasticity model consists of an elastic region in stress space, bounded by a shear yield surface, F_s, in the low pressure region which represents internal friction, and a cap yield surface, F_c, in the high pressure region

which represents compression. To avoid numerical instabilities, a smoothing function F_t was introduced [Hammi et al., 2007] to replace the corner intersection between the two surfaces of the cap model. The yield surfaces are plotted in the q-p plane. The modified Drucker-Prager failure and cap surfaces of the smooth cap model for compaction at low densities ($\rho < \rho_c$) are shown in Figure 4.6.

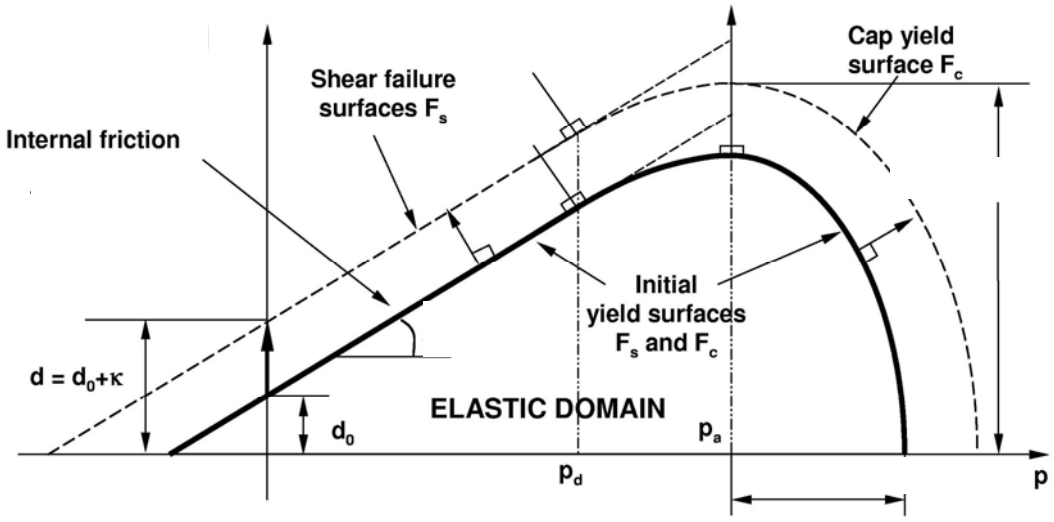

Figure 4.6 Evolution of the failure and cap yield surfaces of the Modified Drucker/Prager Cap Model.

The general equation for the shear yield surface of the model is

$$F_s = q - p\tan\varphi_f - d_0 = 0 \tag{4.104}$$

where d_0 is the material cohesion strength, φ_f is the material internal friction angle, q is the deviatoric stress, and p is the hydrostatic pressure. The shear yield surface is further defined to include the effects of kinematic hardening $\underline{\alpha}$ and isotropic hardening κ and to include the transitional smoothing function F_t such that

$$F_s = \left|\underline{\sigma}' - \underline{\alpha}\right| - \kappa - d_0 - p\tan\varphi_f + F_t(p) = 0 \ , \tag{4.105}$$

where the pressure dependent transition function f_t is defined by:

$$F_t(p) = \frac{H(p - p_d)}{2(p_a - p_d)}[p - p_d]^2 \tan\varphi_f, \tag{4.106}$$

where the cap hardening variable, p_a, is an evolution parameter that represents the volumetric plastic strain driven hardening/softening, p_d is a material parameter, and $H(\cdot)$ is the Heaviside function

$$H(p - p_d) = \begin{cases} 1 & \text{if } p \geq p_d \\ 0 & \text{if } p < p_d \end{cases}. \tag{4.107}$$

The cap yield surface has an elliptical shape and is represented by the following relation

$$F_c = \sqrt{|\underline{\sigma'} - \underline{\alpha}|^2 + \frac{1}{R^2}[p - p_a]^2} - d - (p_a - p_d)\tan\varphi_f = 0 \tag{4.108}$$

where R is a material parameter called the cap eccentricity that controls the shape of the cap. The cap yield surface hardens or softens as a function of the volumetric plastic strain.

When the density reaches a critical value ρ_c, which is the density saturation value obtained from compressibility curves, the cap surface is replaced by a von Mises yield surface (Figure 4.7). Therefore, the yield surface for $p > p_a$ becomes pressure independent and is given by

$$F_p = |\underline{\sigma'} - \underline{\alpha}| - F_s(p_a) = 0 \tag{4.109}$$

The shear failure envelope remains identical at high pressure to describe shear crack during compaction and ejection, which is critical due to the granular nature of green compacts.

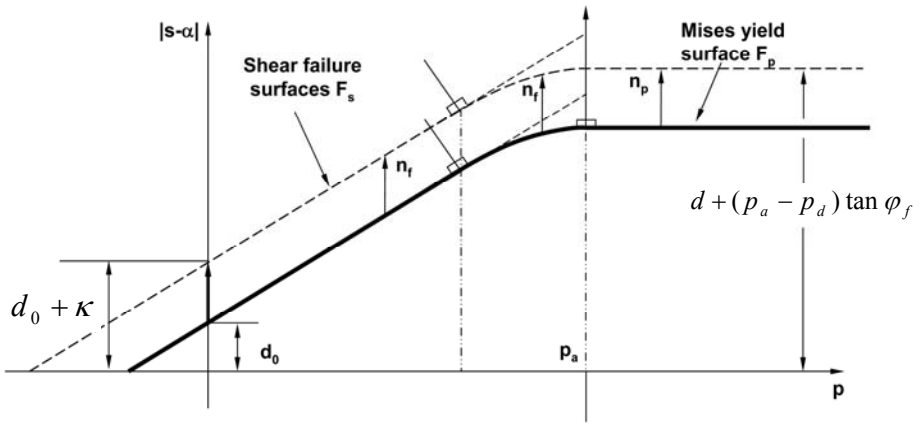

Figure 4.7 Representation of the double yield surface for dense powder aggregate.

As shown in Figure 4.8, in the current PM research studies the interparticle friction is determined based on experiments and is calculated as a function of density,

$$\tan\varphi_f = \begin{cases} c_1 - c_2\rho_d & \text{if } \rho \le \rho_d \\ c_1 - c_2\rho & \text{if } \rho > \rho_d \end{cases} \tag{4.110}$$

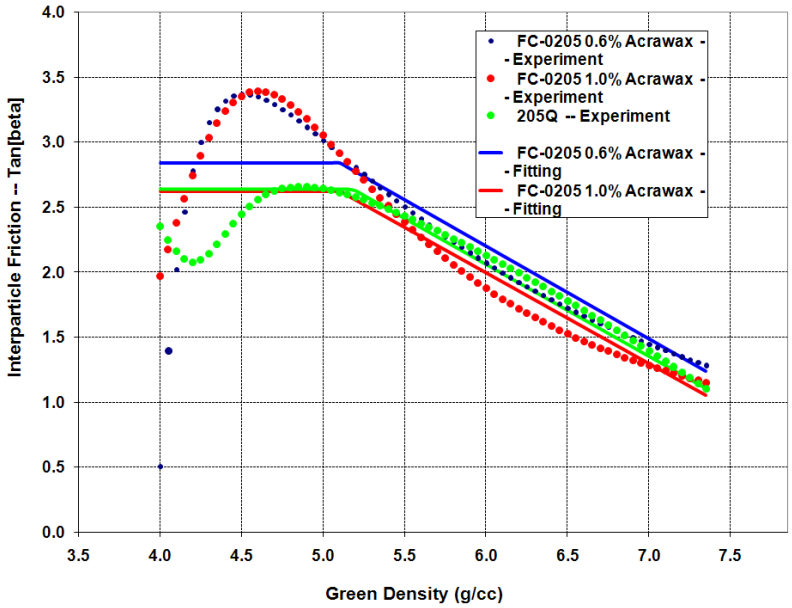

Figure 4.8 Experimental results for interparticle friction angle versus green density for FC-0205 and 205Q steel materials.

By determining the interparticle friction based on evolution equations of the internal state variables, we can obtain a more accurate prediction of the plastic behavior of metal powders during compaction. For the aggregate, the interparticle friction defines the slope of the failure envelope and can be related to the coefficient of friction as

$$\mu = \tan\varphi_f . \tag{4.111}$$

The rate form of the friction angle can be written as

$$\dot{\varphi}_f = \frac{1}{1+\mu^2}\dot{\mu} \tag{4.112}$$

By substituting Eq. (3.29), the evolution equation for the coefficient of friction derived from the MD simulations, we obtain the evolution for the friction angle of the aggregate in terms of the plastic rate of deformation as

$$\dot{\varphi}_f = \frac{-c\mu}{1+\mu^2}\left\|\underline{D}_p\right\| \tag{4.113}$$

where $\mu = \mu_0 e^{-c\varepsilon_p}$. Material parameters μ_0 and c are defined by Eq. (4.70) and Eq. (4.71), respectively, and capture the length scale effect of friction and can be determined from MD simulations or experiments.

4.7 Summary of Chapter 4

A multiscale friction framework based upon internal state variable theory has been developed. The kinematics was modified by including a frictional component in the multiplicative decomposition of the deformation gradient in order to account for the frictional surface effects due to sliding. The evolution of the frictional hardening variable was formulated as a hardening minus recovery event in terms of frictional strains within the material. The parameters for the frictional strains were obtained from MD nanoscale

studies. For the micromechanical formulation, the particles were divided into two regions: a surface region and an interior region for including deformations due to sliding at the interface, in addition to frictional/softening effects within the particles due to friction. For the macroscale continuum model, the friction is accounted for in an evolution equation for the friction angle of the powder aggregate. The constitutive model was coupled with the Bammann-Chiesa-Johnson (BCJ) rate-independent plasticity model to capture the deformation behavior due to dislocations at the interface.

CHAPTER V

CONCLUSIONS AND FUTURE WORK

5.1 Conclusions

Using contact laws and an adhesion law for friction, we developed a friction model that captures the atomic scale effects at the interface of the contacting surfaces from the MD simulations. The resulting interface friction model formulation combined the influence of particle size using the volume-per-surface-area parameter and was validated with experimental results and the model prediction was extended to micron-sized particles. We developed a multiscale friction model based on internal state variable theory by incorporating the microstructural features, along with the volume per surface area length scale parameter from the nanoscale MD simulations. The kinematics was modified by including a frictional component in the multiplicative decomposition of the deformation gradient in order to account for the frictional surface effects due to sliding, as well as frictional hardening/softening within the particles. The evolution of the frictional hardening variable was formulated as a hardening minus recovery event in terms of frictional strains within the material. The constitutive model was coupled with the Bammann-Chiesa-Johnson (BCJ) rate-dependent plasticity model to capture the deformation behavior of the particles.

5.2 Future Work

5.2.1 Friction Model Implementation

Currently, an implicit time-integration procedure for the proposed friction model is being formulated. Upon completion, the friction model will be implemented into the existing ISV BCJ user material model for ABAQUS. For the powder aggregate, the frictional evolution equation should be implemented into the existing Drucker-Prager Cap Plasticity user material model for ABAQUS.

5.2.2 Friction Model Correlation and Validation with Nickel

After the material model is implemented, experiments need to be performed to obtain the model frictional hardening and recovery parameters. The multiscale friction model should be tested in a two-particle finite element model to correlate the model parameters obtained from the MD simulations. The model should then be applied to a multi-particle finite element model, followed by an actual continuum model (ie. powder metallurgy part) to test the range of the model prediction..

5.2.3 Extend MD Simulation Study to Include Other Materials

In the current study, nickel was the only material evaluated using the MD Simulations. Future work should involve performing the MD simulations for other metals, like copper, and comparing the results with those obtained for nickel.

5.2.4 Energy Dissipation

We want to understand the way in which sliding kinetic energy is dissipated at the surface. Therefore, future MD studies at different temperatures to observe thermal

effects on dislocation structures should be considered. We want to quantify the energy dissipation arising from sliding friction versus the energy dissipation from plastic deformation (ie. dislocations) at the contact to obtain a better understanding of the underlying mechanisms of friction.

REFERENCES

Adams, G. G., S., Müftü, S., and N. Mohd Azhar, 2003. A Scale-Dependent Model for Multi-Asperity Contact and Friction. ASME J. Tribol. 125, 700–708

Amontons, G., 'De la Resistance Causee dans les Machines. Mem. De l'Academie Royale A, 1699, pp. 275–282.

Anand, L. "A constitutive model for interface friction," Computational Mechanics, 12 (4), 1993, pp. 197-213.

Anand, L. and C. Gu, "Granular materials: constitutive equations and strain localization," Journal of the Mechanics and Physics of Solids, 48, 2000, pp. 1701-1733.

Bammann, D.J., "Modeling temperature and strain rate dependent large deformations of metals," In: E. Kremple, D.L. McDowell (Eds.), Part 2. Appl. Mech Rev., 43 (5), 1990, S312-S319.

Bammann, D.J., M.L. Chiesa, M.F. Horstemeyer, and L.I. Weingarten, "Failure in ductile materials using finite element methods," In: Jones, N., Wierzbicki, T. (Eds.), Structural Crashworthiness & Failure, Elsevier, Amsterdam, 1993, pp. 1–54.

Bhushan B. and M. Nosonovsky, "Scale effects in friction using strain gradient plasticity anddislocation-assisted sliding (microslip)," Acta Materialia, 51, 2003, pp. 4331-4345.

Bowden FP, D. Tabor. The Friction and Lubrication of Solids. Oxford: Clarendon Press; 1950.

Carpick, R. W., N. Agrait, D. F. Ogletree, and M. Salmeron, "Measurement of interfacial shear (friction) with an ultrahigh vacuum atomic force microsope," Journal of Vacuum Science Technology B, 14, 1996, pp. 1289-1295.

Chaboche, J-L., "Thermodynamic formulation of constitutive equations and application to the viscoplasticity and viscoelasticity of metals and polymers," International Journal of Solids and Structures, 34 (18), 1997, pp. 2239-2254.

Cheng, J.H. and N. Kikuchi, "An incremental constitutive relation of unilateral contact friction for large deformation analysis," Journal of Applied Mechanics, 52, 1985, pp. 639-648.

Cocks, A.C.F and M.F. Ashby, "Intergranular fracture during power-law creep under multiaxial stresses," Met. Sci., 14, 1980, pp. 395-402.

Coleman, B.D. and M.E. Gurtin, "Thermodynamics with internal state variables," Journal of Chemical Physics, 47 (2), 1967, pp. 597- 613.

Coube, O. and Riedel, H., "Numerical Simulation of Metal Powder Die Compaction with Special Consideration of Cracking," Powder Metallurgy, 43 (2), 2000, pp. 123–131.

Coulomb C.A. de., Théorie des machines simples, en ayant égard au frottement de leurs parties et à la roideur des cordages~ Theory of Simple Machines, Mém Math Phys Acad R Sci 1781:161. Reprinted Paris:Bachelier;1821.

Daw, M.S. and M.I. Baskes, "Embedded-atom method: Derivation and application to impurities, surfaces, and other defects in metals," Physical Review B, 29 (12), 1984, pp. 6443-6453.

Daw, M.S., S.M. Foiles, and M.I. Baskes, "The embedded-atom method: A review of theory and applications," Materials Science Reports, A Review Journal, 9 (7-8), 1993, pp. 251-310.

Derjaguin B.V., V.M. Muller, and Y.P. Toporov, "Effect of contact deformations on the adhesion of particles," Journal of Colloid Interface Science, 53, 1975, pp. 314-326.

Deshpande, V.S., A. Needleman, and E. Van der Giessen, "Discrete dislocation plasticity analysis of static friction," Acta Materialia, 52, 2004, pp. 3135–3149.

DiMaggio, F.L. and I.S. Sandler, "Material models for granular soils," Journal of Engineering Mechanics, ASCE, 97, 1971, pp. 935–950.

Dominik, C. and A.G.G.M. Tielens, "Resistance to sliding on atomic scales in the adhesive contact of two elastic spheres," Philos. Mag. A, 73, 1996, pp. 1279-1302.

Drucker, D.C. and W. Prager, "Soil mechanics and plastic analysis of limit design," Quart. Applied Mathematics, 10 (2), 1952, pp. 157-165.

Drucker, D.C., R.E. Gibson, and D.J. Henkel, "Soil mechanics and work hardening, theories of plasticity," Transactions ASCE, 122, 1957, pp. 338-346.

Fang, H., M.F. Horstemeyer, M.I. Baskes, and K. Solanki, "Atomistic Simulations of Bauschinger Effects of Metals with High Angle and Low Angle Grain Boundaries," Computer Methods in Applied Mechanics and Engineering, 193 (17-20), 2004, pp. 1789-1802.

Fleck, N.A., "On the cold compaction of powders," J. Mech. Phys. Solids, 43, no. 9, 1995, pp. 1409-1431.

Fleck, N.A., L.T. Kuhn, and R.M. McMeeking, "Yielding of metal powder bonded by isolated contacts," Journal of the Mechanics and Physics of Solids, 50 (5), 1992, pp. 1139-1162.

Fleck, N.A., G.M. Muller, M.F. Ashby, and J.W. Hutchinson, "Strain gradient plasticity-theory and experiment," Acta Materialia, 42, 1994, pp. 475-487.

Foiles, S.M., M.I. Baskes, and M.S. Daw, "Embedded-atom-method functions for the fcc metals Cu, Ag, Au, Ni, Pd, Pt, and their alloys," Physical Review B, 33 (12), 1986, pp. 7983-7991.

Fredriksson, B., "Finite element solution of surface nonlinearities in structural mechanics with special emphasis to contact and fracture mechanics problems," Comp. & struct., 6, 1976, pp. 281-290.

Frenkel D. and Smit B. Understanding Molecular Simulation: From Algorithms to Applications. 2nd ed. San Diego: Academic Press; 2002.

Friedel, J., Dislocations. Oxford, New York: Pergamon Press; 1964

Gao, J, W.D. Luedtke, D. Gourdon, M. Ruths, J.N. Israelachvili, and U. Landman, "Frictional forces and Amontons' Law: From the molecular to the macroscopic scale," Journal of Physical Chemistry B, 108 (11), 2004, pp. 3410-3425.

Gerberich,W.W., N.I. Tymak, J.C. Grunlan, M.F. Horstemeyer, and M.I. Baskes, 'Interpretations of Indentation Size Effects,' J. Applied Mechanics, 69 (4), 2002, pp. 443-442.

Gu, C., M. Kim, and L. Anand, "Constitutive equations for metal powders: application to powder forming processes," International Journal of Plasticity, 17, 2001, pp. 147-209.

Gullett P.M., G. Wagner, A. Slepoy. Numerical tools for atomistic simulations. SAND2003- 8782; January 2004.

Hammi, Y., L. Tucker, P.G. Allison, T.W. Stone, M.F. Horstemeyer, E. Marin, "Constitutive modeling of compaction and sintering for P/M automotive Components," Advances in Powder Metallurgy and Particulate Materials, Princeton, NJ: MPIF; 2007.

Hanlon T., A.H. Chokshi, M. Manoharan, and S. Suresh, "Effects of grain refinement and strength on friction and damage evolution under repeated sliding contact in nanostructured metals," International Journal of Fatigue, 27, 2005, pp. 1159-1163.

Hattamleh, O.A., B. Muhnuthan, and H.M. Zbib, "Multi-slip gradient formulation for modeling microstructure effects on shear bands in granular materials," International Journal of Solids and Structures, 44, 2007, pp. 3393-3410.

Hertz, H., ''Ueber die Beruehrung fester elastische Koerper ~On the contact of elastic solids,'' J. fuer reine und angewandte Mathematik, 92, 1882, pp. 156–171.

Homola, A.W., J.N. Israelachvili, P.M. McGuiggan, and M.L. Gee, "Fundamental experimental studies in tribology: the transition from "interfacial" friction of undamaged molecularly smooth surfaces to normal friction with wear," Wear, 136, 1990, pp. 65-83.

Hoover, W.G., "Canonical dynamics: Equilibrium phase-space distributions," Physical Review A, 31 (3), 1985, pp. 1695-1697.

Horstemeyer, M.F., M.I. Baskes, and S.J. Plimpton, "Size scale and time scale Effects on the plastic flow of fcc metals," Acta Materialia, 49 (20), 2001a, pp. 4363-4374.

Horstemeyer M.F., M.I. Baskes, and S.J. Plimpton, "Computational nanoscale plasticity simulations using embedded atom potentials," Theoretical and Applied Fracture Mechanics, 37, 2001b, pg 49-98.

Horstemeyer, M.F., M.I. Baskes, V.C. Prantil, J. Philliber, and S. Vonderheide, "A multiscale analysis of fixed-end simple shear using molecular dynamics, crystal plasticity, and a macroscopic internal state variable theory," Modelling and Simulation in Materials Science and Engineering, 11, 2003, pp. 265-286.

Horstemeyer, M. F., J. Lathrop, A.M. Gokhale, and M. Dighe, "Modeling Stress State Dependent Damage Evolution in a Cast Al-Si-Mg Aluminum Alloy," Theoretical and Applied Fracture Mechanics, 33, 2000, pp. 31-47.

Horstemeyer, M.F., T.J. Lim, W.Y. Lu, D.A. Mosher, M.I. Baskes, V.C. Prantil, and S.J. Plimpton, "Torsion/simple shear of single crystal copper," Journal of Engineering Materials and Technology, 124, 2002, pp. 322-328.

Horstemeyer, M.F. and D.L. McDowell, "Modeling effects of dislocation substructure in polycrystal elasto-viscoplasticity," Mech. Mater., 27, 1998, pp. 145–163.

Hurtado, J.A. and K-S Kim, "Scale effects in friction of single-asperity contacts. I. From concurrent slip to single-dislocation-assisted slip," Proc. R. Soc. Lond. A, 455, 1999a, pp. 3363-3384.

Hurtado, J.A., and Kim, K.-S., 1999, Scale Effects in Friction in Single Asperity Contacts: Part II; Multiple-Dislocation-Cooperated Slip. Proc. R. Soc. London,Ser. A, A455, 1999b, pp. 3385–3400.

Johnson K.L., Contact Mechanics. 1st ed. Cambridge: Cambridge University Press;1987.

Johnson K.L., "Adhesion and friction between a smooth elastic spherical asperity and a plane surface," Proc R Soc London A, 453, 1997, pp. 163-179.

Johnson K.L., K. Kendall, A.D. Roberts, "Surface energy and the contact of elastic solids," Proc R Soc London A, 324, 1971, pp. 301-313.

Kelchner, C.L., S.J. Plimpton, and J.C. Hamilton, "Dislocation nucleation and defect structure during surface indentation," Physical Review B, 58 (17), 1998, pp. 11085-11088.

Kim D. E.and N.P. Suh, "Molecular dynamics investigation of two-dimensional atomic-scale friction," Journal of Tribology, 116, 1994, pp. 225-231.

Ko, J.S. and A.J. Gellman, "Friction anisotropy at Ni(100/Ni(100) Interfaces," Langmuir, 16, 2000, pp. 8343-8351.

Kocks, U.F., "Laws for work-hardening and low-temperature creep," J. Eng. Mater. Technol., 98, 1976, pp. 76-85.

Koh, S.J.A. and H.P. Lee, "Molecular dynamics simulation of size and strain rate dependent mechanical response of FCC metallic nanowires," Nanotechnology, 17, 2006, pp. 3451-3467.

Kröner, E., "Allgemeine kontinuumstheorie der versetzungen und eigenspannungen," Archive for Rational Mechanics and Analysis, 4, 1960, pp. 273–334.

Landman U., W.D. Luedtke, and E.M. Ringer in "Fundamentals of friction: macroscopic and microscopic processes," (eds J. L. Singer and H. M. Pollock), 1992, Kluwer, Dordrecht, pp. 463-508.

Larsson, J. and B. Storåkers, "Oblique indentation of creeping solids," European Journal of Mechanics, A/Solids, 19, 2000, pp. 565-584.

Lee, E.H., “Elastic plastic deformation at finite strain,” ASME Journal of Applied Mechanics 36, 1969, pp. 1–6.

McElthaney, K.W., J.J. Vlassak, and W.D. Nix, “Determination of indentor tip geometry and indentation contact area of depth-sensing indentation experiments,” J. Mater. Res., 13 (5), 1998, pp. 130-136.

McLellan, A., “Theorem Generalized”, American Journal of Physics, 42(3), 1974, pp. 239-243.

Mecking, H., In: A. W. Thompson (ed), Work Hardening in Tension and Fatigue, TMS-AIME, New York, 1975, pp. 67-88.

Michalowski R. and Z. Mroz, “Associated and non-associated sliding rules in contact friction problems,” Arch. Mech., 30, 1978, pp. 259-276.

Michalske, T.A and J. E. Houston, “Dislocation nucleation at nano-scale mechanical contacts,” Acta Materialia, 46 (2), 1998, pp. 391-396.

Mishra R., B. Basu, R. Balasubramaniam, “Effect of grain size on the tribological behavior of nanocrystalline nickel,” Materials Science and Engineering A, 373, 2004, pp. 370-373.

Nosé, S., “A unified formulation of the constant temperature molecular dynamics method,” Journal of Physics and Chemistry, 81, 1984, pp. 511-519.

Plimpton, S.J., “Fast parallel algorithms for short-range molecular dynamics,” J. Comput. Phys., 117 (1), 1995, pp. 1-19.

Potirniche, G.P., J.L. Hearndon, M.F. Horstemeyer, and X.W. Ling, "Lattice Orientation Effects on Void Growth and Coalescence in fcc Single Crystals," International Journal of Plasticity, 22, 2006a, pp. 921-942.

Potirniche, G. P., and M.F. Horstemeyer, "On the Growth of Nanoscale Fatigue Cracks," Philosophical Magazine Letters, 86 (3), 2006b, pp. 185-193.

Potirniche, G.P., M.F. Horstemeyer, B. Jelinek, and G. J. Wagner, "Fatigue Damage in Nickel and Copper Single Crystals at Nanoscale," International Journal of Fatigue, 27 (10-12), 2005a, pp. 1179-1185.

Potirniche, G. P., M. F. Horstemeyer, G. J. Wagner, and P. M. Gullett, "A Molecular Dynamics Study of Void Growth and Coalescence in Single Crystal Nickel," International Journal of Plasticity, 22 (2), 2005b, pp. 257-278.

Procopio, A.T. and A. Zavaliangos, “Simulation of multi-axial compaction of granular media from loose to high relative densities,” Journal of the Mechanics and Physics of Solids, 53, 2005, pp. 1532-1551.

Qi, Y. and Y-T Cheng, “Friction anisotropy at Ni(100)/(100) interfaces: Molecular dynamics studies,” Physical Review B, 6, 2002, pp. 085420-1 - 085420-7.

Raous, M., L. Cangémi, and M. Cocu, “A consistent model coupling adhesion, friction, and unilateral contact,” Computer Methods in Applied Mechanics and Engineering, 177 (3-4), 1999, pp. 383-399.

Riedel, H., D. Meyer, J. Svoboda, and H. Zipse, “Numerical simulation of die pressing and sintering: development of constitutive equations,” International Journal of Refractory Metals and Hard Materials, 12 (2), 1993-1994, pp. 55-60.

Seguchi, Y., A. Shindo, Y. Tomita, and M. Sunohara, “Sliding Rule of Friction in Plastic Forming of Metals,” Computational Methods in Nonlinear Mechanics, University of Texas Austin, 1974, pp. 683-692.

Solanki, K, M.F. Horstemeyer, M.I. Baskes, and H. Fang, “Multiscale study of dynamic void collapse in single crystals,” Mechanics of Materials, 37, 2005, pp. 317-330.

Stone, T., M . Horstemeyer , Y . Hammi , P . Gullett, “Contact and friction of single crystal nickel nanoparticles using molecular dynamics**,”** Acta Materialia, 56 (14), 2008, pp. 3577 – 3584.

Storåkers, B., S. Biwa, and P.L. Larsson, “Similarity analysis of inelastic contact,” International Journal of Solids Structure, 34, 1997, pp. 3061-3083.

Storakers, B., N.A. Fleck, and R.M. McMeeking, “The viscoplastic compaction of composite powders,” Journal of the Mechanics and Physics of Solids, 47, 1999, pp. 785-815.

Suh, N. P. and H.C. Sin, "The Genesis of Friction," Wear, 69, 1981, pp, 91-114.

Surender M., B. Basu, and R. Balasubramaniam, “Wear characterization of electrodeposited Ni-WC composite coatings,” Tribology Internaltion, 37, 2004, pp.743-749.

Tambe, N.S. and B. Bhushan, “Friction model for the velocity dependence of nanoscale friction,” Nanotechnology, 16, 2005, pp. 2309- 2324.

Tomlinson, G.A., “A molecular theory of friction,” Philosophical Magazine, 7, 1929, pp. 905-939.

Zhang, L. and H. Tanaka, "Towards a deeper understanding of wear and friction on the atomic scale-- molecular dynamics analysis," Wear, 211, 1997, pp. 44-53.

Zhang, L.C., K.L. Johnson, and W.C.D. Cheong, "A molecular dynamics study of scale effects on the friction of single-asperity contacts," Tribolology Letters, 10, 2001, pp. 23-28.

APPENDIX A

SUMMARY OF MODEL CONFIGURATIONS

SUMMARY OF MODEL CONFIGURATION

Particle Size (nm)	Contact Angle (degrees)	Strain rate (/s)	Total Strain (%)	Temp (K)
3.52	60	5.00E8	20	300
3.52	30	4.37E8	18	300
3.52	0	4.17E8	17	300
7.04	60	2.50E8	20	300
7.04	30	2.19E8	18	300
7.04	0	2.08E8	17	300
10.0	60	1.76E8	20	300
10.0	30	1.54E8	18	300
10.0	0	1.47E8	17	300
14.0	60	1.25E8	20	300
14.0	30	1.09E8	17	300

APPENDIX B

MD SIMULATION SAMPLE INPUT FILE

```
# DESCRIPTION:  Compaction of 2 Ni sphere (w/ 2 half spheres) 7.04 nm diameter
# using ramp velocity, strain rate 2.185E8, temp 300K, 30 deg contact angle
#-----------------------------------------------------------------------#

units   real
potential  eam 1 nialhjea
timestep   0.005
lattice    fcc 3.52
neighbor   0.3 1

# free in all directions
periodicity  0 0 0

# outputs
thermo     10
#restart      1000 restart_tensile

# box
create box -11 21 -20 37.32 -11 11

# create 100 lattice
orient  x 1 0 0
orient  y 0 1 0
orient  z 0 0 1
origin  0.0 0.0 0.0

select region -11 21 -20 37.32 -11 11
define cutout 0 sphere  0.0 0.0 0.0 10.0
create atoms 1

# create 100 lattice
orient  x 1 0 0
orient  y 0 1 0
orient  z 0 0 1
origin  10.0 17.32 0.0

select region -11 21 -20 37.32 -11 11
define cutout 0 sphere  10.0 17.32 0.0 10.0
create atoms 2

# create 100 lattice
orient  x 1 0 0
orient  y 0 1 0
orient  z 0 0 1
origin  10.0 37.32 0.0

select region -11 21 -20 37.32 -11 11
define cutout 0 sphere  10.0 37.32 0.0 10.0
create atoms 3

# create 100 lattice
orient  x 1 0 0
orient  y 0 1 0
orient  z 0 0 1
origin  0 -20.0 0.0

select region -11 21 -20 37.32 -11 11
define cutout 0 sphere  0 -20.0 0.0 10.0
create atoms 4
```

```
# create types for lower (5) and upper (6) fixed planes
select region inf inf -20 -19 inf inf
create types 5
select region inf inf 36 37.32 inf inf
create types 6

# initialize thermal velocities on interior atoms
select type  1
create vels  thermal 600.0 1
select type  2
create vels  thermal 600.0 1
select type  3
create vels  thermal 600.0 1
select type  4
create vels  thermal 600.0 1

# initially, all lower and upper surfaces are fixed
select type  5
create fixes xyz 0 0 0
select type  6
create fixes xyz 0 0 0

# apply temperature controls on active atoms
temp type  1
temp control hoover 300.0 10.0
temp type  2
temp control hoover 300.0 10.0
temp type  3
temp control hoover 300.0 10.0
temp type  4
temp control hoover 300.0 10.0


# run to equilibrate temperature (10 ps)
# set up output
snapshot   100 Ni7_30b_parts_eq
snap column  7
snap thresh  centro 2.0
diagnostic tensile_meam 50 Ni7_30b_eq.dat 4 2 5 14.70 010
run     2000
reset timestep  0

# minimize potential energy
#relax 100
#reset timestep 0

# initial Vy of fixed atoms-add ramped velocity to get strain rate of 2.185E8/s
check vels      0
select type  5
create vels  ramp vy 0.00625 0.00625 y -20 -19
select type  6
create vels  ramp vy -0.00625 -0.00625 y 36 37.32

#add Vy ramp to active atoms
select type 4
create vels  ramp vy 0.00625 0.004 y -19 -10
select type 1
create vels  ramp vy 0.004 0 y -10 8.66
select type 2
create vels  ramp vy 0 -0.004 y 8.66 27.32
```

```
select type3
create vels   ramp vy -0.004 -0.00625 y 27.32 36

# make sure ramped velocity is taken into account in temperature
temp adjust   ramp vy 0.00625 -0.00625 y -20 37.32

# set up output
snapshot   100 Ni7_30b_parts
#1- multiple parts, 0- only one part
snap types 1
snap column   7
snap thresh   centro 2.0

#Compute stresses on center particles (avg) & on each part
diagnostic tensile_meam 50 Ni7_30b.dat 4 2 5 14.70 010
# create force and velocity data file
#write meamstat 1000 meamstat7nm60b

# run up to approx. 18.0% strain
run     180000
```